GROWTH AND ELECTRONIC PROPERTIES OF NANOSTRUCTURED EPITAXIAL GRAPHENE ON SILICON CARBIDE

A Thesis
Presented to
The Academic Faculty

by

David Britt Torrance

In Partial Fulfillment
of the Requirements for the Degree
Doctor of Philosophy in the
School of Physics

Georgia Institute of Technology
December 2013

Copyright © 2014 by David Britt Torrance

GROWTH AND ELECTRONIC PROPERTIES OF NANOSTRUCTURED EPITAXIAL GRAPHENE ON SILICON CARBIDE

Approved by:

Professor Phillip N. First, Advisor
School of Physics
Georgia Institute of Technology

Professor Walt de Heer
School of Physics
Georgia Institute of Technology

Professor Andrew Zangwill
School of Physics
Georgia Institute of Technology

Professor Zhigang Jiang
School of Physics
Georgia Institute of Technology

Professor Thomas Orlando
School of Chemistry & Biochemistry
Georgia Institute of Technology

Date Approved: May 29 2013

To my wife, Lisa Leilani Matragrano. Without your love and support I would never have made it this far.

PREFACE

Many observers have expressed the oft-repeated phrase that 'graphene is the new silicon,' implying that graphene will one day supplant silicon in modern electronics. Despite the obvious technological hurdles which must first be overcome before this prediction can come true, I personally find a better parallel between graphene and the invention of polymer materials. As detailed in her article titled 'A brief history of plastic's conquest of the world,' Susan Freinkel explains how plastic was initially adopted to manufacture combs and billiard balls, which were traditionally luxury items made from expensive and rare materials such as animal ivory [1]. Plastic substitutes for these simple products were met by an incredible demand from the broad majority of consumers, who suddenly could afford to purchase these much cheaper analogues. This increased demand, in turn, resulted to investments by government and industry into researching new kinds of synthetic plastics, rubbers, and eventually polymers. Researchers went on to develop entirely new products using artificial polymer materials that would have been impossible to create using natural materials. Although any of these products are considered common-place today, the introduction of materials such as Velcro™, Teflon™, Kevlar™, and carbon fiber composites have had revolutionary applications in fields spanning from cookware to the aerospace industry.

I personally foresee a similar technology road map for graphene technologies over the next 20 years or more. First, graphene will be used as a simple replacement or additive in currently existing technologies. To some extent this phase has already begun as multiple start-up companies have developed techniques manufacturing large quantities of dispersed graphene flakes [2], which are being used as a replacement

for graphite in carbon fiber composites, conductive ink for printable electronics, and lithium-ion battery electrodes [3]. The second phase will involve new and revolutionary products which make better use of graphene's amazing mechanical, chemical, electronic, and optical properties. In the end, I believe that graphene, like plastics, will fall victim to its own success and fade into everyday obscurity.

ERRATA

The Acknowledgements page has been replaced with the following errata.

ERRATA ENTRY 1

a. Page vi, starting with line 1.

b. Original Passage

I would like thank my thesis committee: Dr. Thomas Orlando and Dr. Zhigang Jiang (for taking the time and effort), Dr. Andrew Zangwill (for teaching me Electromagnetism), Dr. Walt de Heer (for the wonderful collaborations), and of course my advisor Dr. Phillip First. Without Phil I would not be the person I am today; his tutelage has made me a better scientist and a more interesting person.

To the graduate students in the First laboratory, I am forever in your debt. To Joanna Hass and Nikhil Sharma for teaching me how to operate the initially arcane UHV equipment and perform STM. To David Lee Miller and Kevin Kubista for countless conversations, insights, and an extra pair of hands with a wrench. To Greg Rutter for being my friend and colleague. Also to the current students in the First lab: Tien Hoang, Yuntao Li, Caven Yang, and Chen Di. And of course the undergraduates that worked on various projects that I was involved with: Madeleine Phillips, Evan Greene, and, of course, Owen Andrews, without whom I would never have been able to complete Chapter 4.

To my friends at Georgia Tech who provided a shoulder to lean on, someone to talk to over coffee or beer, and in several cases the delight of working together, in no particular order: Alex Weiner, Chris Malec, Farhana Zaman, John Hankinson, Grahame Vittorini, Jeremy Hicks, Yike Hu, Ming Ruan, Daniel Borrero.

To my parents, Ralph D. and Deborah H. Torrance, for teaching me to love hard and excel academically. It seems that chemistry set really paid off. To my brother, Michael Cole Torrance, for being my brother. To my friends Ted McDonald, Greg Weaver, and Charles Stephen ``Quatro" Shaughnessy: you know what you did.

You were there.

c. New Passage

I would like to thank my thesis committee: Dr. Thomas Orlando and Dr. Zhigang Jiang (for taking the time and effort), Dr. Andrew Zangwill (for teaching me Electromagnetism), Dr. Walt de Heer (for the wonderful collaborations), and of course my advisor Dr. Phillip First. Without Phil I would not be the person I am today; his tutelage has made me a better scientist and a more interesting person.

To the graduate students in the First laboratory, I am forever in your debt. To Joanna Hass and Nikhil Sharma for teaching me how to operate the arcane lab equipment. To David Lee Miller and Kevin Kubista for countless conversations and insights. To Greg Rutter for being my friend and supporter. Also to the current graduate students in the First lab: Tien Hoang, Yuntao Li, Caven Yang, and Chen Di. To the undergraduates: Madeleine Phillips, Evan Greene, and, of course, Owen Andrews, without whom I would never have been able to complete Chapter 4.

To my friends at Georgia Tech who provided a shoulder to lean on, someone to talk to over coffee or beer, and in several cases the delight of working together, in no particular order: Alex Weiner, Chris Maleċ, Farhana Zaman, John Hankinson, Grahame Vittorini, Jeremy Hicks, Yike Hu, Ming Ruan, Daniel Borrero. Thank you.

To my parents, Ralph D. and Deborah H. Torrance, for teaching me to love hard and excel academically. It seems that chemistry set really paid off. To my brother, Michael Cole Torrance, and my friends Ted McDonald, Greg Weaver, and Charles Stephen Shaughnessy. Thank you all.

Portions of this work were supported by the National Science Foundation (grants DMR-0804908, DMR-0820382 [MRSEC], and DMR-1106131), and by the Semiconductor Research Corporation through the NRI-INDEX program.

TABLE OF CONTENTS

DEDICATION . . . . **iii**

PREFACE . . . . **iv**

ACKNOWLEDGEMENTS . . . . **vi**

LIST OF FIGURES . . . . **ix**

SUMMARY . . . . **xvii**

I INTRODUCTION **1**

1.1 Motivation 1

1.2 Electronic Structure of Graphene 4

1.2.1 Chirality and Backscattering Suppression 10

1.2.2 Half-integer Quantum Hall Effect 13

II METHODS **15**

2.1 Sample Preparation 15

2.1.1 Mechanical and Chemical Mechanical Polishing 18

2.1.2 Hydrogen Etching 22

2.1.3 Dimple Grinding 25

2.2 Epitaxial Graphene Growth 31

2.3 Sample Characterization 36

2.3.1 Particle Scattering Techniques 37

2.3.2 Scanning Tunneling Microscopy 44

III EPITAXIAL GRAPHENE GROWTH ON SILICON CARBIDE **57**

3.1 Motivation for Kinetic Theory of Graphene Growth 57

3.2 Auger Attenuation Model 62

3.3 Kinetic Theory of Graphene Growth on Silicon Carbide 72

3.4 Results 78

3.4.1 High Pressure Argon Growth 78

3.4.2 Growth in Silane Gas 86

3.5 Conclusion 89

IV SIDEWALL GRAPHENE NANORIBBONS STUDIED BY SCANNING TUNNELING MICROSCOPY 92

4.1 Types of Sidewall Graphene Nanoribbons 98

4.2 Methods 100

4.3 Results 101

4.3.1 SiC Sidewall Nanofacet Structure 101

4.3.2 Atomic-scale structure of sidewall graphene nanoribbons . . . 105

4.3.3 Electronic States in sidewall graphene nanoribbons 112

4.3.4 Buffer Layer 120

4.4 Conclusion 121

V CONCLUSION 124

5.1 Summary of Results 124

5.2 Future Studies 127

REFERENCES 129

VITA 177

LIST OF FIGURES

1.1 Schematic demonstrating how graphene is the fundamental building block of graphite (stacking), carbon nanotubes (rolling), and spherical fullerenes like C_{60} (wrapping). 5

1.2 The graphene crystal lattice, with the A and B sublattices denoted by colored atoms. The graphene unit-cell (2.46 Å) contains one atom from each sublattice. 7

1.3 Graphene band structure calculated using the near-neighbor tight-binding approximate [4]. 9

1.4 Chirality and pseudospin conservation in graphene. The black arrows refer to momentum, and the green arrows pseudospin. The chirality of a quasiparticle in graphene is determined by the band index λ and the valley index ξ, where the chirality eigenvalue $\eta = \xi\lambda$ 12

2.1 AFM topography measurements of the as-received hexagonal SiC samples purchased from Cree Research, Inc. (a) Simple mechanical polishing with a diamond based slurry leaves the SiC with residual, randomly oriented scratches that are up to several nanometers deep. 21

2.2 (a) Picture of the custom tantalum thin-wall hydrogen etching furnace, which can prepare both (b) single unit-cell and (c) half unit-cell 6H SiC(0001) surfaces (measured by AFM) depending upon the etching recipe and initial surface conditions. 24

2.3 Commercial First Nano Graphene Furnace (Easy Tube 3000), capable of heating up to 100 mm diameter substrates up to 2200 ° C in various environments. The inset is an AFM image of a 4H SiC(0001) substrate hydrogen etched in this furnace, displaying smooth and straight 8.43 ± 2.68 nm high step bunches (scale bar is 20 um) 25

2.4 (a) Gatan 656 Dimple Grinder used to micromachine vicinal SiC. (b) The dimple grinder operates by rotating a grinding/polishing spherically-shaped wheel coated in an abrasive against the sample, while simultaneously rotating the sample. The wheel has a spherical profile so that the concave, spherical dimple is formed on the substrate. In this figure the wheel is not aligned with the sample axis of rotation which would result in an aspherical surface dimple. 26

2.5 AFM image of a dimpled surface immediately after slow polishing with 0.25 um diamond compounds for 30 minutes. 28

2.6 A(a) Bright-field optical microscopy image and (b) AFM scan of a SiC dimple rapidly polished with 0.25 μm diamond compound for 30 minutes. The field of view of the optical microscopy image is approximately 0.5 mm, and the image was white-balanced and contrast enhanced for better visibility. 28

2.7 AFM images of a dimpled/vicinal 4H SiC(0001) surface after hydrogen etching in the custom furnace. (a) Near the center of the dimple the terrace widths are large because the surface is nominally on-axis, whereas (b) near the edge of the dimple the miscut angle is 4° and terrace width are much smaller. 29

2.8 Bright-field optical microscopy (10x) of hydrogen etching induced step bunches on dimpled SiC. Photo was enhanced to improve contrast, but the step bunches are clearly visible in the unprocessed version. 30

2.9 Images of step bunches formed on a dimpled/vicinal step after hydrogen etching in the FNG furnace. (a) SEM image of the complete step bunches near the lower left corner of the dimple (shown in inset). (b) AFM image of the step bunches near the center of the dimple. Scale bar is 20 μm 30

2.10 Room Temperature UHV system, equipped with an electron electron beam heater, Low-Energy Electron Diffraction, Auger Electron Spectroscopy, and Scanning Tunneling Microscopy. 32

2.11 UHV chamber used for in-situ sample growth in a custom graphite furnace, and in-situ sample analysis using a retarding field analyzer for Auger electron spectroscopy (AES) and low-energy electron diffraction (LEED). SiC samples are held in a graphite holder that allows access to both sides of the wafer (inset; red balls represent gaseous silicon). The sample holder effectively seals the graphite furnace, leaving only a narrow annular channel (6.35 mm mean diameter, 15 μm width) between the sample holder and furnace wall. 34

2.12 Diagram of the Retarding Field Analyzer used for both AES and LEED in the UHV-F system. The dashed lines denote the grids used for filtering electron scattered from the sample surface, where G2 and G3 are connected to variable voltage and G1 and G4 are held at ground for electrostatic shielding. The (green) solid half-circle behind the grids is the glass collector plate, which is coated with both a transparent electrode and a phosphorescent powder for diffraction imaging. The voltage on the collector ranges from as low as 200 V for AES, and as high as 5 kV for LEED (although it is typically operated between $3-4$ kV. The Ammeter connected to the collector for measuring Auger electron current is a simplification; in practice, the current is measured using a lock-in amplifier. 40

2.13 Depiction of LEED pattern acquisition using an RFA. The centered electron gun emits the low-energy primary beam, which diffract off the surface of the sample. The scattered electrons are energy-filtered by the stack of grids (depicted as a transparent gray region). A diffraction pattern forms on the phosphorescent collector because of constructive interference between electrons diffracted from a sample, in this case the $(6\sqrt{3} \times 6\sqrt{3})$R30° surface reconstruction on SiC(0001). 41

2.14 Auger electrons are scattered from materials when they are exposed to high energy electron or x-ray beams (1), which can eject electrons from core-shell orbitals in the near-surface region of the sample. The electron cloud relaxes by filling the core-shell vacancy with an electron from a higher energy level, releasing energy which can excite and eject an Auger electron (3). 43

2.15 Schematic describing the operation of a typical STM. In this setup the sample is stationary while the tip is connected to a single tube piezo, which can be scanned in the X,Y, and Z direction depending upon the voltages output from the STM electronics. A voltage bias V_{bias} is applied between the STM tip and the sample and the tunneling current I_t is monitored by the STM electronics. A feedback loop in the STM electronics maintains a constant I_t by adjusting the tip-sample separation using the the high voltage output of the STM electronics connected to the piezoelectric scanner. The inset shows the atomically sharp STM tip positioned several Angstroms from the sample surface during operation. The arrows demonstrate that electrons can tunnel between the STM tip and sample in either direction depending upon the voltage bias. 52

2.16 RT STM supported from two sets of spring stages (visible in the background) in an UHV system. The white Macor block in the center of image supports two concentric tube piezoelectric elements for actuating the STM tip across the sample surface. Thin gold wires leading to the STM tip or the tube piezoelectric electrodes can be see on the back of Macor. A dimpled SiC sample is visible on the platter-shaped sample holder in front of the STM tip. 55

3.1 This figure describes the two different geometries used for EG growth on SiC. (a) The open geometry has the sample surface freely exposed to a large volume, such that the surface is accessible to material deposition and experimental characterization, but allows for the silicon to sublimate freely from the SiC surface during annealing. (b) In the confined geometry the silicon is heated in a small, enclosed furnace so that silicon vapor has many collisions with the sample before escaping. 58

3.2 Comparison of the different models (lines) and measurements (points) of free electron decay lengths in graphite as a function of electron energy in eV. The electron EAL was calculated using the NIST Electron Effective-Attenuation-Length Database (SRD 82). 67

3.3 Comparison of the different models (lines) and measurements (points) of free electron decay lengths in SiC as a function of electron energy in eV. The electron EAL was calculated using the NIST Electron Effective-Attenuation-Length Database (SRD 82). 68

3.4 Theoretical model of the attenuation of the Si LMM Auger electron signal relative to the C KLL Auger signal for graphene on both SiC(0001) (red/solid line) and SiC(000$\bar{1}$ (blue/dashed line). An abrupt interface between SiC and graphene was assumed based upon the most recent models of these systems [5, 6]. The inset shows the same plot on a logarithmic scale which demonstrates that the Si Auger intensity decays with the same exponential slope for both SiC surfaces. The offset between the two curves is due to the different relative orientation of the Si-C bilayer for each SiC surface termination. 71

3.5 LEED pattern from EG grown on SiC(0001) in the UHV-F furnace. This sample was grown until 1 ML of graphene surface coverage corresponding to predominantly buffer layer graphene on SiC(0001), as confirmed by the prominence of the graphene, SiC, and $(6\sqrt{3} \times 6\sqrt{3})$R30° diffraction peaks. 79

3.6 LEED patterns from EG grown on SiC(000$\bar{1}$) in the UHV-F furnace. (a) LF003 was heated at 1450 °C for 20 minutes in 827 mbar of argon gas, which resulting in 0.4 ML of graphene. Graphene diffraction spots are epitaxial with the SiC by 30 degree rotation, and there is very little azimuthal broadening. (b) LF011 was graphitized at 1625 °C for 20 minutes in 827 mbar of argon gas. The average graphene thickness on LF011 was 3.2 ML, as confirmed the lack of visible SiC spots. All graphene spots were broadened azimuthally but there was no 'ring' of diffraction intensity characteristic of rotational disorder. 80

3.7 Graphene growth rates versus (a) temperature and (b) pressure for both of the SiC terminations studied. Carbon face CMP samples are indicated with an open symbol, all other samples were hydrogen etched prior to growth. 82

3.8 Graphene growth rates for carbon face (triangles) and silicon face (circles) SiC, normalized according to the sublimation-diffusion relationship derived in Equation 3.23b. The fits to equation 3.23b for each silicon carbide termination is displayed to show the high level of agreement with the proposed model. For the carbon face (solid line), $\log \Psi_F = 31.32 \pm 2.50 \log(\frac{ML}{sec}\,\text{mbar}\, K^{-\frac{1}{2}})$, and $\Delta H = 5.33 \pm 0.36$eV. For the silicon face (dashed line), $\log \Psi_F = 34.33 \pm 3.77 \log(\frac{ML}{sec}\,\text{mbar}\, K^{-\frac{1}{2}})$, and $\Delta H = 5.81 \pm 0.54$ eV. Carbon face CMP samples are indicated with an open symbol. Data points in the grey region are samples which were grown to more than a single monolayer of carbon as determined by AES and/or ellipsometry. 83

3.9 AFM of two samples grown simultaneously at 1625 $^\circ$C for 20 minutes in 827 mbar of argon gas. The height profiles were acquired along the dashed lines in each image. (a) The carbon face of Sample LF011 has an average surface coverage of 3.2 ML of graphene, with an RMS surface roughness of 0.35 nm. The surface has roughened following graphitization, such that the original unit-cell step structure is no longer visible in this image. (b) In contrast, the silicon face of sample LF010 has an average surface coverage of 1.15 ML, and the steps have bunched into 4.06 ± 0.94 nm steps. The terraces between each step bunch have an RMS surface roughness of 0.14 nm. 85

3.10 AFM and LEED of sample LF014, which was grown in 827 mbar of 0.7% silane/argon mixture. (a) AFM and of the carbon face of sample LF014, which was grown in 827 mbar of 0.7% silane/argon mixture for 20 minutes. The silicon carbide is step bunched (average step height is 2.15 ± 1.01 nm), with $1-3$ nm high pleats in the graphene running across the otherwise smooth terraces with an RMS surface roughness of 0.10 nm. (b) LEED of sample LF014 shows a typical diffraction pattern expected for high-quality multilayer epitaxial graphene grown on SiC(000$\bar{1}$). Compared to samples grown in similar Argon environments (ie. Fig. 3.6), the graphene on LF014 is much thicker (No evidence of SiC diffraction peaks) and contains much more rotational disorder. . . 88

4.1 Graphene nanoribbons are formed by cutting a graphene sheet into narrow strips. In general there exist three different classes of ideal nanoribbons (a-c) as defined by the orientation of the ribbon with respect to the graphene crystal lattice. (a) Zig-zag nanoribbons have have edge-terminated atoms belonging to a single carbon sublattice, while (b) armchair ribbons have atoms from both sublattices at the edge. Another possibility is to have a periodic arrangement of zig-zag and armchair edge sites, called (c) chiral nanoribbons. 94

4.2 Images of the low-vacuum CCS furnaces used to grow sidewall GNRs on SiC(0001) in this study. 99

4.3 AFM and EFM measurements of sample 25Ed30 (on-axis GNR) after graphitization. (a) AFM shows that step bunching has occurred across the surface, which an average step height of 4 nm in this region. (b) a 3D representation of the sample in (a) with the EFM data as on overlay. The surface potential on the SiC sidewall nanofacets changes by approximately 2 V relative to the SiC terraces, indicating the presence of sidewall GNRs. 100

4.4 LEED on samples (a) 25Ed30 (on-axis GNR) and (b) HDS009 (dimpled GNR), after outgassing as described in the text. Both LEED patterns are consistent with a buffer layer covered SiC(0001) surface, although the dimpled GNR sample is much more ordered than the on-axis sample. 102

4.5 Large-scale STM images of GNR covered sidewalls nanofacets on (a) on-axis (25Ed30) and (b) dimpled SiC (HDS009). 103

4.6 Detailed STM images of sidewall nanofacets on on-axis SiC (25Ed30) 104

4.7 Detailed STM images of sidewall nanofacets on dimpled SiC (HDS009) 105

4.8 (a) STM image ($V_B = 1.0$ V, $I_t = 50$ pA) of the top portion of a multiple nanofacet step bunch on the on-axis sample. (b) The entire step bunch is $\sim$ 10 nm high, but only the top 3 nm as shown in the profile. (c) Carefully subtracting the background height variation from the SiC substrate reveals the atomic lattice of sidewall GNR on both the terrace and the nanofacet. The atomic lattice was made prominent and added back to the background to demonstrate that the graphene lattice is continuous onto the SiC nanofacet (local height enhancement). This image is local height enhanced to display both the atomic lattice and SiC sidewall. Near the sidewall the graphene lattice bulges upward $\sim$ 1 Å and the graphene lattice is distorted relative to the imaging on the terrace, as shown in (d) the FFT power spectrum of the atomic lattice, where white/black is low/high power. 106

4.9 Higher resolution STM image (V_B = 0.7 V, I_t = 50 pA) of the top portion of the sidewall GNR shown in Figure 4.8. The profile across the middle of image shows that the graphene gradually bulges upward 3 Å over $\sim$ 3 nm before proceeding onto the SiC sidewall nanofacet. The asymmetric sublattice imaging is strongest in the middle of the bulge, where the graphene lattice is most distorted. 107

4.10 (a) Atomic sale resolution STM image (V_B = -0.6 V, I_t = 30 pA) of the GNR on the dimpled SiC sample (HDS009), on the same SiC sidewall shown in Figure 4.7b. The graphene lattice is continuous across the basal plane and SiC nanofacet, and what may be a $(\sqrt{3}\times\sqrt{3})$R30° electronic scattering pattern is present in the transitionary region where the graphene abruptly curves over the edge. The atomic scale information was local height enhanced to simultaneously display the graphene lattice and the large-scale features of the SiC sidewall. (b) Profile of the local height enhanced image along the dashed line in (a). 109

4.11 (a) Background subtracted image of Figure 4.10, and (b) 2D Fast-Fourier Transform (FFT) of the background subtracted image. The peaks attributed to graphene lattice are highlighted by the outer circles. The graphene lattice constant is uniformly compressively strained by $\sim$ 12 %. 109

4.12 (a) (V_B = -1.5 V, I_t = 30 pA) STM image (V_B = 1 V, I_t = 100 pA) of the graphene (layer-1) on top of the graphene buffer layer (layer-0) on SiC(0001) . At this voltage bias the LDOS of the buffer layer is much greater than the LDOS of the graphene overlayer, so the buffer layer dominates the tunneling current and the constant height image. The buffer layer lattice is constant is uniformly compressively strained by $\sim$ 12 % as determined by FFT (not shown). The sample in (b) was grown in UHV by thermal annealing with an electron beam heater (section 2.2) 110

4.13 3D rendering of the on-axis, sidewall GNR in Figure 4.8c. The colored marks represent the approximate locations were STS was performed as the sample drifted laterally with respect to the tip scanning window. 114

4.14 (a) STS (red line) on the on-axis, sidewall GNR in Figure 4.13 at the red (right hand side) marker. A possible energy gap (limited by the noise level of the current) of $\sim$ 400 meV is centered about the Fermi energy ($V_B = 0$ V). Several distinct peaks are present at higher energies at both positive and negative sample bias. The black line at negative sample bias is the electron states (positive sample bias) mirrored about the E_D to demonstrate electron-hole symmetry. The peak energy spacing is $E_N \propto \sqrt{N}$ where N is the index of the peak. (b) Pseudo-Landau level fan plot for the peaks identified in (a). . . . 115

4.15 (a) STS (purple line) on the on-axis, sidewall GNR in Figure 4.13 at the purple (middle) marker. The energy gap of $\sim$ 400 meV about the Fermi energy ($V_B = 0$ V) is more distinct in this region. This STS scan swept a larger range of sample biases compared to figure 4.14, revealing even more electron-hole symmetric peaks (identified by tick marks) at higher energy. (b) Pseudo-Landau level fan plot for the peaks identified in (a) 116

4.16 STS (blue line) on the on-axis, sidewall GNR in Figure 4.13 at the blue (left hand side) marker. There is no clear energy gap in this region but a large collection of peaks are visible which display electron-hole symmetry. However, unlike the previous spectra, only some the peaks seem to follow a $E_N \propto \sqrt{N}$ energy dependence. 117

4.17 STS of a sidewall GNR on the dimpled SiC sample. (a) Color coded regions of interest wherein spectra were averaged together and plotted in (b) and (c). The image shows the line-by-line subtracted topography of the GNR as it transitions from the basal plane to the nanofacet of the SiC. The scale bar is equal to 2 nm. 119

SUMMARY

The two-dimensional phase of carbon known as graphene is actively being pursued as a primary material in future electronic devices. The goals of this thesis are to investigate the growth and electronic properties of epitaxial graphene on SiC, with a particular focus on nanostructured graphene. The first part of this thesis examines the kinetics of graphene growth on SiC(0001) and SiC($000\bar{1}$) by high-temperature sublimation of the substrate using a custom-built, ultra-high vacuum induction furnace. A first-principles kinetic theory of silicon sublimation and mass-transfer is developed to describe the functional dependence of the graphene growth rate on the furnace temperature and pressure. This theory can be used to calibrate other graphene growth furnaces which employ confinement controlled sublimation. The final chapter in this thesis involves a careful study of self-organized epitaxial graphene nanoribbons (GNRs) on SiC(0001). Scanning tunneling microscopy of the sidewall GNRs confirms that these self-organized nanostructures are susceptible to overgrowth onto nearby SiC terraces. Atomic-scale imaging of the overgrown sidewall GNRs detected local strained regions in the nanoribbon crystal lattice with strain coefficients as high as 15%. Scanning tunneling spectroscopy (STS) of these strained regions demonstrate that the graphene electronic local density of states is strongly affected by distortions in the crystal lattice. Room temperature STS in regions with a large strain gradient found local energy gaps as high as 400 meV. Controllable, strain-induced quantum states in epitaxial graphene on SiC could be utilized in new electronic devices.

CHAPTER I

INTRODUCTION

1.1 Motivation

Scientific and commercial interest in graphene, a two-dimensional crystal of carbon atoms in a honeycomb lattice, has grown explosively over the last 8 years. Since 2004, the global scientific community has become increasingly more focused on studying the properties and applications of graphene. The number of academic publications per year concerning graphene has grown from 161 in 2004 to 8594 in 2012.[1] This eruption of scientific work was ignited by the discovery of multiple methods for isolating graphene, either by mechanical exfoliation from graphite [7] or by controlled growth on a substrate [8]. Graphene has evolved from a topic of only theoretical interest (and originally as a model for better understanding graphite and carbon nanotubes), into a veritable playground for exploring exotic experimental physics and a potential candidate for various future technologies. As of yet there is not an actual product which truly capitalizes on the unique properties of graphene, and some of the more exciting applications may be several decades away yet [9]. But despite this near-term shortcoming, funding for graphene research from both government agencies and private corporations has been extremely generous in the last 8 years. Research centers focusing primarily on graphene have been founded in the United States, Europe, and Asia. In 2013 the European Union (EU) approved a $1.3 billion Graphene Flagship funding initiative to be dispersed over 10 years. Nokia is a partner institute in the EU graphene flagship, and rival Samsung has already invested substantially in graphene R&D [10–12]. South Korea has proposed a 6 year, $200 million graphene research

[1] According to Thomas Reuters Web of Science Citation Report tool, as of March 19, 2013.

initiative [13]. As of 2012, South Korean university and Samsung researchers have secured over 260 graphene-related patents regarding optics and electronics applications [14]. IBM is reportedly considering a hybrid carbon approach, wherein carbon nanotubes replace traditional Si field-effect transistors (FET) [15] and graphene is used for radio-frequency (RF) transistors [16, 17]. Intel has taken a much more conservative track and has only acknowledged the possibility of specialty graphene components in their future products [18]. The question, then, is thus: why has graphene attracted so much intellectual and financial capital when there are alternative technologies that are both more mature and better understood?

While some exotic materials may be superior to graphene in terms of singular metrics, what makes graphene unique is the fact that it is not a single-purpose material with niche applications. Graphene is simultaneously the world's strongest and flimsiest material, it has a thermal conductivity one order of magnitude higher than copper, it is relatively chemically inert, and it has been shown to possess electronic mobilities up to two orders of magnitude higher than that found in Si. Most of the interest in graphene has stemmed from this materials unique and exciting electronic properties, which include room temperature ballistic charge transport, electrostatic carrier doping control, and exotic degrees of freedom that are not present in traditional electronic materials such as silicon. For these reasons, graphene has been positioned as a component material in future integrated circuits and possibly as a replacement for silicon electronics altogether.

However, a lack of wafer-scale high quality graphene and limitations related to industry-standard processes have slowed the acceptance of graphene by the major semiconductor electronics manufacturers. Graphene exfoliates from bulk graphite in irregularly shaped, micrometer sized flakes that are completely unsuitable for industrial electronics. Various groups have demonstrated the ability to grow very large-area sheets of graphene on metallic substrates such as Cu using chemical-vapor

deposition (CVD). However, in most cases CVD graphene has very small domains which degrades the material's electronic characteristics. Even as the quality of CVD graphene improves, the technique is fundamentally limited by the destructive process of transferring the graphene onto an insulating substrate. In addition, a major hurdle for wide-scale adoption of graphene in the semiconductor industry is that intrinsic graphene is not a semiconductor. Without a band gap it is impossible to achieve reasonable switching using a CMOS-compatible graphene FET. It is also unclear if proposed graphene band structure engineering techniques will be successful in creating a band gap while simultaneously preserving the high mobility inherent to graphene.

The work in this thesis will address the two major technological obstacles discussed above. Chapter 3 concerns the critical problem of growing high-quality graphene on a non-conductive substrate. I will show that epitaxial graphene growth on SiC by substrate sublimation [19] is an ideal platform for graphene electronics, and that the growth process itself can be understood using a simple kinetic gas theory to model the growth rate. Band structure engineering of epitaxial graphene SiC(0001) was studied in Chapter 4. In particular, graphene nanoribbons were grown on the low-angle facet or sidewalls of SiC(0001) to study the effects of quantum confinement on the electronic properties of this material. The graphene nanoribbons were studied using a variety of techniques, but the bulk of the work presented will involve scanning tunneling microscopy (STM). STM was used to characterize the morphology of the nanoribbons across the SiC substrate and to probe the electronic density of states of the material. It was found that the system, although complicated, can only be understood if one takes into account the combined effects of confinement, local doping, and (most importantly) strain. Chapter 2 discusses the experimental techniques used in this thesis in detail, and the conclusions of the thesis project are presented in Chapter 5.

1.2 Electronic Structure of Graphene

The electronic properties of graphene were first studied by Wallace in 1947, as an intermediate step towards calculating the band structure of graphite [20]. This approach was refined by multiple authors in the following decades to explain the magnetic and optical properties of graphite [21–23]. Theoretical interest in graphene was reignited by the discovery of carbon nanotubes in 1991 [24]. The electronic states in carbon nanotubes were investigated by multiple theory groups in this time period [25–32]. Ando followed his seminal review of two-dimensional electron gases (2DEGs) in semiconductors [33] by treating the same problem in graphene [34]. Figure 1.1 displays a model of the graphene lattice in juxtaposition with the 3 other most commons form of sp^2 hybridized carbon. Each of these graphenic materials can be thought as a particular arrangement of graphene with different boundary conditions and hence altered dimensionality, as shown in Figure 1.1.

Graphene is composed of a honeycomb crystal lattice of carbon atoms in the sp^2 hybridized electron configuration. The sp^2 hybridization involves a mixing of the $2s^2$, p_x, and p_y electron orbitals into three in-plane sp^2 electron orbitals with trigonal-planar symmetry. The formation of the sp^2 orbitals releases a $2s$ electron to occupy the out-of-plane p_z electron orbital. The mechanical properties of graphene can be attributed to extremely strong covalent bonding between the sp^2 electron orbital (σ bonds), while the conjugated network of p_z electrons (π bonds) are responsible for the electronic properties. The mechanical strength of the σ is a consequence of the considerable overlap between two sp^2 orbitals, which means that the electron charge density is highly localized between separate carbon nuclei. The p_z electron orbitals between neighboring carbon atoms form weakly-coupled π bonds because they extend vertically out of the graphene plane with very little orbitals overlap. Therefore, the covalent nature of the π bond is much weaker than the covalent nature of σ bonds, enabling electrons in the conjugated graphene π bond network to tunnel between

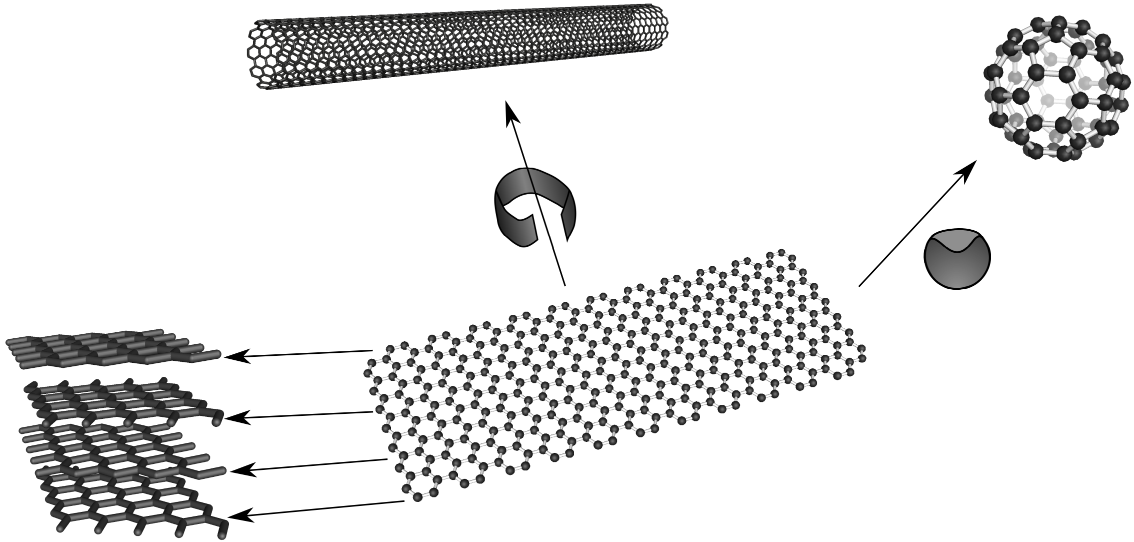

Figure 1.1: Schematic demonstrating how graphene is the fundamental building block of graphite (stacking), carbon nanotubes (rolling), and spherical fullerenes like C_{60} (wrapping).

neighboring lattice sites.

This simple π bond network model of conduction electrons in graphene also explain why the 'tight-binding' approach to calculating the graphene band structure (and the band structure of other fullerenes) is so successful [20, 21, 23]. The tight-binding approximation assumes that the material is crystalline so that Bloch's Theorem is applicable [35] and that the conduction electrons are 'tightly' bound to the atomic nuclei in the lattice with only a weak-overlap between neighboring electron orbitals. When this is true, electron wave functions can be modeled as a superposition of the atomic wave functions at each lattice site. Because the electronic configuration of carbon is well-understood it is conceptually easy to calculate the band structure for sp^2 hybridized carbon materials.

The delocalized nature of the π electron in graphene only explains the origin of the conduction electrons in graphene. The graphene crystal lattice appears to be hexagonal in-plane, but it is most accurately described as a bipartite triangular

lattice (Fig. 1.2). The carbon atoms in graphene can be ascribed to one of two inversion-symmetric triangular sublattices, typically referred to as sublattice A and sublattice B. The symmetry of the graphene crystal appears hexagonal because the carbon atoms in sublattice B are rotated by 180 degrees with respect to the carbon atoms in sublattice A. One choice of lattice vectors is:

$$\mathbf{a_1} = a\sqrt{3}\hat{x}/2 + 3a\hat{y}/2, \;\; \mathbf{a_2} = -a\sqrt{3}\hat{x}/2 + 3a\hat{y}/2 \tag{1.1}$$

where $a = 2.46\,\text{Å}$ is the lattice constant for each sublattice, and $\delta = 1.42\,\text{Å}$ is nearnest neighbor bond length between carbon atoms from separate sublattices. Unlike most bipartite crystal lattices, the two sublattices in graphene are both occupied by the same element and thus in most cases are indistinguishable. The indistinguishability and symmetry of the two carbon sublattices in graphene is necessary to explain the unique electronic properties of this material.

In this treatment of the graphene band structure I will follow the conventions established by Bena [36]. In particular, the position of the unit cell is given by the positions of the A sublattice atoms $\mathbf{R}_j^A = \mathbf{R}_j = n\mathbf{a_1} + m\mathbf{a_2}$, and the positions of the B sublattice atoms is $\mathbf{R}_j^B = \mathbf{R_j} - a\hat{y}$. In this formulation of the problem, the atomic wave functions from the A and B atoms are combined to form a single Bloch function per unit cell:

$$|\Psi(\mathbf{r},\mathbf{k})\rangle = \frac{1}{\sqrt{N}} \sum_j e^{i\mathbf{k}\cdot\mathbf{R_j}} [c^A(\mathbf{k}) \left|\phi(\mathbf{r} - \mathbf{R_j^A})\right\rangle + c^B(\mathbf{k}) \left|\phi(\mathbf{r} - \mathbf{R_j^B})\right\rangle] \tag{1.2}$$

where N is the number of unit cells, and $\phi(\mathbf{r})$ are the wave functions of the π electron orbitals. The coefficients $c^{A/B}$ are chosen to ensure that Ψ^k is an eigenstate of the tight-binding Hamiltonian:

$$\mathcal{H} = -t \sum_{<i,j>} (\left|\phi_j^A\right\rangle \left\langle\phi_i^B\right| + h.c.) \tag{1.3}$$

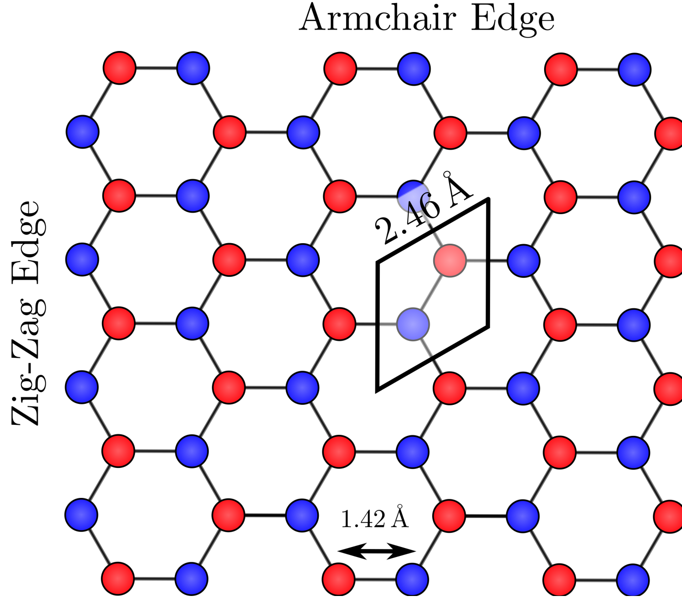

Figure 1.2: The graphene crystal lattice, with the A and B sublattices denoted by colored atoms. The graphene unit-cell (2.46 Å) contains one atom from each sublattice.

where $t \approx 3\,\mathrm{eV}$ is the tight-binding hopping amplitude for graphene. Solving for the eigenfunctions of $c^{A/B}$ using Equation 1.3 and evaluating $\left\langle \phi_j^l \right| \mathcal{H} \left| \Psi^k \right\rangle$ $(l = A, B)$ gives the coupled equations:

$$
\begin{aligned}
\epsilon(\mathbf{k})\, c^A(\mathbf{k}) &= -t(e^{-i\mathbf{k}\cdot\mathbf{a_1}} + e^{-i\mathbf{k}\cdot\mathbf{a_2}} + 1)\, c^B(\mathbf{k}) = f(\mathbf{k})\, c^B(\mathbf{k}) \\
\epsilon(\mathbf{k})\, c^B(\mathbf{k}) &= -t(e^{i\mathbf{k}\cdot\mathbf{a_1}} + e^{i\mathbf{k}\cdot\mathbf{a_2}} + 1)\, c^A(\mathbf{k}) = f^*(\mathbf{k})\, c^A(\mathbf{k})
\end{aligned}
\tag{1.4}
$$

which determines the matrix formulation of the effective tight binding Hamiltonian:

$$
\mathcal{H}(\mathbf{k}) = \begin{pmatrix} 0 & f(\mathbf{k}) \\ f^*(\mathbf{k}) & 0 \end{pmatrix} \tag{1.5}
$$

This yields the energy eigenvalues for the Hamiltonian, which is equivalent to the energy dispersion relationship for graphene:

$$
\epsilon(\mathbf{k}) = \pm\sqrt{3 + 2\cos\left(\sqrt{3}k_x a\right) + 4\cos(\sqrt{3}k_x a/2)\cos(3k_y a/2)} \tag{1.6}
$$

The band structure of graphene within the 1st Brillouin zone is plotted in Figure 1.3 using equation 1.6. The two π orbitals in each graphene unit cell form two different π bands: a bonding or valence band (π) and an anti-bonding or conduction band (π^*). Each p_z orbital only contributes one electron each so that the low energy valence band is completely filled but the conduction band is empty. The most characteristic feature of the graphene band structure is that the conduction and valence bands touch at 6 reciprocal space points near the edge of the graphene Brillouin zone. Therefore, graphene is a zero band gap, undoped semimetal. The conduction and valence bands touch at the high symmetry $\mathbf{K}$ and $\mathbf{K}'$ points where $\epsilon = 0$, which is defined as the Dirac point. In the low energy limit near the K points ($\mathbf{k} = \mathbf{K}+\mathbf{q}$) the charge carriers have a linear energy dispersion:

$$\epsilon(\mathbf{q}) = \pm\hbar\left(\frac{3ta}{2\hbar}\right)|\mathbf{q}| = \pm\hbar v_F|\mathbf{q}| \tag{1.7}$$

where the Fermi velocity $v_F \approx 10^6$ m/s is a *constant* defined by the lattice constant a and hopping parameter t. The eigenstates in the low-energy limit can be defined by a two-component wave function mathematically similar to a spinor:

$$|\Psi(\mathbf{q})\rangle = \begin{pmatrix} \Psi^A \\ \Psi^B \end{pmatrix} = \frac{1}{\sqrt{2}}\begin{pmatrix} 1 \\ \pm e^{i\theta(\mathbf{q})/2} \end{pmatrix} \tag{1.8}$$

The two components of the eigenstates refer to the A and B sublattice contributions to Bloch function, $\theta(\mathbf{q}) = \arctan(q_y/q_x)$ and the $\pm$ sign correspond to the π and π^* bands, respectively. The eigenstates are quantified to within an additional phase factor of $e^{i\theta(\mathbf{k})}$, so there exist valid solutions to the tight-binding Hamiltonian which consist of states on only the A or B sublattices. This degree of freedom is called the 'pseudospin' in order distinguish between the intrinsic 'spin' of the electrons themselves.

Equation 1.7 demonstrates the striking fact that the low-energy quasiparticles

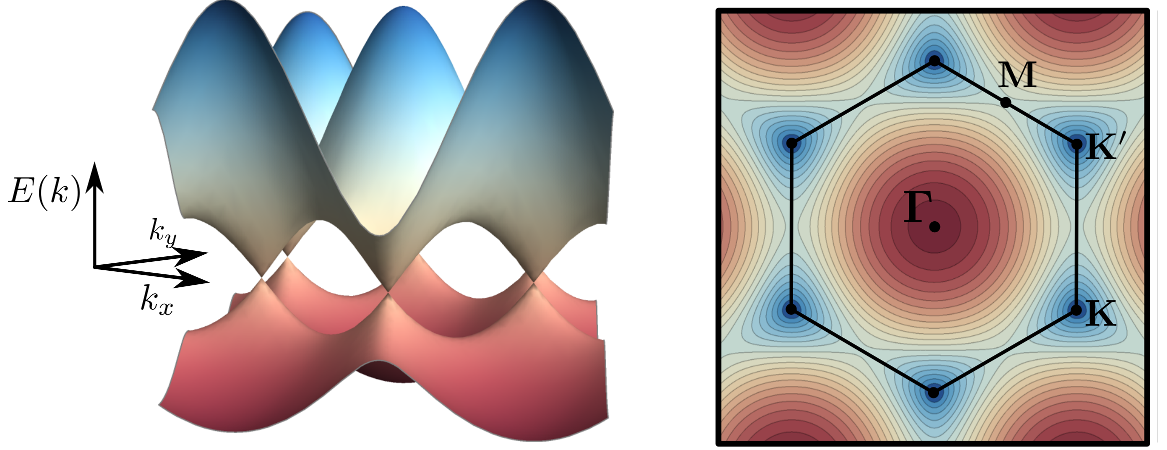

Figure 1.3: Graphene band structure calculated using the near-neighbor tight-binding approximate [4].

in graphene behave like massless, relativistic fermions which travel at a constant velocity v_F. The Fermi velocity in most materials is a function of the charge carrier momentum, and the energy dispersion usually follows the quadratic form given by Schrödinger's equation for massive particles [37]. Equation 1.7 is independent of *which* Dirac point ($\mathbf{K}$ or $\mathbf{K}'$) the low-energy expansion is performed, which implies a valley degeneracy for electrons near these points. Although the electron states at the $\mathbf{K}$ and $\mathbf{K}'$ are degenerate, the wave functions at these points are inequivalent. If the low-energy expansion is performed separately for the $\mathbf{K}$ and $\mathbf{K}'$ points $f(\mathbf{k}) \rightarrow f_\xi(\mathbf{q}) = \hbar v_F(\xi q_x - iq_y) = v_F(\xi p_x - ip_y)$, where $\xi = \pm$ for the $\mathbf{K}$ and $\mathbf{K}'$ points, respectively, and $\mathbf{p} = \hbar\mathbf{q}$. The Hamiltonian must be expanded into a 4×4 space to encompass the $\mathbf{K}$ and $\mathbf{K}'$ subblocks:

$$\mathcal{H}(\mathbf{q}) = \begin{pmatrix} 0 & f_+ & 0 & 0 \\ f_+^* & 0 & 0 & 0 \\ 0 & 0 & 0 & f_-^* \\ 0 & 0 & f_- & 0 \end{pmatrix} = \begin{pmatrix} v_F\mathbf{p}\cdot\boldsymbol{\sigma} & 0 \\ 0 & v_F\mathbf{p}\cdot\boldsymbol{\sigma} \end{pmatrix} \tag{1.9}$$

This low-energy effective Hamiltonian can be written using a more compact notation:

$$\mathcal{H}_{4\mathrm{D}} = \mathcal{H}_{2\mathrm{D}} \otimes \tau_0 = v_F[\mathbf{p} \cdot \boldsymbol{\sigma}] \otimes \tau_0 \tag{1.10}$$

where $\boldsymbol{\sigma}$ are the 2-dimensional Pauli matrices, and τ_0 is the 2×2 identity matrix used to include the valley degree of freedom [38]. With the definition of the momentum operator as $\mathbf{p} = -i\hbar\nabla$, the Hamiltonian is shown to be equivalent to the four-dimensional Dirac equation (a 2D Dirac equation for each valley). The mapping of the low-energy electronic states in graphene to the Dirac equation explains why the ($\mathbf{K}$ or $\mathbf{K}'$) are known as the Dirac points. More importantly, it implies that the low-energy quasiparticles in graphene behave analogously to massless, charged Dirac fermions that travel at a fraction of the speed of light. Indeed, much of the low-energy physics which has been studied in graphene can be understood from the point of the view of the Dirac equation. The identification of the low-energy quasiparticles that behave like massless, Dirac fermions has been experimentally confirmed in measurements of the Shubnikov-de Haas oscillations and the half-integer Quantum Hall Effect (QHE) [8, 39–41], and by measurements of the graphene band structure using scanning tunneling spectroscopy [42] Angle-Resolved Photoelectron Spectroscopy (ARPES) [43, 44].

1.2.1 Chirality and Backscattering Suppression

The suppression of backscattering in graphene is a direct consequence of the low-energy electronic structure of this material, which can be expressed in terms of the Dirac equation for massless fermions (Eqn. 1.10). We can define the quantum-mechanical *helicity* or *chirality* operator $\hat{\mathbf{h}}$ as the projection of the a particle's spin onto the direction of propagation:

$$\hat{\mathbf{h}} = \frac{1}{2}\boldsymbol{\sigma}\cdot\frac{\mathbf{p}}{|\mathbf{p}|} \tag{1.11}$$

The chirality operator commutes with the 2D Dirac Hamiltonian $\mathcal{H}_{2D}$, and therefore it is a good quantum number for the low-energy massless Dirac quasiparticles in graphene and this quantity is conserved. This operator is well known in high-energy physics, where it is invoked to explain the 'left-handedness' of neutrinos (spin anti-parallel to momentum) and the 'right-handedness of anti-neutrinos (spin parallel to momentum) [45]. For neutrinos the chirality is with respect to the neutrino's intrsinsic spin, but in graphene the chirality refers to the conservation of the 'pseudospin' or sublattice degree of freedom. For the effective Dirac fermions in graphene, $\hat{\mathbf{h}}\Psi_\xi = \xi\lambda\frac{1}{2}\Psi_\xi$, where ξ is the valley index (+ for $\mathbf{K}$, - for $\mathbf{K}'$) and λ is the band index (+ for conduction band, - for valence band). Figure 1.4 schematically shows how the chirality of a Dirac fermion in graphene changes for the different bands and valleys. The conservation of chirality for the charge carriers in graphene implies that they are protected from backscattering for long-range forces (ie. Coulomb force). Backscattering implies very large momentum changes, so that Dirac quasiparticles can only backscatter from the $\mathbf{K}$ valley into the $\mathbf{K}'$ valley (or vice versa). However, the electrons/holes in the $\mathbf{K}$ have the opposite chirality of the electron/holes in the $\mathbf{K}'$, so this scattering channel is forbidden [30]. The suppression of backscattering is spectacularly evidenced in the Klein tunneling [46] of charge carriers across graphene PN junctions. In graphene, electrons incident on a PN junction only are allowed to scatter into either electron states moving in the same direction or hole states moving in the opposite direction. Every other scattering channel involves a change in the pseudospin of the original state, which is only possible for very short-range potentials (on the scale of the C-C bond length between the neighboring A and B sublattic sites). Therefore, carriers travelling towards PN junction (square potential barrier) at near normal incidence are perfectly transmitted [47].

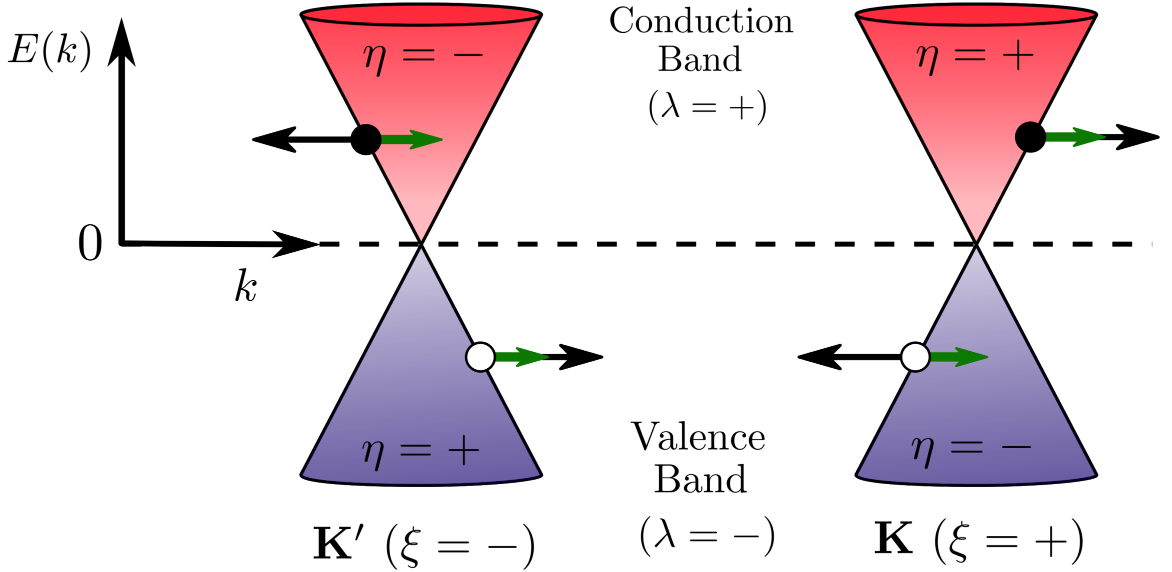

Figure 1.4: Chirality and pseudospin conservation in graphene. The black arrows refer to momentum, and the green arrows pseudospin. The chirality of a quasiparticle in graphene is determined by the band index λ and the valley index ξ, where the chirality eigenvalue $\eta = \xi\lambda$

Backscattering suppression has important implications for charge transport in graphene when doped near the Dirac point. Graphene devices on SiO_2 possess room temperature electron/hole mobilities of between 5000 $cm^2/V \cdot s$ - 20000 $cm^2/V \cdot s$ even the prescence of disorder (ie. Coulomb impurities). In comparison, the electron mobility of bulk n-type silicon is only 1450 $cm^2/V \cdot s$ [48]. The high mobility of charge carriers in grapheen in the presence of disorder is directly attributable to a near-total lack of carrier backscattering [49], in addition to the very low instrinsic electron-phonon coupling in graphene [50, 51]. The measured transport mobility at room temperature is still much lower than the theoretically predicted carrier mobility of 200000 $cm^2/V \cdot s$ because of the comparatively stronger electron-phonon coupling between the carriers in graphene and nearby materials (ie. substrate and/or gate oxide) [52]. This was confirmed by more recent measurements using suspended graphene devices [53, 54, 54, 55] or graphene deposited onto boron nitride [56**?**]. Even greater graphene mobilities have been measured using magneto-optical spectroscopy

for faulted graphene layers embedded in bulk graphite [57] or multilayer epitaxial graphene grown on SiC($000\bar{1}$) [58]. Unfortunately, the ballistic charge conduction in graphene comes at a price: graphene FETs have very poor ON/OFF ratios because of the Klein tunneling effect. Therefore, intrinsic graphene is a very poor material for low-frequency FET devices.

1.2.2 Half-integer Quantum Hall Effect

Any two-dimensional electron gas (2DEG) in an out-of-plane magnetic field will form quantized cyclotron orbits known as Landau levels, which are capable of forming because the motion of the particles is constrained in the plane. The motion of a particle in a cyclotron orbit is mathematically equivalent to a 2D harmonic oscillator, so the quantum mechanical solution of this canonical problem is applicable to the case of of a 2DEG in a magnetic field. In traditional 2DEGs like Al-GaAs the charge carriers are massive quasiparticles described by the Schrödinger equation, and so the energy levels of these states are equidistant in energy and possess equal degeneracy.

$$E_N^S = \hbar\omega_c(N + 1/2) \tag{1.12}$$

The factor $\omega_c = eB/m$ is the classic cyclotron frequency for a charged particle of mass m in magnetic field of strength B, and $N = 0, 1, 2, \ldots$ is the Landau level index. It is clear that in the normal 2DEGs the Landau level spacing is linear in both the level index and the magnetic field strength. For high mobility 2DEG samples at 2.3 K or lower it is possible to measure the quantum hall effect (QHE) in an applied perpendicular magnetic field. The QHE is a consequence of Landau level formation, and is expressed as quantized integer conductance values versus changes in the Fermi energy of the material. The values of the quantized Hall conductance are determined by the occupancy of each Landau Level. In general the Landau level occupancy, or 'filling factor', is equal to $g_s(e^2/h)$, where the factor $g_s = 2$ stems from the spin

degeneracy of the 2DEG.

Graphene is an unusual 2DEG because the low-energy quasiparticles behave like massless, Dirac fermions, which form Landau levels with a non-equidistant energy spacing.

$$E_N^D = \lambda v_F \sqrt{2e\hbar B|N|} \tag{1.13}$$

In graphene the energy gap between lowest Landau Level ($N = 0$) and the next highest Landau level ($N = \pm 1$) is large enough that the QHE is observable at room temperature in reasonable magnetic fields. The lowest Landau level in graphene is unique; it is pinned at the Dirac point, it consists equally of electrons and holes, and the $N = 0$ quantum states are both valley- and pseudospin-polarized. In addition, the Hall conductance plateaus observed in the QHE for graphene occur at half-integer quantized values [45]:

$$\sigma_{xy} = \frac{I}{V_H} = g_v g_s (N + 1/2) \frac{e^2}{h} \tag{1.14}$$

where $g_v = 2$ and $g_s = 2$ for the spin and valley degeneracies. The non-equidistant energy spacing and the half-integer QHE in graphene is a direct consequence of magnetic orbital quantization of a 2D massless, charged Dirac gas. In particular, this behavior stems from a non-zero geometric or Berry's phase in graphene. As clearly shown in the functional form of the Dirac Hamiltonian eigenstates (Eq. 1.8), low-energy quasiparticles which move adiabatically in circular orbits accrue an additional wave function phase of $\theta = \pi$. The Berry's phase π implies that semi-classical, quantized cyclotron orbits in graphene must be an odd-number of half-wavelengths in circumference for the wave function to be continuous, because the additional half-wavelength is accrued automatically. This 'half-wavelength' condition leads to the half-integer form of the QHE in graphene.

CHAPTER II

METHODS

2.1 Sample Preparation

The quality and size of silicon carbide (SiC) wafers has increased dramatically in recent history. Until thirty years ago, SiC was only produced in very small quantities as a byproduct of the Acheson method where coke and silica are heated in an electric smelting furnace to form amorphous silicon carbide [59]. The Acheson method usually only produces microcrystalline SiC, although sometimes larger crystal 'platelets' can form in voids between the source materials [60]. The search for SiC electronics officially began when Lely revealed his physical vapor transport (PVT) method for growing relatively large SiC platelets ($1\,\mathrm{cm}^2$) in 1955 [61]. This discovery incited the electronics industry as well as many independent researcher to express interest in replacing the nascent silicon electronic material with SiC. William Shockley, one of the inventors of the transistor, supported SiC (and carbon) electronics in a statement at the First International Conference on Silicon Carbide in 1959 [62]:

> Now the big question is this: How is the problem of high temperature going to be solved? What are the horses to put one's money on?... One approach is the logical sequence we see here: Ge, Si, SiC, C in that sequence...

SiC is attractive because it has a wide band gap (depending on the material polytype) and excellent thermal stability and conductivity, which in turn allows the material to operate as a semiconductor at temperatures as high as $800\,^\circ$C [63]. The incredible hardness of SiC, which is only slightly less than diamond, originates from the strong Si-C covalent bonds in the material. The hardness of SiC also contributes to the radiation insensitivity of the material, which has made SiC electronics a prime

candidate for the aerospace industry to this day [64]. Unfortunately, the success of SiC was halted by the problem of forming larger and higher-purity SiC crystal using the Lely method [65]. The quality and size of silicon semiconductor wafers continued to increase and this material was eventually adopted despite it's many intrinsic limitations [60].

SiC research was jump started yet again in 1978 by the modified PVT method which employs seed crystals to increase the growth rate [66]. The seed crystal assisted PVT growth, refined by various researchers, enabled the preparation of large boules of SiC in the late 1980s [67–70]. Chemical-vapor deposition (CVD) of SiC thin-films onto Si or SiC substrates is another popular method for making SiC devices [65], and more recently high-temperature CVD methods have achieved similar growth rates and comparably lower impurity levels [63]. Thin-film growth techniques benefit from not needing to cut a large SiC boule into a flat wafer, which is difficult for SiC because it is such a hard material [65]. Cree Research Inc. began to manufacture 25 mm diameter SiC wafers in 1989, and today there are multiple companies producing high-quality electronic grade SiC [63]. As the size of silicon carbide wafers increased, it became increasingly clear that the material was plagued by a variety of defects. Intrinsic defects in SiC include threading screw dislocations and, the related and even more troublesome, micropipes which can form around these screw dislocations [60]. Crystal growers have optimized SiC growth parameters in recent years, and today 150 mm diameter, low micropipe density carbide wafers are commercially available [63]. While other kinds of intrinsic defects persist in modern day silicon carbide wafers (stacking fault induced multiple polytypism, threaded edge dislocations, step bunching, etc.), the overall quality/cost ratio of the material has improved to such a point that SiC has become a commercially viable substrate for efficient III-nitride light-emitting diodes [60] and and as the active element high power electronics [71–73].

Silicon carbide wafers can also suffer from extrinsic defects. Extrinsic defects are those that occur due to processing and handling steps after crystal growth. These extrinsic defects often manifest in the form of surface roughness such as scratches (short wavelength height variations), dimples (long wavelength height variations), or step bunches (periodic height variations). Scratches and dimples can form during lapping and polishing planarization processing steps. Step bunches are unique in that they can occur as either extrinsic or intrinsic defects, although intrinsic step bunching is largely unimportant since the SiC wafers are often polished after growth. Improperly polishing silicon carbide can also result in subsurface defects, such as stacking faults and dislocations [70, 74, 75]. Global doping in SiC is often achieve by directly introducing the dopant into the furnace during growth, but local doping of SiC is often achieved using high energy ion-implantation followed by a relatively high temperature annealing step. Ion-implementation is necessary because high-temperature diffusion is a very slow, inefficient process in SiC [76]. Both the ion-implantation and annealing steps can cause significant surface roughening and internal damage to the crystal lattice [60, 77, 78].

To study the growth of epitaxial graphene on silicon carbide, and in general the growth of all thin-film materials, it is important to prepare the initial substrate by tailoring the number of defects across the surface. Intrinsic defects such as vacancies and step edges clearly impact the growth of epitaxial graphene because they dominate the global sublimation rate due to atomic desorption. Desorption is favored near crystalline defects because nearby atoms possess dangling bonds and are in a higher energy state compared to atoms with fully saturated bonding. Extrinsic defects such as scratches should alter the local silicon sublimation rate in a similar manner; by changing the surface step-flow dynamics that strongly impact epitaxial graphene growth. Defects can also act as a local nucleation site for crystal formation by statistically reducing the mobility of nearby adatoms and making them more

susceptible to additional atom capture [79, 80]. In general adsorbed molecules are less mobile than single adatoms, and in certain deposition regimes (ie. temperature, incident flux, etc.) there exists a critical size after which an adatom island becomes pinned to the substrate [81–84]. In many system the critical size increases as a function of temperature, proceeding from monomers at very low temperature to dimers, trimers, etc [85]. Curiously, five-atom (pentamer) graphene clusters on ruthenium remain mobile and stable islands are formed only when six pentamers join together [86, 87].

We have focused on using various sample preparation techniques to prepare the silicon carbide surface for epitaxial graphene growth. The two SiC wafers used in this study were purchased from Cree Research Inc., and were subsequently diced into 3.5 x 4.5 mm samples using the wafer cutting facilities in the cleanroom at Georgia Techs Institute of Electronics and Nanotechnology (IEN). Wafer H (50 mm diameter) was doped $6H-SiC(0001)$ with double-sided mechanical polishing. Wafer L (75 mm diameter) was semi-insulating $4H-SiC$ with normal mechanical polishing on the SiC(0001) surface and chemical mechanical polishing (CMP) on the SiC($000\bar{1}$) surface. Epitaxial graphene growth studies were carried out on CMP SiC surfaces or hydrogen etched SiC surfaces. Hydrogen etching is a common technique for forming atomically flat SiC terraces with very straight steps on CMP or mechanically polished surfaces [88]. The following subsections will discuss simple mechanical polishing, CMP, and hydrogen etching sample preparation techniques. The final subsection will introduce a hybrid technique known as dimple grinding, which was used in conjunction with hydrogen etching to prepare off-axis SiC surfaces on a nominally on-axis wafer.

2.1.1 Mechanical and Chemical Mechanical Polishing

Semiconductor wafers are mechanically lapped and polished after they are cut from a large boule of high-purity material. The wafer is sliced from the boule using a

diamond saw blade, which leaves the surface roughened and the near-surface region damaged with crystalline defects, macroscopic cracks, and non-uniform stress in the crystal [89]. Lapping and polishing are used to micromachine the surface and near-surface regions of the wafer to achieve better electronic device performance. Lapping involves the use of an abrasive to mechanically remove large amounts of material and reduce the thickness of a wafer. The primary objective of lapping is often to improve the uniformity of the wafer thickness [90]. The abrasive usually consists of a hard mineral grit either mixed into a colloidal solution known as a slurry, or bonded onto the surface of flexible substrate. The grit is worked against the wafer using a durable, metallic lapping wheel operated at constant speed and pressure. Increasing the grit size, wheel speed, and wheel pressure increases the material removal rate (MRR), but it also increases the surface roughness damage [91].

A correctly lapped wafer surface has less damage than a wafer cut directly from the boule. Complete removal of the surface roughness and near-surface damage is accomplished by polishing. Polishing resembles slurry-based lapping, except the hard metallic wheel is covered or replaced by a pliant polishing pad. The polishing pad spreads the wheel pressure more evenly across the wafer surface and soaks up the abrasive slurry which is either continuously or periodically refreshed [89]. The lapping and polishing steps are implemented in steps of ever reducing severity. During the lapping and initial polishing steps, the MRR is fast but the surface and near-surface damage remains high. During the final polishing steps the MRR is gradually decreased by reducing the size of the grit and the operating speed/pressure of the polishing wheel. This gradual process eliminates the majority of surface and near-surface damage [90]. With larger grit sizes and high wheel rotation rate and pressure, material is removed via a brittle fracture mechanism which leaves an imprint on the surface. With small enough grit, slow rotational velocity, and low pressure, the polishing reaches a transition point where a ductile removal process dominates [92]. The

ductile polishing regime is desirable because it results in a very smooth surface and very little near-surface damage. Ductile polishing leaves an amorphous surface layer which may not be ideal for further processing steps, such as surface epitaxial growth. It is also possible for crystal dislocations and stacking faults to persist after careful mechanical polishing in the ductile regime. Amorphous layers and crystal defects are often removed from silicon wafers by high temperature oxidation followed by an HF oxide etch [93].

One downside of simple mechanical polishing is that it is difficult to achieve atomically flat surfaces on extremely hard and brittle materials such as sapphire or SiC. Figure 2.1 is an atomic force microscopy (AFM) image of the mechanically polished $4H$ and $6H$ SiC(0001) sample surfaces used in this thesis. The initial root mean square (RMS) surface roughness of the mechanically polished surfaces was 0.92 nm), and consists mainly of randomly oriented, straight scratches as deep as 8 nm. As noted above, the only way to achieve atomically flat surfaces with mechanical polishing is to sequentially reduce the grit size past the ductile polishing regime [92, 94]. The critical cutting depth for SiC is on the order of 0.1 μm so ductile removal occurs during the final polishing stages, but SiC is so hard (Moh's Hardness of 9.5) and brittle that even ultra-fine diamond polishing compounds (Moh's Hardness of 10) are unable to achieve atomic-scale planarity [95].

CMP is a hybrid method that combines chemical etching and simple mechanical polishing in which a relatively soft abrasive grit is suspended in slurry containing a reactive chemical solution [89], and is now the standard method for the planarization of essentially every material used in the semiconductor industry [89, 96], including SiC [70]. During CMP the chemical solution reacts with the wafer surface to form a softer material, which is then removed by the abrasive. Material is preferentially removed from asperities on the wafer resulting in atomically smooth surfaces and very little near-surface damage because the soft abrasive can only impact the relatively

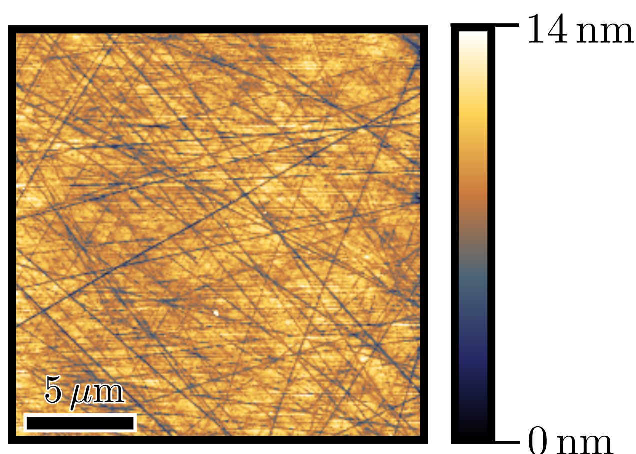

Figure 2.1: AFM topography measurements of the as-received hexagonal SiC samples purchased from Cree Research, Inc. (a) Simple mechanical polishing with a diamond based slurry leaves the SiC with residual, randomly oriented scratches that are up to several nanometers deep.

soft oxide which forms during processing. The soft abrasive cannot effectively damage the wafer surface before the surface reacts with the chemical solution. In addition, the heat generated by the friction between the wafer and polishing pad thermally activates the chemical reaction of the substrate [96]. Silicon wafer CMP is perhaps the prototypical and most well-known example of the CMP method. Silicon dioxide nanoparticles are mixed with a highly concentrated alkaline solution (pH 10-11) to form a basic colloidal silica suspension. The alkaline agent oxidizes the silicon surface, which is then worn away by the silica abrasive [97]. CMP on chemically inert and thermally resistant materials like SiC is limited by very slow oxidation rates [98]. The use of a normal alkaline colloidal silica slurry for polishing silicon wafers results in a MRR of much less than $1\,\frac{\text{um}}{\text{hr}}$ on SiC wafers [75]. However, in many cases only a single CMP step is required so the overall planarization process is faster and more reproducible. Modifications to standard silicon CMP have achieved atomic-scale planarity at reasonably high MRR by replacing silica grit with a harder material such as alumina [99], adding strong oxidizers into the solution [100],, or including specially-prepared diamond nanoparticles [101].

2.1.2 Hydrogen Etching

Before CMP for SiC was made more practical, hydrogen etching was the only method for preparing atomically flat SiC surfaces. Planarization of SiC via hydrogen etching resembles epitaxial graphene growth of SiC [102]. At temperatures between $1200\,^\circ\mathrm{C} - 1800\,^\circ\mathrm{C}$ in UHV or an inert atmosphere SiC decomposes primarily by monoatomic silicon sublimation [103–105]. High-temperature annealing of crystals promotes rapid step-flow which quickly alters the initial surface morphology. A spectacular example of this behavior is observed in the Si(111) surface, which will form unit-cell, triple unit-cell, or step bunched surfaces depending upon the initial crystal facet and morphology [106, 107]. Step-flow assisted planarization of SiC is complicated by the formation of graphene which accumulates amidst silicon sublimation [108]. The graphene buffer layer on SiC(0001) appears to pin SiC steps, perhaps contributing to the severe surface roughening observed in the system [109, 110]. The situation is less clear for SiC($000\bar{1}$), but this surface also suffers from surface roughening during high-temperature sublimation and graphene growth [111]. Graphene related surface roughening is avoided if the SiC is heated in a hydrogen rich environment. The hydrogen reacts with surface carbon to form simple gaseous hydrocarbons and passivates the bare SiC surface [112]. At high temperatures the graphene-free SiC surface steps flow unimpeded and can repair residual polishing damage [88, 108, 112].

The literature suggests an incredible range of possible hydrogen etching process parameters depending upon the SiC surface termination, polytype, and initial surface condition. Etching with hydrogen gas has been accomplished with temperatures from $1275\,^\circ\mathrm{C}$ for $3\mathrm{C} - \mathrm{SiC}$) [113] to as high as $1750\,^\circ\mathrm{C}$ for defective, early generation Lely platelets [112]. Hydrogen gas pressures range from 50 mbar to atmospheric pressure [108, 112–114]. Some groups work with non-flammable mixtures of hydrogen and argon, which reduces the etch rate while simultaneously restricting silicon sublimation from the crystal surface [115]. One major reason for the disparity in the

hydrogen etching parameters employed by different laboratories is that the etching process is sensitive to the furnace material and furnace history. It is very common to use graphite furnaces for hydrogen etching and other high temperature SiC processes. Unfortunately, the hydrogen will etch both the SiC and graphite furnace itself. The overabundance of gaseous hydrocarbons which results from etching the graphite furnace walls reduces the etching rate of the SiC to maintain chemical equilibrium [114–116]. To prevent excess hydrocarbon buildup it is common to use boron nitride, tantalum carbide, or even SiC coated graphite furnaces for hydrogen etching [114]. It is also common to see tantalum or molybdenum furnaces because these materials enhance the hydrogen etching process [117].

Hydrogen etching of SiC is difficult to optimize because it is necessary to balance the net quantity of both silicon and carbon removed from the surface. At high hydrogen pressure/flow rates and relatively low temperatures carbon etching is rapid relative to the rate of silicon sublimation leading to an accumulation of silicon adatom across the substrate in the form of large silicon droplets [78]. These silicon droplets act as a local SiC etching mask and roughen the final surface [115]. At very high furnace pressures, flow rates, and temperatures the carbon etching rate and the silicon sublimation rate are similar enough to prevent silicon droplet formation [116]. Nevertheless, at temperatures above approximately 1550 ° C the hydrogen etched SiC tends to form large step bunches with atomically flat terraces [118]. Step bunches are problematic for traditional semiconductor electronics, but for epitaxial graphene the stability of large steps on SiC have been utilized to fabricate sidewall nanoribbons [119].

Two different hydrogen etching furnaces were utilized for preparing SiC surface for graphene growth. The first was a small, custom-built tantalum hydrogen etching furnace picture in Figure 2.2a [120]. Hydrogen etching was performed using a 3% hydrogen/argon mixture at atmospheric pressure, flowed at a rate of 2.4 SLPM

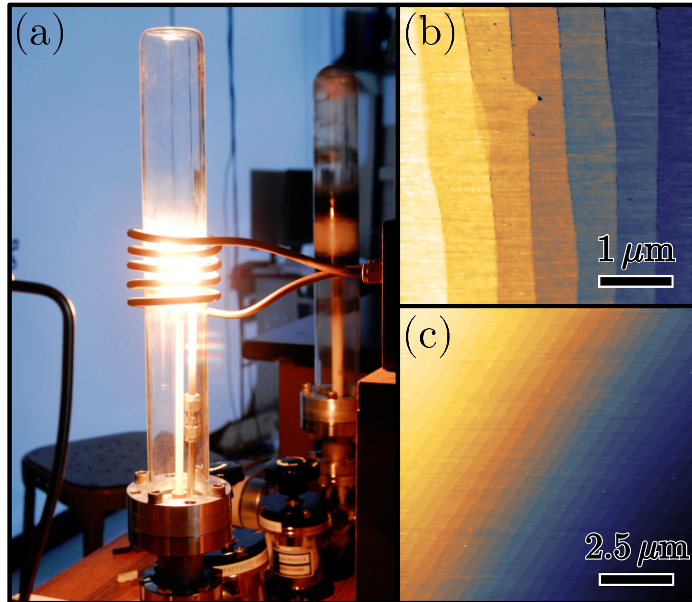

Figure 2.2: (a) Picture of the custom tantalum thin-wall hydrogen etching furnace, which can prepare both (b) single unit-cell and (c) half unit-cell 6H SiC(0001) surfaces (measured by AFM) depending upon the etching recipe and initial surface conditions.

(standard liter per minute). The furnace temperature was operated between 1400 ° C and 1450 ° C to prevent unwanted furnace deterioration [121]. 4H SiC surfaces hydrogen etched in the custom hydrogen etching furnace had straight, unit-cell high steps separating atomically flat terraces as determined by AFM (not shown). 6H SiC surfaces hydrogen etched in the same manner usually exhibited unit-cell high steps (Fig. 2.2b), although sometimes samples would possess half unit-cell steps (Fig. 2.2c) [88].

Figure 2.3 show the second type of furnace used for hydrogen etching: a commercial First Nano Graphene (FNG) furnace (CVD Corporation, Islip, NY)[1]. The FNG furnace consists of a large graphite furnace/susceptor which can accommodate 100 mm diameter substrates and has three gas injection ports connected to hydrogen, argon, methane, and silane cylinders. The recipe used with the custom hydrogen etching furnace is not effective in the FNG, leaving SiC surfaces relatively unchanged from

[1]Maintained by the Georgia Tech Nanotechnology Research Center in the Marcus Building Inorganic Cleanroom

Figure 2.3: Commercial First Nano Graphene Furnace (Easy Tube 3000), capable of heating up to 100 mm diameter substrates up to 2200 ° C in various environments. The inset is an AFM image of a 4H SiC(0001) substrate hydrogen etched in this furnace, displaying smooth and straight 8.43 ± 2.68 nm high step bunches (scale bar is 20 um)

their original surface preparation (see Section 2.1.1). The very large and uncoated graphite furnace most likely reacts with the hydrogen gas to form a large background pressure of hydrocarbon, which inhibits the hydrogen etching of SiC samples [114–116]. A new hydrogen etching recipe was developed with the FNG furnace to generate atomically flat terraces separated by large step bunches. These samples were etched in 1 bar of hydrogen gas at a furnace temperature of 1800 ° C, flowed at 1.0 SLPM. On-axis SiC samples hydrogen etched in the FNG using this recipe had a significant amount of step height variation (8.43 ± 2.68 nm). Off-Axis SiC samples prepared via dimple grinding had much less step meandering than the as-received on-axis samples, possibly because of long-range interactions between steps inside the SiC dimple (see Section 2.1.3)

2.1.3 Dimple Grinding

Spherical, concave depressions were machined into SiC wafer samples (3.5 mm $\times$ 4.5 mm $\times$ $0.250 - 0.350$ mm) using a specialty grinding instrument known as a dimple

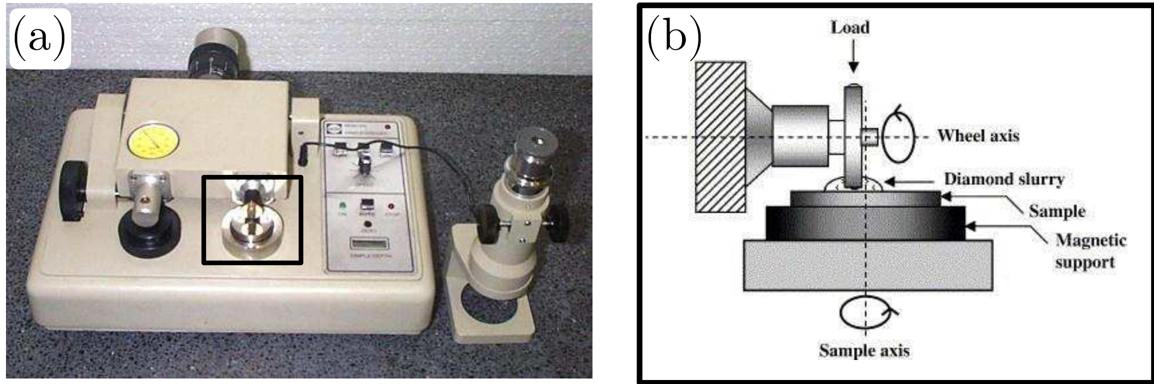

Figure 2.4: (a) Gatan 656 Dimple Grinder used to micromachine vicinal SiC. (b) The dimple grinder operates by rotating a grinding/polishing spherically-shaped wheel coated in an abrasive against the sample, while simultaneously rotating the sample. The wheel has a spherical profile so that the concave, spherical dimple is formed on the substrate. In this figure the wheel is not aligned with the sample axis of rotation which would result in an aspherical surface dimple.

grinder. Dimple grinders are used to micromachine surfaces using mechanical abrasion with a polishing compound. The sample is mounted to a stainless steel mounting chuck using Crystal Bond^{TM}509 (Aremco, Valley Cottage, NY), a strong wax which melts at temperatures above 121 °C. The chuck is inserted into the center of the table wheel which rotates at a slow, fixed speed. The sample chuck is centered with respect to the axis of rotation of the table wheel using an included alignment microscope. The SiC sample is coated with a diamond compound (Kay Diamond Products, Boca Raton, FL) diluted with water,and mechanically abraded using a vertical rotation wheel. The wheel has a spherically curved transverse profile with a diameter of 15 mm and is operable at variable speed. Figure 2.4 shows the Gatan 656 Dimple Grinder,[2] and a diagram which explains how the dimple grinder operates.[3]

The SiC dimple was ground and polished according to the principles described in the mechanical polishing section of this chapter. Dimples $20 - 45\,\mu$m deep were

[2]furnished by the Center for Nanostructure Characterization at the Georgia Institute of Technology

[3]Reprinted from Surface and Coatings Technology, Vol. 200, Gomez, M. A., Romero, J., Lousa, A., and Esteva, J., Tribological performance of chromium\chromium carbide multilayers deposited by RF magnetron sputtering, 1819 - 1824, (2005), with permission from Elsevier.

ground out using a diamond compound containing 3 μm diamond particles, with the metal grinding wheel operated at a speed of 2.5 (arbitrary units on Gatan 656 dimple grinder). The resulting dimple appears as a cloudy circular feature visible to the naked eye with a diameter of approximately 1.5 mm. A depth gauge included on the dimple grinder was used to measure the depth of the ground out dimple with an accuracy of $\pm 1\,\mu$m. To remove the damage incurred during the grinding procedure, the metallic grinding wheel is replaced by a felt polishing wheel. The polishing wheel is soaked with a slurry of diamond compound and deionized water prior to polishing. Subsequently smaller and smaller diamond particle compounds are used to reduce the roughness of the dimpled surface. Individual felt polishing wheels are used for each diamond compound to prevent cross-contamination and to maximize the smoothness of the final surface. Starting with the 3 μm diamond compound for 5 minutes at a speed of 4, followed by 1 μm and 0.25 μm diamond compounds at speeds of 4, 3, and 2 for 5, 10, and 15 minutes, respectively. It is very important that the sample position and orientation is maintained throughout the entire grinding/polishing process to prevent multiple dimples or asphericities from forming. At the beginning of the grinding phase, the position of the sample chuck is marked with a pen to guarantee that the sample has not shifted during the process.

Figure 2.5 is an AFM image of a 40 μm deep dimpled ground and polished into SiC(0001). The RMS surface roughness over a 400 um^2 area of the optically smooth, mechanically polished dimple is 1.28 nm, which is close to the initial surface roughness of the mechanically polished SiC as received from the manufacturer (0.92 nm, see Figure 2.1).

If the speed of the felt polishing wheel is not sequentially reduced during each polishing step as described in the previous paragraph, a second type of polishing damage is often evident over much larger length scales as shown in Fig. 2.6. These corrugations are easily visible in an optical microscope (Fig. 2.6a), which makes characterizing

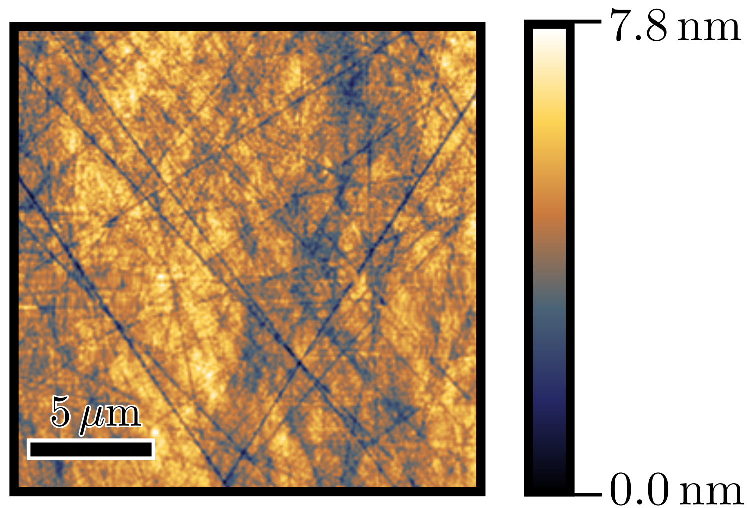

Figure 2.5: AFM image of a dimpled surface immediately after slow polishing with 0.25 um diamond compounds for 30 minutes.

the dimple after polishing a relatively expedient process. The circular corrugations or ring damage have a typical wavelength of $10 - 20\,\mu$m and amplitude of $5 - 10$ nm (Fig. 2.6b). The ring may be due to variations in the polishing compound density that can occur at higher wheel speeds. A barely visible single ring is is usually present at the center of the dimple even when the optimized procedure is performed.

Hydrogen etching the SiC surface after mechanical polishing removes the residual

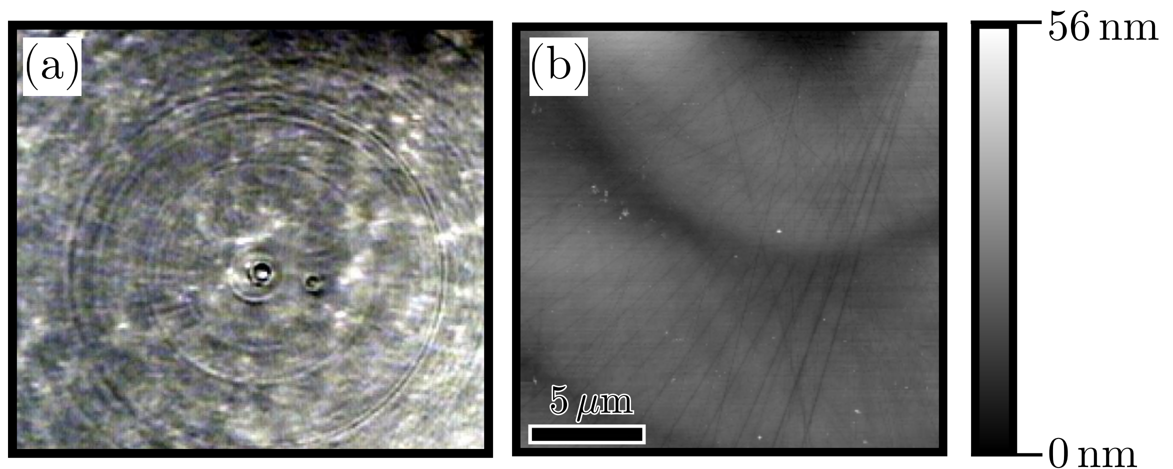

Figure 2.6: A(a) Bright-field optical microscopy image and (b) AFM scan of a SiC dimple rapidly polished with $0.25\,\mu$m diamond compound for 30 minutes. The field of view of the optical microscopy image is approximately 0.5 mm, and the image was white-balanced and contrast enhanced for better visibility.

polishing damage. Etching in the custom hydrogen furnace at 1450 °C for several hours produces a well-ordered surface with unit-cell high steps near the center of the dimple as measured with AFM (Fig. 2.7a). Figure 2.7b was acquired near the dimple rim (miscut angle 4° off-axis), where it is clear that the atomic terraces are much smaller because of the local sample miscut. For this sample the steps near the rim are well-ordered, because the sample was etched for several hours. For most samples etched for less than one hour the step near the rim of a dimple are barely discernible, most likely due to the much slower hydrogen etching rate observed for off-axis SiC surface [122, 123].

Dimpled samples hydrogen etched in the First Nano furnace using the 1800 °C recipe lead to step bunch formations across the surface that are large enough to discern using a simple optical microscope (Fig. 2.8). The step bunch height is dependent upon the miscut angle as shown in Figure 2.9. Step bunches near the center of the dimple had an average height of 6 nm, while step bunches near the rim had an average height of 30 nm (not shown). These step bunches were further characterized

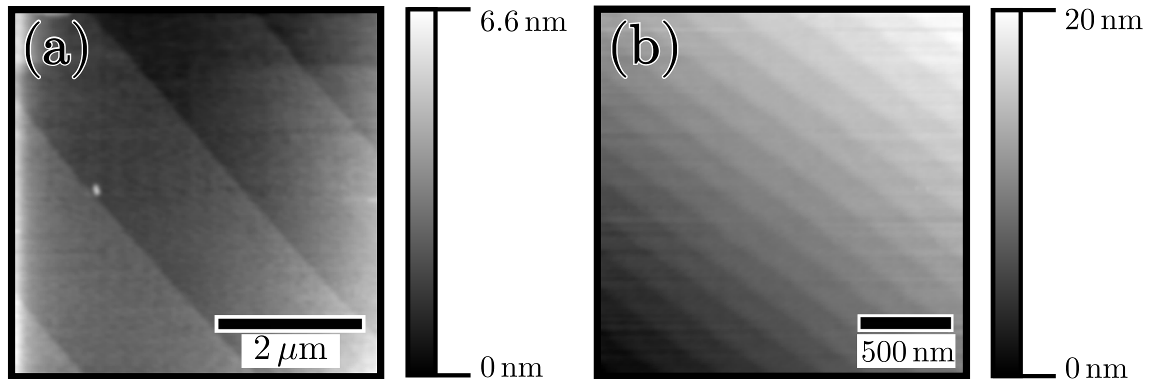

Figure 2.7: AFM images of a dimpled/vicinal 4H SiC(0001) surface after hydrogen etching in the custom furnace. (a) Near the center of the dimple the terrace widths are large because the surface is nominally on-axis, whereas (b) near the edge of the dimple the miscut angle is 4° and terrace width are much smaller.

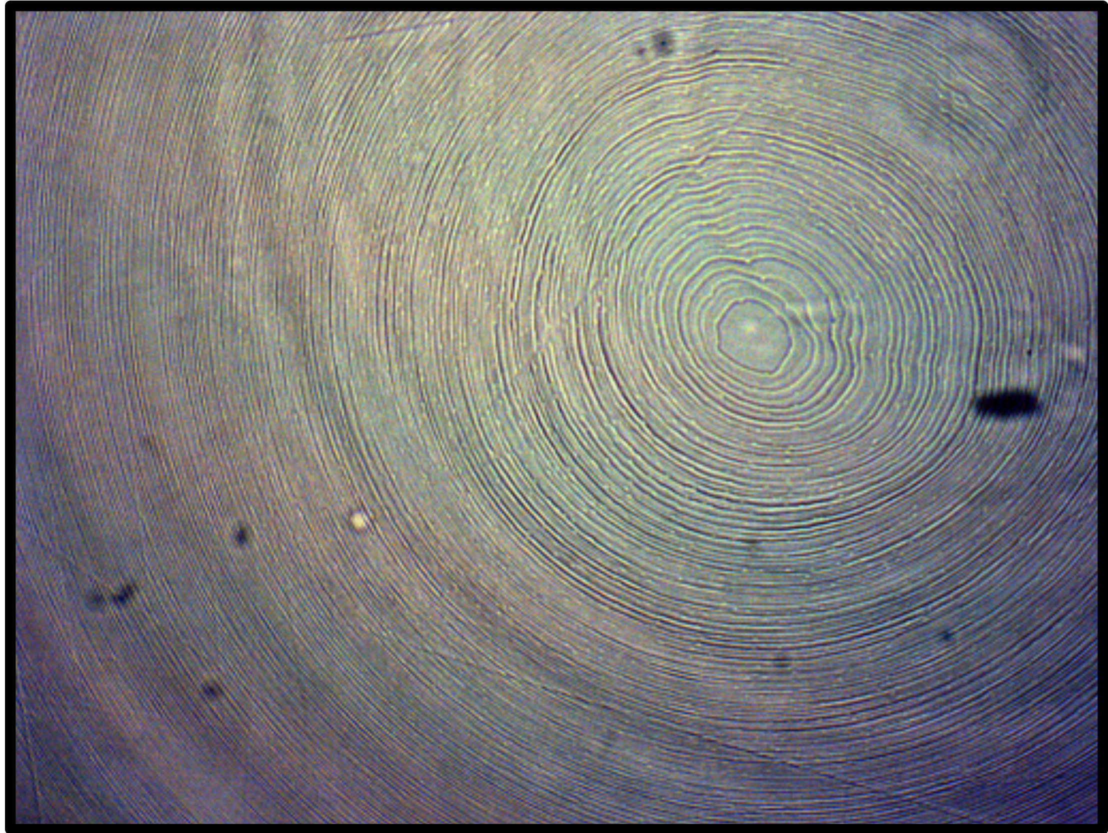

Figure 2.8: Bright-field optical microscopy (10x) of hydrogen etching induced step bunches on dimpled SiC. Photo was enhanced to improve contrast, but the step bunches are clearly visible in the unprocessed version.

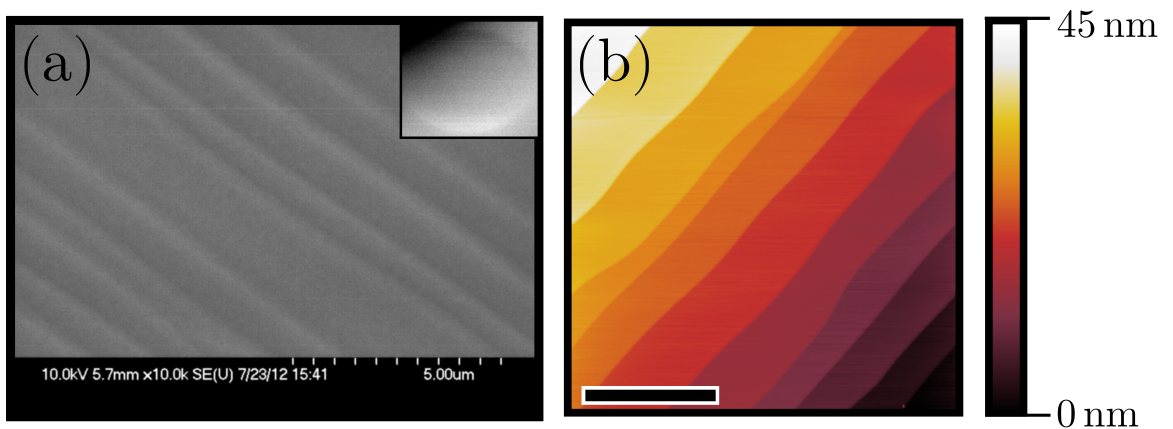

Figure 2.9: Images of step bunches formed on a dimpled/vicinal step after hydrogen etching in the FNG furnace. (a) SEM image of the complete step bunches near the lower left corner of the dimple (shown in inset). (b) AFM image of the step bunches near the center of the dimple. Scale bar is 20 μm

using a scanning electron microscope,[4] which shows that the step edges have a higher contrast than the terraces (Fig. 2.9a). SEM images throughout the rest of the dimple confirmed the formation of complete step bunches across the entire dimple.

2.2 Epitaxial Graphene Growth

Epitaxial graphene growth on SiC proceeds by thermal decomposition of the SiC substrate. This type of growth requires temperatures greater than 1200 $^\circ$C, and typically as high as 1600 $^\circ$C, to achieve high-quality graphene crystals [19]. This requirement restricts heating elements to refractory metals, high-temperature ceramics, and graphite, as these are the only materials that can survive extremely high temperatures for a prolonged period of time. Of the refractory metals, molybdenum, tungsten, and tantalum are the most common. Neither tantalum or tungsten form alloys with SiC, but tungsten islands have been observed to migrate onto SiC or graphene during growth [124]. Molybdenum is a more ideal sample holder material for high temperature processing because it is more thermally and electrically conductive [125]. However, molybdenum reacts with Si or SiC to form various molybdenum-silicides [126]. In many ways graphite is the simplest and most desirable heating element for SiC. Graphite has an extremely high melting point, has a low heat capacity which is amenable to rapid thermal processing, and is relatively inert at high-temperatures (except in the presence of oxygen or hydrogen) [117, 127]. Semiconductor-grade hardened graphite is relatively inexpensive, simple to machine, and often used for growing silicon carbide [60]. Graphite can react with elemental silicon to form SiC at high enough temperatures [128], which over time can result in damage to the heater. For this reason graphite is often coated with a protective layer to minimize surface damage and reactions which can affect SiC or epitaxial graphene growth [114, 129, 130].

Graphene was grown in two different systems. The first is a room-temperature

[4]Hitachi S-4700 FE-SEM maintained by the Georgia Tech Nanotechnology Research Center in the Marcus Building Inorganic Cleanroom

(RT) UHV (RT-UHV) chamber (base pressure 1×10^{-10} mbar) shown in Figure 2.10. For growth on EG on SiC this system is equipped with an electron beam heater, which was used to grow graphene on SiC in the earliest experiments conducted at Georgia Tech [41]. More information is available in the theses of previous students [131–134]. Briefly, the electron-beam heater is comprised of molybdenum housing with an electrically isolated tungsten filament. Disc-shaped molybdenum sample holders were used for epitaxial graphene growth. These sample holders possess a central hole to allow direct electron bombardment of the SiC samples. SiC and graphitized SiC samples were mounted onto molybdenum sample holders using thin tantalum spacers to prevent direct-contact between these materials. Heating occurs by applying a large negative voltage bias (typically less than 600 V) between the filament and the sample ground while between 4 and 5 A AC current pass through the filament. With this instrument SiC samples can be heated to temperatures as high as $1450\,^{\circ}$C in less than 1 minute.

The electron beam heater is equipped with a Type-K thermocouple probe to measure the sample holder temperature. Unfortunately, this thermocouple is mounted

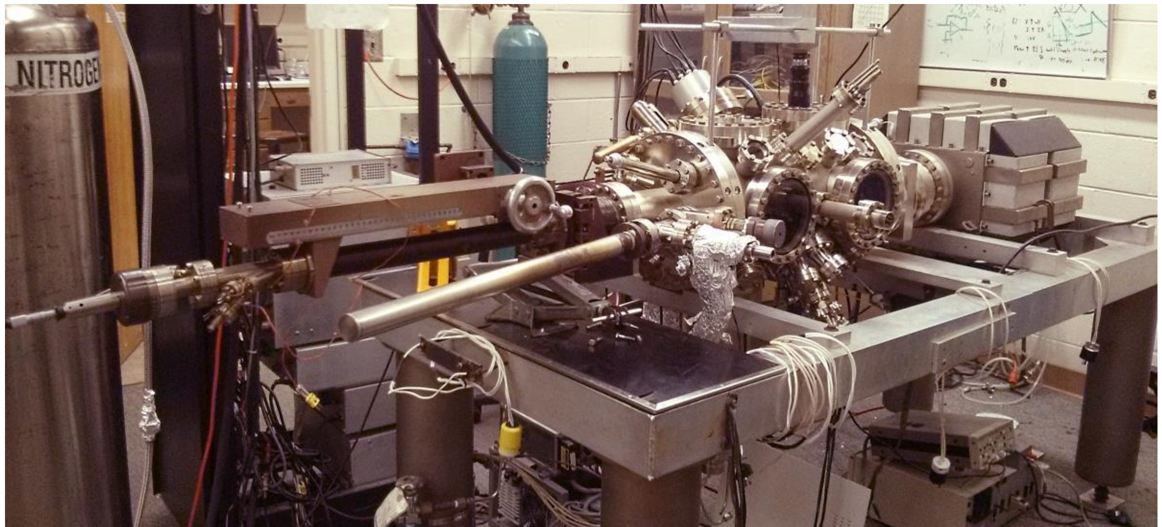

Figure 2.10: Room Temperature UHV system, equipped with an electron electron beam heater, Low-Energy Electron Diffraction, Auger Electron Spectroscopy, and Scanning Tunneling Microscopy.

on a stainless steel assembly which is incompatible with the extremely high temperatures necessary for graphene growth; therefore, two different pyrometers were used to measure the sample temperature. The pyrometers actually measure the sample holder temperature because the high-quality SiC material used in our experiments is optically transparent. In all cases the temperature of the thin tantalum sheet that partially supports the sample was taken as the sample temperature. The first pyrometer is a standard disappearing filament optical pyrometer which is manually controlled [135]. The second pyrometer is an infrared (IR) pyrometer which automatically calculates the surface temperature and has the capability for computer control and data acquisition through a serial port (previously Mikron Infrared Inc., now Lumasense, Santa Clara, CA). Temperatures measured with the IR pyrometer depend strongly on the sample hemispherical emissivity, which varies for different and materials and surface preparations. For graphitization experiments in the RT-UHV chamber the IR pyrometer optics were focused onto the tantalum strips supporting the SiC, and the emissivity in the pyrometer software was set to epsilon = 32.5% (the average tantalum emissivity over the temperature range probed in this study) [136]. With these parameters the optical and IR pyrometers agree within $\pm 20\,^\circ$C.

The second UHV system used for graphene growth experiments was equipped with an internal RF induction furnace. Figure 2.11 is a schematic of the original UHV-Furnace (UHV-F) system, where the furnace was placed directly onto the 8 inch flange of a larger UHV chamber.The furnace was comprised of an alumina tube containing a molybdenum susceptor with a closed end graphite tube (Fig. 2.11). This furnace was originally designed by Dr. David Lee Miller and more details can be found in his thesis [137]. The furnace was heated using coiled copper tubing connected to a 3 kW RF power source (Ambrell, Scottsville, NY). Cold water flows through the copper coils to prevent overheating of the coils themselves or of the high power fluid/electrical vacuum feedthrough (MDC Vacuum, Hayward, CA). The furnace was

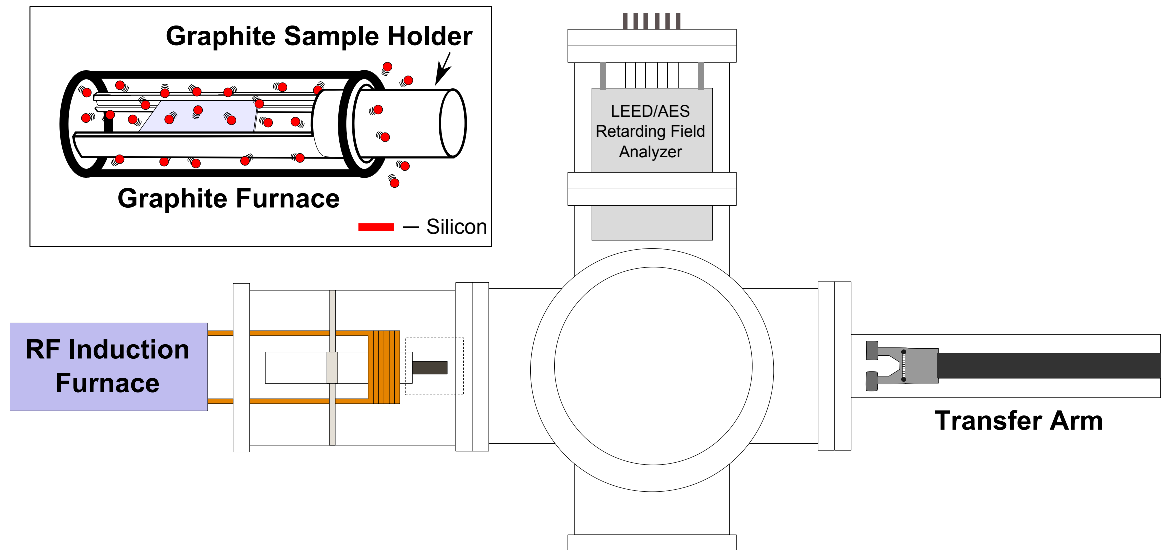

Figure 2.11: UHV chamber used for in-situ sample growth in a custom graphite furnace, and in-situ sample analysis using a retarding field analyzer for Auger electron spectroscopy (AES) and low-energy electron diffraction (LEED). SiC samples are held in a graphite holder that allows access to both sides of the wafer (inset; red balls represent gaseous silicon). The sample holder effectively seals the graphite furnace, leaving only a narrow annular channel (6.35 mm mean diameter, 15 μm width) between the sample holder and furnace wall.

assembled and mounted to the internal face of the 8 inch flange using two stainless-steel threaded rods and specially constructed stainless steel clamp. The furnace was equipped with an argon gas line to study the effect of inert gas pressure on graphene growth. An ultra-high purity argon gas cylinder was connected directly to an oxygen gas and water vapor purifier (Matheson Tri-Gas). The gas filter was connected to an ultra-high precision valve capable of leak rates as low as $1 \times 10^{-10}\,\frac{\text{Torr}\cdot\text{L}}{\text{s}}$ using stainless steel tubing, which was mounted onto the back of the furnace flange . The gas line was formed using 1/4 in stainless steel tubing joined together using Swagelock connectors and valves. The gas line was leak-checked using helium gas in conjunction with the quadrupole mass spectrometer. Although not shown in Figure 2.11, a small samply cylinder attached containing a subatmospheric pressure of pure silane gas was attached to the UHV-F system via a separate precision leak valve.

Samples were inserted into the graphite furnace using a custom graphite sample

holder, consisting of two arms with slots connected to a plug (inset of Fig. 2.11). As many as three SiC samples were placed into the sample holder slots. A slightly larger 'cap' SiC was wedged into the front end of the sample holder to prevent the samples from falling out. The SiC cap was heated in the furnace to 1600 ° C in UHV for one hour in order to cover the surface with a thick layer of graphene to limit further silicon sublimation from this element. This sample holder design allowed us to study graphitization rates on both polar terminations of SiC simultaneously. The gap between the graphite furnace and sample holder was an annulus approximately 150 μm thick and 3 mm in length, at a radius of 3.1 mm.

Growth experiments were conducted either at UHV or in static pressure of argon gas. Prior to an experiment the furnace was outgassed at 1600 ° C for 30 minutes to remove residual silicon from previous SiC anneals. Before leaking argon gas into the furnace, the gate valves to the chamber ion pump and transfer arm turbo pump were closed. The argon gas line was purged for 5 minutes and pumped down for one hour prior to backfilling the furnace in order to minimize contaminants. During this time, the samples were outgassed in the furnace for 30 minutes at 850 ° C to desorb volatile gases which might influence graphene growth. After pumping the down the gas line, the valve connecting it to the turbopump was closed and the line was filled with argon gas to approximately 1 bar. Before argon gas was leaked into the chamber, the sample temperature was less than 850 ° C as measured by the IR pyrometer. I estimate the error of our temperature measurements to be ±25 ° C. The argon gas pressure in the furnace chamber was measured with a typical Bayert-Alpert ion gauge at pressures less than 1×10^{-4} mbar. Higher pressures were measured using a Convectron gauge. After pressure stabilization was complete, the leak valve was closed. At this point, the furnace temperature was increased to 1200 ° C and maintained for 20 minutes to allow the initial SiC step-flow to stabilize across the surface [138]. Following the 1200 ° C anneal, the furnace temperature was increased

to the final growth temperature for a set amount of time. During sample growth the argon gas line was purged and pumped down to a base pressure of 2×10^{-7} mbar by turbomolecular pumping. After completing the growth phase the RF power source was turned off to cool the furnace down to $1100\,^{\circ}$C within 15 seconds and to $700\,^{\circ}$C within 2 minutes. Once the temperature of the furnace decreased to less than $700\,^{\circ}$C the UHV-F chamber was pumped down to a pressure of 1×10^{-7} mbar, at which point the ion pump gate valve was opened. Over 12 hours the system pressure would approach a minimum of 1×10^{-9} mbar. If the ion pump was heated to $125\,^{\circ}$C during this time period the pressure would reach the system base pressure of 1×10^{-10} mbar.

After graphene growth the sample holder was removed from the furnace and placed in front of the UHV-F retarding field analyzer for LEED and AES measurements (see Section 2.3.1). LEED was used to detect the presence of graphene growth and to provide an initial characterization of the graphene quality. A quantitative measurement of the average graphene thickness across the sample surface was made with AES. The AES measurements were calibrated using homogeneous epitaxial graphene buffer layer samples prepared by annealing in a custom low vacuum furnace (see Section 4.1). The graphene film thickness was used to calculate the time-integrated graphene growth rate for each sample surface in the furnace. The uncertainty in the graphene thickness measurement was estimated based upon the background noise level of the Auger spectrum for each sample. The standard deviation of the Auger spectrum was converted to an uncertainty in graphene thickness using the Auger attenuation model calculated in section 3.2 and using the standard method of uncertainty propagation.

2.3 Sample Characterization

Epitaxial graphene on silicon carbide is uniquely suited for studies using vacuum-based surface science techniques. Surface science involves the study of physical and chemical phenomena at the interfaces between different materials and/or phases. The

solid-vacuum or solid-gas interfaces/surfaces are the easiest to study because these systems are accessible to the largest array of surface science techniques. In a vacuum environment, the surface may be probed with a variety of particle scattering techniques, such as AES and LEED. Scanning probe microscopy is another powerful class of techniques which is useful for studying surfaces. SPM generally does not require a vacuum environment, although in practice sample cleanliness sometimes necessitates the use of UHV systems. Scanning Tunneling Microscopy (STM) is a very powerful form of SPM for directly probing the surface structure and electronic properties of conductive material. The first subsection will discuss particle scattering techniques and their applications in surface science, followed by the AES and LEED instruments I used in this thesis. The second subsection will present a general introduction to SPM, followed by an in-depth look at the theory and experimental design behind STM.

2.3.1 Particle Scattering Techniques

Scattering spectroscopy involves a particle probe beam which interacts with a solid surface in some way to produce a signal spectrum of scattered electrons. The particle source is typically engineered to produce a probe beam that is well-collimated, is highly focused, and has a narrow energy bandwidth. For instance, in AES the probe is a highly focused high-energy electron beam operated at a constant voltage. This primary electron beam scatters a signal spectrum of secondary electrons out of the targeted sample that are then collected by an electron analyzer [139]. Electron energy analyzers range from simple current collecting electrodes to extremely complicated precision instruments capable of simultaneously measuring electron energy, current, momentum, and spin [140]. Another surface-sensitive particle spectroscopy is X-ray Photoelectron Spectroscopy (XPS). XPS is similar to AES in that a signal spectrum of electrons is scattered from the sample and collected using an electron analyzer, but

in this case the signal is scattered from the sample by a collimated X-ray probe beam using the photoelectric effect [141]. The surface sensitivity of these techniques depends upon the type of particle in the probe and/or signal spectrum because different particles have different scattering cross-sections and mean-free paths [140]. AES and XPS have almost equivalent surface-sensitivity because they both analyze scattered electron signals with similar kinetic energies [142]. The kinetic energy determines the mean-free path of electrons in a material, which limits the effective sampling depth of the technique. A good counter-example of this behavior can be found in Energy Dispersive X-ray Spectroscopy (EDS or EDX). In this case, a high-energy electron beam causes x-ray emission from the sample, where the x-ray energy is characteristic of the elemental composition of the sample. In this case the sampling depth is determined by the energy of the high energy electron probe beam because the inelastic mean-free path (IMFP) of x-rays is very long in solid materials regardless of the x-ray energy [143].

Diffraction is another popular method for studying surfaces and interfaces. Unlike particle spectroscopy in which the probe beam excites a particle spectrum via predominantly inelastic scattering, diffraction techniques only study the elastically scattered components of the probe. Diffraction occurs when waves elastically scatter off of ordered structures, such as diffraction gratings or crystal lattices. Therefore, diffraction techniques explicitly depend on wave-particle duality. The scattered waves interfere with one another because of phase shifts that accrue as the incident waves scatter off different parts of the ordered structure. The interference or diffraction pattern which results from this process reveals the symmetry and characteristic length scales of the structure. Tuning the energy of the probe changes the wavelength of the particles in the beam, which changes the diffraction pattern in a predictable manner. Surface-sensitive particle diffraction employs massive particles with small mean-free paths such as low-energy electrons [144, 145], and helium atoms [146]. In a grazing

angle geometry it is even possible to perform surface sensitive diffraction measurements with longer mean-free path incident beams of x-rays, [147, 148] neutrons [149], or high-energy electrons (RHEED). [150] Although these technique are very useful for identifying the structure of surface and near-surface phase, in many cases multiple scatterings must be taken into account to describe these diffraction patterns quantitatively [140].

Both chambers were equipped with instruments capable of performing LEED and AES. The UHV-F system has a single retarding-field analyzer (RFA) for both LEED and AES measurements (LK Technologies, Bloomington, IN). The RT-UHV system has an RFA dedicated to LEED measurements (Princeton Research Instruments, Inc., Princeton, NJ). A diagram of the RFA design used in both systems is shown in Figure 2.12. The RFA consists of an electron gun axially centered behind 4 spherically formed tungsten grids. The electron gun emits a collimated electron beam with a narrow energy bandwidth known as the primary beam. The first and fourth tungsten grids (G1 and G4) are grounded for electrostatic shielding. The inner grids (G23) are electrically shorted to one another to insure field uniformity. Behind the grids is a spherical glass collector plate, coated with a transparent conductive film and a thin layer of phosphorescent dust. When the RFA is operated in LEED mode, grids G23 act as a high-pass filter for electrons which diffract off the sample surface. The primary beam energy is controlled directly by the user. Simultaneously, the RFA/LEED electronics automatically set the voltage on grids G23 to a value slightly lower than the primary beam voltage. This configuration favors the transmittance of diffracted electrons at the primary beam energy over the large background spectrum of electrons with lower energy due to inelastic scattering. The diffracted electrons phosphoresce upon striking the semi-transparent collector plate, which is visible from the back-side of the instrument (Fig. 2.13). Images of the diffraction pattern are saved for later analysis using a camera. One significant difference between the two LEED

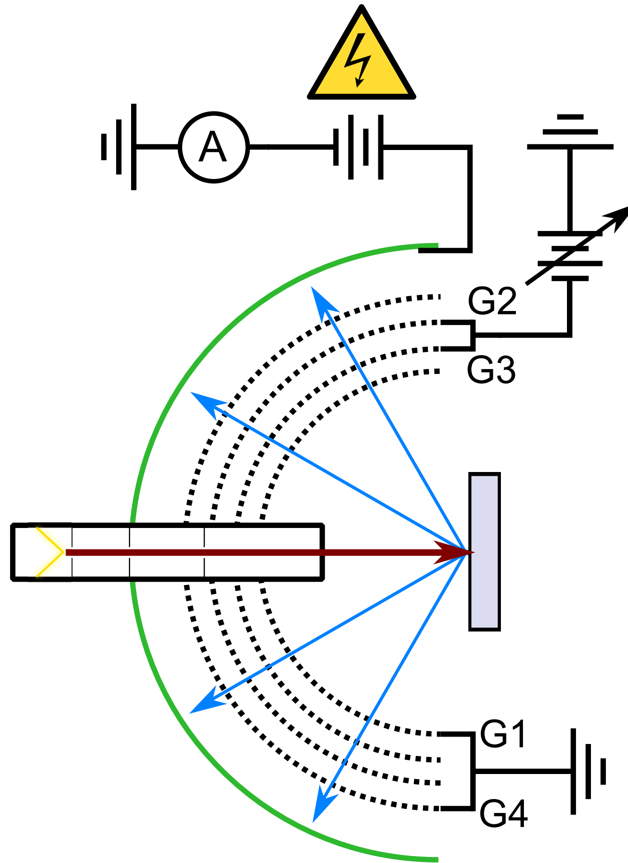

Figure 2.12: Diagram of the Retarding Field Analyzer used for both AES and LEED in the UHV-F system. The dashed lines denote the grids used for filtering electron scattered from the sample surface, where G2 and G3 are connected to variable voltage and G1 and G4 are held at ground for electrostatic shielding. The (green) solid half-circle behind the grids is the glass collector plate, which is coated with both a transparent electrode and a phosphorescent powder for diffraction imaging. The voltage on the collector ranges from as low as 200 V for AES, and as high as 5 kV for LEED (although it is typically operated between $3 - 4$ kV. The Ammeter connected to the collector for measuring Auger electron current is a simplification; in practice, the current is measured using a lock-in amplifier.

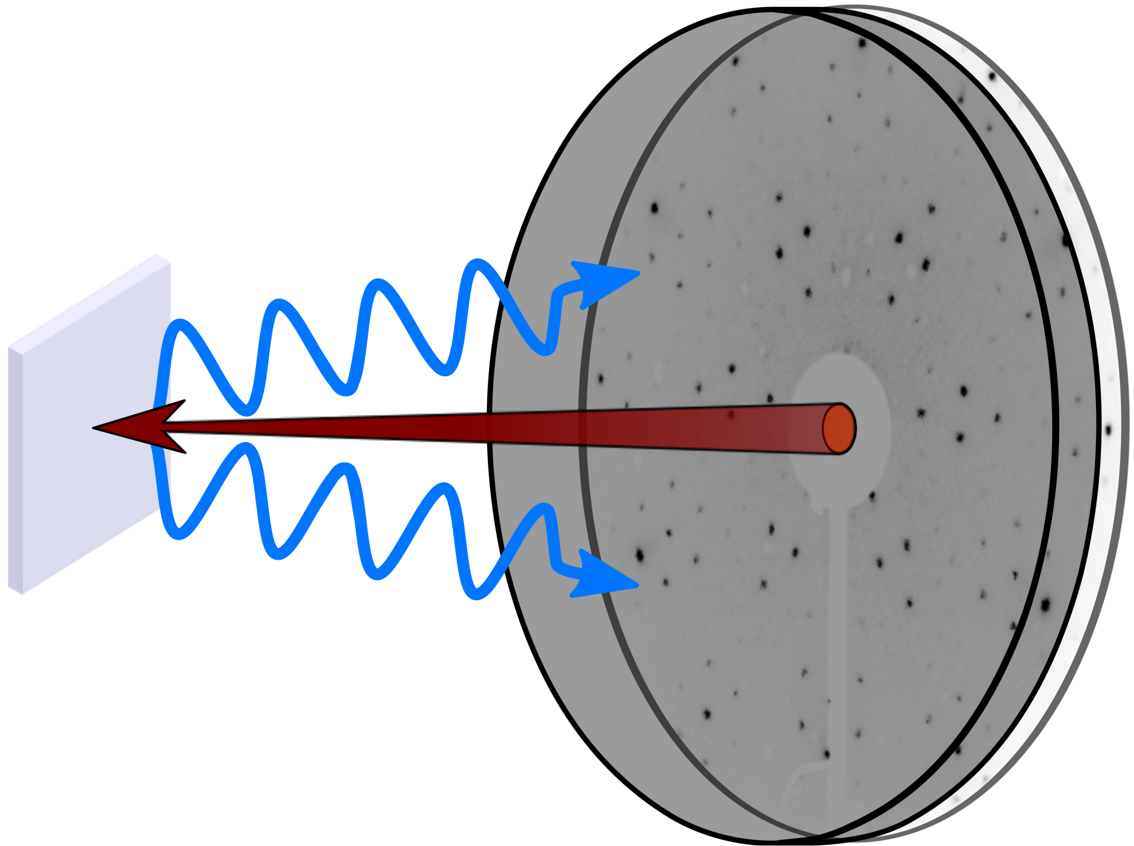

Figure 2.13: Depiction of LEED pattern acquisition using an RFA. The centered electron gun emits the low-energy primary beam, which diffract off the surface of the sample. The scattered electrons are energy-filtered by the stack of grids (depicted as a transparent gray region). A diffraction pattern forms on the phosphorescent collector because of constructive interference between electrons diffracted from a sample, in this case the $(6\sqrt{3} \times 6\sqrt{3})\mathrm{R}30^{\circ}$ surface reconstruction on SiC(0001).

systems is that the UHV-F LEED electronics are equipped with computer control for the primary beam energy. Using the open-source camera acquisition software package gPhoto2,[5] diffraction images were automatically recorded over a range of analyzer energies. This feature simplifies tracking of the individual diffraction beams as a function of energy.

Performing AES with the RFA requires a different electronic configuration than the configuration used for LEED. Once again grids G23 act as high-pass filters for

[5]gPhoto2 Digital Camera Software. Available from http://gphoto.sourceforge.net as of 03/15/2013.

the electrons scattered from the sample surface. However, in this mode the primary electron beam is operated at a constant high voltage typically between 2-5 keV and the measured electron current is due to both elastic and inelastic scattering at the sample surface. Figure 2.14 describes the Auger electron scattering process. In each of these scattering events there is a probability that the high energy primary electron (1) will transfer enough energy to an orbital electron to eject it from the bound state around the nuclei. When a low-energy core-shell electron is ejected in this manner (2), electrons from the high-energy valence shell will relax down to fill the vacancy (3). The electron relaxation obeys energy conservation by either (a) emitting an x-ray photon with an energy equal to the difference between the core-shell and valence shell levels, or (b) ejecting an electron with the same energy (4). Therefore, the energy of these electrons, known as Auger electrons after their discoverer [151], is characteristic of the element involved in the scattering process since the energy of Auger electron is determined by the orbital electron energy levels of the element [140].

The probability of an Auger electron scattering event is much lower compared to other secondary electron scattering events. Distinguishing these small peaks amidst this large background is essentially impossible without the use of signal amplification which is typically achieved using a lock-in amplifier [152]. Lock-in amplification works by summing a small AC voltage modulation with a very narrow frequency bandwidth into the signal line. Amplification occurs by sampling the signal components with the correct reference frequency, and rejecting all other frequency components as noise. The AC modulated signal is then sampled and the slope of the signal directly calculated. Signal detection is improved using this type of amplification because changes in the signal slope are much more dramatic compared to changes in the overall signal intensity when comparing a small signal versus an intense background level.

The large secondary electron background is a factor in every variant of high-energy electron spectroscopy or microscopy, but this problem is particularly troublesome in

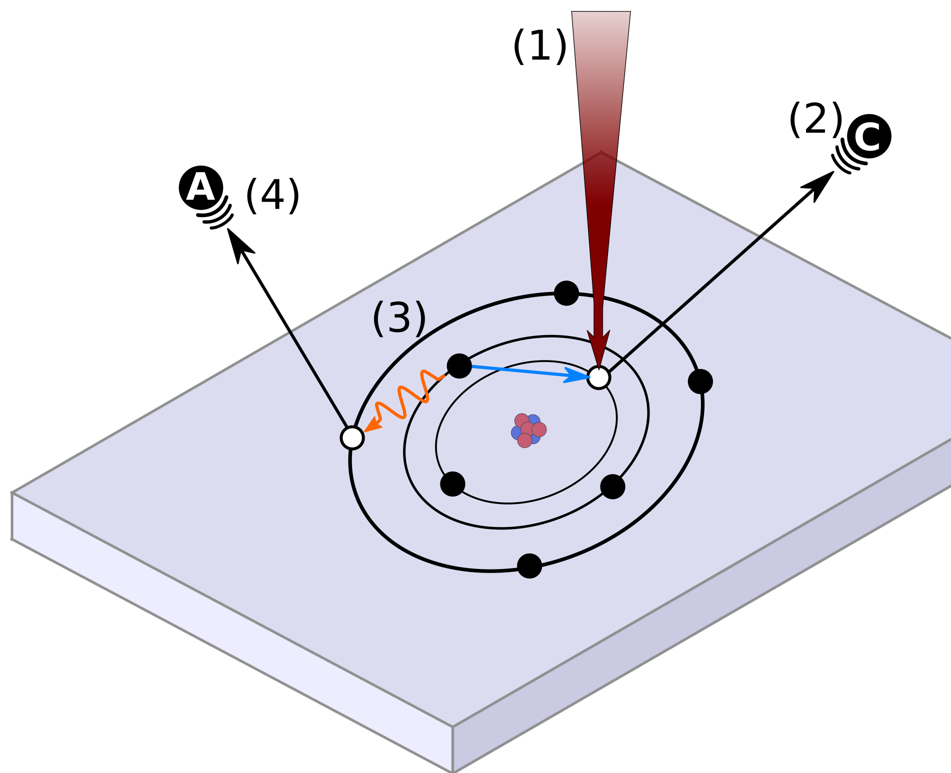

Figure 2.14: Auger electrons are scattered from materials when they are exposed to high energy electron or x-ray beams (1), which can eject electrons from core-shell orbitals in the near-surface region of the sample. The electron cloud relaxes by filling the core-shell vacancy with an electron from a higher energy level, releasing energy which can excite and eject an Auger electron (3).

the RFA geometry because of the very wide acceptance angle for scattered electrons and the fact that the instrument only high-pass filters the scattered electrons. The RFA geometry for AES has largely been replaced by more modern designs such as the cylindrical mirror analyzer (CMA) [153] installed in the RT-UHV system (single-pass CMA, PHI model 10-155, Physical Electronics, Chanhassen, MN). The CMA improves upon the poor signal-to-noise and low energy resolution of the RFA by employing concentric cylinders with small apertures to filter scattered electrons from sample surface before collection at the detector. The voltage bias between the two cylinders guides the electrons from the entrance aperture to the exit aperture, geometrically forming a band-pass filter. The energy resolution in this geometry is determined primarily by the mean acceptance angle of the CMA and width of the

exit aperture at the cost of sacrificing total transmission of electrons. The total transmission $T \approx 7\%$, so the electron currents achieved with this method require the use of an electron multiplier, unlike the RFA which has a very large transmission factor and simply collects and measures the current directly. The electron multiplier in the CMA is a single-channel electron multiplier of the continuous dynode variety.

2.3.2 Scanning Tunneling Microscopy

Scanning probe microscopy describes any kind of imaging technique which employs a mobile probe to measure the properties of a material. In most cases SPM is extremely surface-sensitive, in that the measurement typically can only probe the accessible surface of a material. Some SPM techniques are capable of probing subsurface properties with nanoscale lateral resolution, such as near-field scanning microwave spectroscopy [154]. SPM is loosely separated into contact and non-contact based techniques, although there is often some ambiguity as to what actually defines contact because different SPM techniques rely on distinct physical interactions to measure surface features. The type interaction and SPM probe (or tip) size typically defines the theoretical sensitivity and resolution of the technique, although these methods are often further limited by the practical considerations such as vibrations, signal noise, electronic speed and bandwidth, etc. This section will briefly describe the history of SPM and the major differences between two of the more popular types of SPM, scanning tunneling microscopy (STM) and atomic force microscopy (AFM).

Although not recognized as a form of SPM (and certainly less sensitive than most techniques), humans often use their fingers and the sense of touch to gain insight into the roughness, texture, and/or shape of the objects we encounter. This technique is critical for people who are blind or visually impaired, especially for communication using braille (a tactile reading/writing system). SPM is clearly superior

to tactile feedback in terms of sensitivity and repeatability. Mechanical profilometers are contact-based instruments where a small diamond stylus is scanned across a surface while measuring and recording surface height variations. Despite the simplicity of this technique modern mechanical profilometers are capable of detecting surface height variations as small as approximately 0.5 nm. The lateral sensitivity of mechanical profilometers is limited by the physical size of the stylus, although this problem has been mitigated with the introduction of nanometer scale styluses and with advanced analysis software which can deconvolve the tip shape with the actual shape of the surface feature.[ref] Nevertheless, contact SPM is essentially incapable of achieving atomic-scale imaging because the physical interaction (coulomb repulsion for contact) which defines the measurement is unspecific and insensitive. In addition, contact-based measurements can easily disturb the delicate and environmentally sensitive atomic-scale features on most surfaces.

Non-contact SPM techniques overcome these difficulties by utilizing relatively long-range forces and interactions between the tip and the surface. In principle the simplest realization of this concept would involve measuring the capacitance between a metallic sample and tip. If we were to assume that the tip apex has a known geometric shape, in principle it is elementary to calculate either analytically or computationally the tip-sample capacitance for any tip-sample separation. Unfortunately, the tip-sample capacitance is a slowly varying function with respect to the tip-sample separation. However, many interactions mediated by the electromagnetic force are much more sensitive to the tip-sample separation. These interactions are monitored and used (with the aid of an electronic feedback system) to maintain a constant tip-sample separation as the surface is scanned. Besides maintaining pristine sample surfaces the main benefit of non-contact SPM is that the forces involved are typically very sensitive to the tip-sample separation. The scanning tunneling microscope (STM) invented by Binnig and Rohrer at the IBM Zurich Research lab in 1981 was the

first example of the non-contact SPM, and was the first instrument to achieve direct imaging of atomic-scale features on a surface [155–157]. STM utilizes the tunneling current between a metallic tip and a conductive sample to measure and maintain the tip-sample separation as the surface is rapidly scanned. As discussed in more detail in the next section, the tunneling current between two electrodes depends exponentially upon the electrode separation or tunneling gap [158]. The STM was rapidly recognized as an incredibly powerful and important invention, and in 1986 the Nobel Prize was awarded to Binnig and Rohrer for their work only 5 years earlier [159]. The Zurich STM design was quickly replicated and improved upon by other laboratories throughout the world [160].

The second SPM was the atomic force microscope (AFM) invented by Binnig, Quate, and Gerber at IBM Zurich in 1986 [161]. In principle the AFM can be used to measure any kind of force between the tip and a sample [162], although in practice topography measurements are accomplished with AFM in the non-contact mode by measuring the relatively long-range Van der Waals force (and any other forces) between the tip and surface to maintain a constant tip-sample separation [163]. The AFM has been more commercially successful than the STM because it is a fundamentally more versatile technique [160]. The most desirable feature of AFM is that it can be performed on any kind of a material in essentially any environment [164], unlike STM which only works for conductive surfaces/tips and generally requires either vacuum or an inert atmosphere in order to function with atomic-scale resolution [140]. AFM can perform a variety of different modes in parallel with traditional non-contact topographical scanning. For instance, scanning capacitance microscopy has been realized as a complementary technique in AFM instruments. The AFM maintains the constant tip-sample separation concurrent with measurements of the tip-sample capacitance as the tip is scanned across the sample [165]. It is also possible to measure the near-field optical response of a surface by probing it with near-field

scanning optical microscope (NSOM). An NSOM tip is made from a pulled optical fiber coating with metal everywhere but the tip apex. As the tip is scanned across the surface in the AFM mode any near-field optical signals will couple to the metallic tip aperture before propagating down the optical fiber and into a photodetector [166]. Although the AFM has been more popular, the STM is still the gold standard for acquiring local measurements of a surface with atomic-scale resolution. In the following sections I will describe the theory and experimental implementation of STM, and in will close with a brief explanation of AFM in order to compare and contrast these often complementary techniques.

2.3.2.1 Quantum Mechanical Tunneling: Background and Theory

Tunneling refers to the ability of particles to pass through potential energy barriers that would be otherwise impossible according to classical mechanics. Quantum tunneling was originally invoked to model alpha decay and nuclear decay rates [167], but is now understood that tunneling is a general feature of quantum mechanics. This correctly implies that quantum tunneling is only observable in systems where the wave-like nature of a particle is relevant. In other words, tunneling is only observed when the wavelength of the particle is greater than or equal to characteristic length scales of the systems potential energy landscape. When the objects wavelength is very short compared to the barrier width it will interact with the barrier as a classical particle would, which is why macroscopically large particles are incapable of tunneling. However, recent experiments involving large atomic ensembles such as C_{60} fullerenes [168] and mesoscopic mechanical oscillators [169] have shown that even relatively large objects can exhibit some quantum mechanical properties.

Elementary particles routinely undergo quantum mechanical tunneling, such as in the nuclear decay of radioactive elements or isotopes. For instance, in alpha decay a He^{2+} ion is emitted by tunneling out of the potential energy well from the strong

nuclear force [167], and in beta decay the electron emitted from the nucleus tunnels through the potential energy barrier of the surrounding electron cloud [170, 171]. Quantum tunneling can assist chemical reactions through the structural or conformational rearrangement of molecules despite the presence of significant energy barriers in the reaction pathway. For example, ammonia molecule inversion occurs rapidly at room temperature because the nitrogen atom is capable of tunneling between the symmetric and anti-symmetric states in the molecule [172]. Electron tunneling is extremely important for understanding the ground state electronic configurations of sp^2 hybridized carbon networks in organic molecules such as benzene [173], and organic solids such as graphene and graphite (see 1) [20, 22, 23, 35].

Tunneling is responsible for a variety of electron dynamics in solid-state systems. Cold or field emission of electrons from metals or semiconductors occurs because of quantum mechanical tunneling [174]. Another common example of quantum mechanical tunneling is found in the aptly named tunnel junction. A tunnel junction consists of two conductive materials separated by a thin insulating layer. Research into tunnel junctions was ignited in the late 1950s by the discovery of interband tunneling between degenerately doped regions of opposite polarity in silicon. [175] The tunneling barrier in these Esaki silicon diodes is a thin insulating layer of silicon layer at the interface of the pn-junction [176]. The simplest tunnel junction consists of two planar metals separated by an insulating layer. The theory of electron tunneling through an insulating barrier between similar or dissimilar electrodes was first explained by Simmons [177, 178]. The first of these devices were manufactured by depositing aluminum onto a substrate, forming a thin-film thermal oxide of alumina, and then depositing a second aluminum onto the insulator. The Al-Al_2O_3-Al tunnel junction was studied experimentally and theoretically by Hartman and Chivian [179, 180], who determined that the current for sufficiently thin insulating layers (less than 30 Å) was entirely attributable to quantum-mechanical tunneling [179].

$$T \approx e^{-2\frac{z}{\hbar}\sqrt{2m_e(V_0-E)}} = e^{-2\kappa z} \tag{2.1}$$

For trapezoidal tunneling barriers this problem is solvable using the Wentzel-Kramers-Brillouin (WKB) approximation [179, 180]. However, it is more instructive to consider a conceptually simpler but similar problem. If the tunnel junction electrodes are large enough, such that quantum size-effects may be neglected, and the problem is restricted to rectangular barriers, then the tunnel junction problem simplifies to the standard graduate level thought experiment used to demonstrate quantum mechanical tunneling. In this case the problem involves a plane-wave electron with mass m_e and momentum $\hbar k_F = \sqrt{2m_eE}$ (where E is the Fermi energy of the anode electron gas) incident upon the electrostatic potential barrier of height V_0. Classically the particle can only surpass this barrier if the particles energy E is greater than the height of the barrier ($E > V_0$). The quantum mechanical version of this problem is treated using the 1D version of Schrödingers equation. In the quantum regime the electron wave function decays exponentially in the barrier region. Since the wave-function is continuous, there exists a finite probability that the electron will penetrate through the barrier and continue traveling in the form a transmitted plane wave. The probability of transmission T (or the tunneling current) is given in Equation 2.1.

The tunneling current depends on the barrier width z and the tunneling decay constant κ which is a simple function of the reduced barrier height $(V_0 - E)$. In practice, V_0 is the combination of the applied voltage bias and the work function difference between the two electrode. The decay constant is approximately $1\,\mathring{A}$ for most materials separated by vacuum. Therefore the vacuum barrier width must be considerably less than 1 nm to measure reasonable tunneling currents. Furthermore the current will change by an order of magnitude for every angstrom of change in the barrier width, enabling incredibly sensitive surface height measurements. Tunneling will occur if filled electron states in the left electrode overlaps with empty states in the

right electrode, or vice versa. For this reason it is possible to tunnel electrons between two metal electrodes at any finite voltage bias, assuming the voltage is low enough to suppress field emission [174]. If at least one of the electrodes is a semiconductor then tunneling is forbidden if the Fermi energy in one electrode is aligned with an energy gap in the other electrode

$$I = \pm \frac{2\pi e}{\hbar} \int_{E_F}^{E_F+V_B} \rho_{tip}(\epsilon) T(\epsilon) \rho_{sample}(\epsilon) d\epsilon \tag{2.2}$$

A better treatment of the tunnel junction problem should account for more realistic conditions. The actual shape of the potential energy barrier is modified from the ideal trapezoidal shape due to surface potential effects [181]. Therefore a more exact solution to the tunneling barrier problem requires a more advanced treatment, such as that given by Tersoff and Haman [182]. Equation 2.2is a more accurate calculation of the tip-sample tunneling current using first-order perturbation theory, where ρ_{tip} and ρ_{sample} are the density of states in the tip and sample, respectively, V_b is the applied voltage bias, and E_F is the Fermi energy. $T(E)$encapsulates the tunneling matrix which describes all possible scattering probabilities between electron wave functions in the tip and the sample [183].

In STM, one electrode is a sharpened metal tip with an (ideally) flat density of states like tungsten or Pt-Ir and the other electrode is the sample of interest. Therefore, the tunneling current is proportional to the integral of the sample local density of states (LDOS) beneath the tip. The limits of this integral are E_F and $E_F + eV$ because all of the electron states in this range are conceivably available for tunneling. The tunneling current is very sensitive to the wave functions in the microtip and the sample, as expressed by the tunneling matrix M. In most cases the current and constant charge LDOS images acquired with STM are well described by simple s-wave tip models [184]. When s-wave models are valid, the topographical features acquired

by STM reveal the contours of constant LDOS across the sample surface [182]. In addition, the derivative of the tunneling current with respect to the applied bias voltage is directly proportional to the sample LDOS at the energy $E_F + eV$ [185]. For this reason differential conductance measurements across the sample surface are used to determine the spatial dependence of the sample LDOS. Higher angular momentum tip wave functions can be important for imaging extremely small atomic-scale features on graphite and other materials with very small lattice constants [185]. Recently a CO functionalized STM tip with p-wave character was used to directly image the small scale nodal structure of the highest occupied molecular orbital and lowest occupied molecular orbital in pentacene and napthalocyanine that is inaccessible to s-wave tips [186].

2.3.2.2 Experimental STM Design

STM instruments form a mobile tunnel junction by suspending a movable, atomically sharp metal tip (electrode I) over a conductive substrate (electrode II) as shown in Figure 2.15. In most cases the insulating layer is either vacuum or an inert gas [181, 187], although sometimes a liquid-phase surface is studied [188–190]. When studying atomic-scale features on metal or semiconductors it is common to perform STM in ultra-high vacuum (UHV) because these surfaces are typically not chemically inert. A clean metallic surface will be coated with approximately 1 ML of contaminants in as little as 3 hours in a UHV chamber at a pressure of 1×10^{-10} mbar. Clean sample surfaces are prepared in UHV by thermal annealing, ion sputtering, or a combination thereof [181]. Tungsten tips are the most common material used for STM because it is a hard and relatively abundant refractory metal that is simple to sharpen using electrochemical etching [191]. Tungsten tips must be cleaned in vacuum via thermal annealing or sputtering in order to remove the oxide which forms during the etching process and exposure to air. Other common tip material includes Ir and Pt-Ir, both

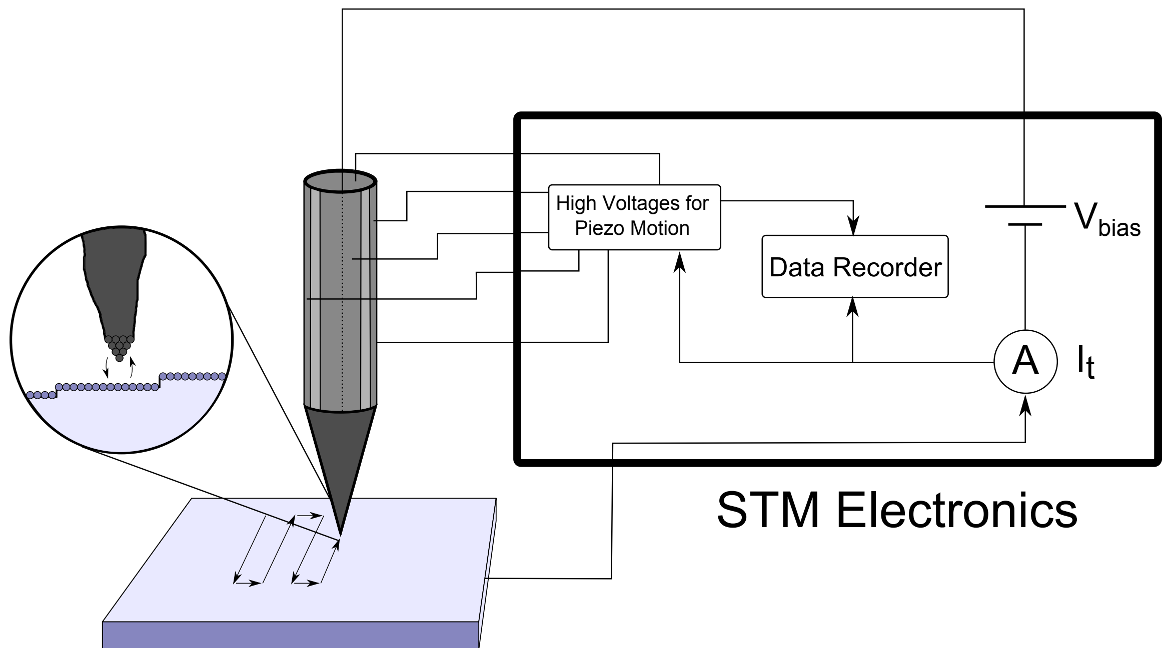

Figure 2.15: Schematic describing the operation of a typical STM. In this setup the sample is stationary while the tip is connected to a single tube piezo, which can be scanned in the X,Y, and Z direction depending upon the voltages output from the STM electronics. A voltage bias V_{bias} is applied between the STM tip and the sample and the tunneling current I_t is monitored by the STM electronics. A feedback loop in the STM electronics maintains a constant I_t by adjusting the tip-sample separation using the the high voltage output of the STM electronics connected to the piezoelectric scanner. The inset shows the atomically sharp STM tip positioned several Angstroms from the sample surface during operation. The arrows demonstrate that electrons can tunnel between the STM tip and sample in either direction depending upon the voltage bias.

of which are hard nearly-free electron metals that are inert in air [192]. Surface science UHV chambers sometimes include a suite of tools for tip characterization and preparation. For instance, Field-Ion Microscopy is can be performed on STM tips prior to tunneling experiments in order to image the atomic structure at the tip apex [181].

Piezoelectric ceramics are the only electromechanical actuator with enough sensitivity for SPM, where they are used to carefully move the tip closer to sample to achieve measurable tunneling currents, and to scan the tip across the surface once tunneling is achieved [158]. Piezoelectric materials lack inversion symmetry in their crystalline structure and thus possess coupled elastic strain and electric fields. The strain-induced from electric fields translates into physical motion of the piezoelectric material [193]. Piezoelectric ceramics are manufactured in a variety of different shapes and sizes. One common piezoelectric form used in SPM are cylindrical tubes as shown in Figure2.15 [194]. Metal electrodes are deposited on the ceramic surface in order to apply electric fields across the material and generate motion, but first the piezoelectric material must be polarized by applying a very large electric field across the electrodes to induce spontaneous ferroelectric polarization. Piezoelectric materials expand/contract when the electric field is parallel/anti-parallel to the previously induced polarization vector [195]. Piezoelectric tubes are often used for SPM scanning because they can achieve much larger static displacements in all directions without the need to stack multiple actuators [196]. Piezoelectric tubes for STM are manufactured with four distinct electrode quadrants on the outer surface and a single electrode on the inner surface. If the piezoelectric tube is polarized radially then the outer electrodes can be used to generate X and Y displacements by bending the tube, while the inner electrode is used to generate Z displacements by increasing or decreasing the entire tube wall thickness [196]. A tip-sample separation or gap of less than 1 nm is necessary to achieve measurable tunnel currents, on the order of 10 to

1000 pA when working in a vacuum. Since the STM tip is usually atomically sharp any mechanical interaction with the tip apex can irreparably damage the tip. Before measurable tunneling is achieved the tip-sample separation is carefully reduced using a coarse approach method [194, 197–202]. Various STM designs have different coarse approach mechanisms, most of which employ piezoelectric elements to slowly walk the tip towards the sample. The proximity of the STM tip and sample surface necessitates the use of vibrational isolation to prevent inadvertent tip-sample collisions and to lower the noise level of the tunneling current. The original STM design employed liquid helium cooled magnets to levitate the STM free of any vibrational noise sources [158]. Today it is understood that properly designed spring systems are sufficient to dampen most vibrational noise [159], although in some cases more extreme approaches have been taken to insure total stability over very long time scales [203]. Once the STM is within tunneling range the tip-sample separation is controlled via an electronic feedback loop ('electronics box' in Figure 2.15). The feedback loop attempts to maintain a constant tip-sample tunneling current by modulating the voltage which controls the Z displacement of the piezoelectric with the mounted tip or sample.

The RT STM used in this thesis is suspended from two separate spring stages inside the RT-UHV chamber described in Section 2.2. The RT-UHV chamber itself rests on 4 massive table legs as a first step in vibrational isolation. The first STM spring stage employs magnetic damping to further lower the instrument vibrational noise level, and the two spring stages have different resonant frequencies to prevent interstage coupling. Figure 2.16 is a photo of the RT STM, which is fashioned from two concentrically-mounted piezoelectric tubes[6]. The outer tube (0.5 in OD, 0.025 in wall thickness, 0.5 in in length) was used entirely for actuating the tip height (tip-sample separation, z-axis in Figure 2.15). The inner tube (0.25 in OD, 0.025 in wall thickness,

[6]PZT-5A (EBL #2), purchased from EBL Products Inc.

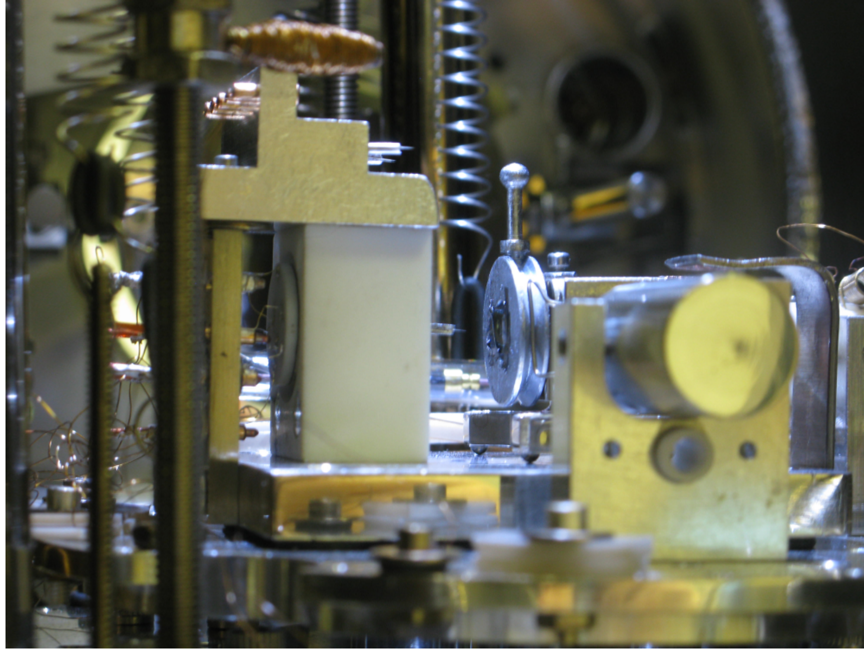

Figure 2.16: RT STM supported from two sets of spring stages (visible in the background) in an UHV system. The white Macor block in the center of image supports two concentric tube piezoelectric elements for actuating the STM tip across the sample surface. Thin gold wires leading to the STM tip or the tube piezoelectric electrodes can be see on the back of Macor. A dimpled SiC sample is visible on the platter-shaped sample holder in front of the STM tip.

0.5 in in length) was used scan the tip across the sample surface (xy-axis in Figure 2.15). The inner tube has a front-facing Macor cap with a gold-coated beryllium-copper socket used to hold the STM tip during operation. The tip is constructed from a 1 mm diameter tungsten rod, with a smaller diameter wire spot-welded near one end. The tip is manually inserted into the tip socket using a wobblestick-type manipulator. The actual microscope used in this thesis was rebuilt by the author after a tip was irremovably lodged in the original, which was previously described in another thesis [204].

Sample holders are inserted onto a sliding sample positioner using the wobblestick. Coarse approach of the sample to the tip is achieved using a separate inchworm piezoelectric actuator [197, 198]. During a coarse approach, the inchworm gently pushes the sample positioner closer to the stationary microscope. In general, the tip

is manually approached until the physical tip is almost in contact with the reflection of the tip in the sample surface. At this point, the tip sample separation is less than 100 μm and a slower computer controlled approach is activated to bring the STM tip within tunneling range of the surface. The tunneling current is first converted into a voltage using a vacuum internal current-to-voltage amplifier with a static gain of 10^8 V/A and then further amplified using a SRS 560 low-noise voltage pre-amplifier (variable gain but typically operated at 100 V/A).

The STM is controlled using a custom electronics box containing a floating-point, digital signal processor (DSP, ADSP-21369 SHARC, Analog Devices, Inc., Norwood, MA) as single-variable feedback loop controller. The electronics box contains analog-to-digital and digital-to-analog converters to enable communication between the STM and the DSP, and various other components for signal filtering and monitoring. The DSP utilizes a PID controller algorithm which differences the measured tunneling current with respect to a current set point. The resulting error voltage is used to calculate a response in the output voltage for the z-axis piezoelectric tube, thus coupling the tip-sample separation and the tunneling current with the DSP controller. The z-axis signal is first passed through a high-voltage summing amplifier in order to achieve the correct change in the tip-sample separation as controlled by the PID loop. An attached computer server is used to generate XY scanning voltages (using a National Instruments digital output board), and to acquire image spectroscopic data from the DSP controller using asynchronous serial communication. A separate client computer was used to control the server computer, where the client was used for high-level operations using a GUI to prepare and initialize experimental scans and for visualizing data acquired on the server computer. The Python Open Source Scanning Microscopy (POSSM) software package was used to control the STM electronics during scan acquisition. More details concerning the DSP electronic servo and the POSSM software used for the RT STM is available in a previous thesis [137].

CHAPTER III

EPITAXIAL GRAPHENE GROWTH ON SILICON CARBIDE

Although it is has been studied for almost 40 years, the growth of epitaxial graphene (EG) on silicon carbide (SiC) is still poorly understood. Thin-film growth by decomposition of the substrate is unlike traditional thin-film growth techniques such as simple molecular beam epitaxy (MBE), sputter/evaporative deposition, or chemical vapor deposition (CVD). In all traditional thin-film growth methods, a target material is deposited at a known rate onto a heated substrate (higher temperatures facilitate surface diffusion and better thin films). Epitaxial graphene growth is driven by high-temperature thermal decomposition of the SiC substrate which results in silicon vapor sublimation and surface carbon enrichment. In this chapter, I show that there is a correspondence between all of these thin film growth techniques and that the vast array of techniques used to study traditional thin-film growth are applicable to EG on SiC. I also demonstrate that high quality EG on SiC is only achievable when the solid SiC and silicon vapor phases are close to thermodynamic equilibrium, such that the EG growth rate is low and the SiC surface is not degraded by the sublimation/graphitization process. Finally, I present a universal model for growing EG on SiC, which can be used to understand and predict the growth rates in different experimental conditions.

3.1 Motivation for Kinetic Theory of Graphene Growth

Early studies of epitaxial graphene growth were conducted in ultra-high vacuum (UHV) with the sample situated in an open geometry [8, 205–210], which is shown

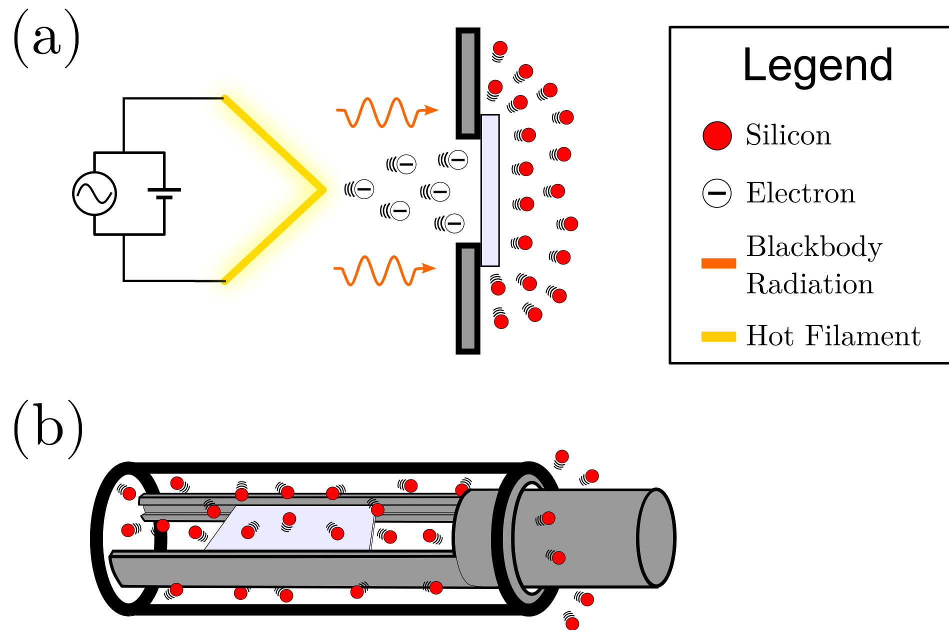

Figure 3.1: This figure describes the two different geometries used for EG growth on SiC. (a) The open geometry has the sample surface freely exposed to a large volume, such that the surface is accessible to material deposition and experimental characterization, but allows for the silicon to sublimate freely from the SiC surface during annealing. (b) In the confined geometry the silicon is heated in a small, enclosed furnace so that silicon vapor has many collisions with the sample before escaping.

schematically in Figure 3.1a.The open geometry configuration is also used for most thin-film growth experiments in UHV because the sample surface is accessible for material deposition and for analysis using surface sensitive measurements, some of which can be operated during the growth itself. For instance, in MBE an evaporated beam of the material is deposited directly onto the sample substrate at temperature, T, typically with a flux, F, that is often much less than one monolayer (ML) per sec. Elevated temperatures are often necessary to increase the adatom surface diffusion length, which is important for achieving high-quality layer-by-layer growth in MBE.

Epitaxial graphene growth is driven by high-temperature thermal decomposition of the SiC substrate. Because the vapor pressure of carbon-containing products is 10-100 times smaller than pure silicon at the experimental temperatures of interest,

the rate of surface carbon enrichment is almost identical to the rate of silicon sublimation. Vaporized silicon travels without interatomic collisions until it strikes and condenses onto another surface in the UHV chamber. Therefore, in the UHV, open geometry configuration there is almost zero probability for vaporized silicon to return and interact with the hot SiC surface. Without a vapor pressure of silicon surrounding the hot SiC, SiC thermal decomposition occurs out of chemical equilibrium. In addition, sublimation (and EG growth) occurs very rapidly when the solid/gas phases of a material are out of chemical equilibrium. The thermodynamic and kinetic conditions of UHV, open geometry approach to thin-film growth is incompatible with the production of high-quality EG on either face of SiC, as clearly shown in previous work on this subject [109, 111].

Clearly a basic challenge for the growth of high-quality graphene on hexagonal SiC substrates is to achieve independent control of the carbon surface diffusion rate and the effective carbon deposition rate (i.e., the silicon sublimation rate). As for MBE, these parameters are expected to regulate the surface and film morphology, but for simple vacuum sublimation, both rates are determined by a single parameter: the substrate temperature. Hence, controlling the silicon sublimation flux is crucial for controlling the rate of graphene growth at a chosen substrate temperature. Prominent methods to achieve this control are 1) confinement of the SiC wafer within a nominally sealed furnace (confinement controlled sublimation, CCS), 2) use of an inert gas to impede the sublimation flux, 3) introduction of silicon flux to the surface via a low pressure of disilane, and 4) co-decomposition of face-to-face SiC wafers. In each case the net flux of silicon from the substrate is reduced. This reduction allows growth at higher temperatures, which favors layer-by-layer graphene formation and large atomically flat terraces. Methods 1 and 2 focus on reducing the silicon flux from the SiC substrate itself, but methods 3 and 4 provide an extra source of silicon. Although the growth temperatures span a wide range relative to typical UHV growth, all of

these methods achieve significant improvement in the quality of epitaxial graphene.

These methods force the vapor-phase closer to thermodynamic equilibrium with the solid-phase by restricting or compensating for physical vapor transport of silicon away from the substrate. A key benefit of near-equilibrium thin film growth is that the growth process becomes governed by the law of mass action among the chemical constituents [211]. When mass action holds, the growth of the product (here, graphene) can be viewed as a progression between equilibrium states, with the change controlled by reactant concentrations. An appropriate growth temperature allows rapid surface diffusion, resulting in films of high structural quality. An excellent example of this behavior is found in the case of gallium arsenide MBE where it was found that a steady-state population of gallium and arsenic adatoms persists on the substrate in near-equilibrium with the vapor-phase during growth [212]. Many different possible reactions must be considered for graphene on SiC because at this stage it is unknown which (if any) dominate the growth dynamics. In equations 3.1-3.3 three classes of reactions are described: 1) Decomposition and sublimation of the Si-C system, 2) Etching reactions with an external gas (only hydrogen is shown here), and 3) Nucleation and growth reactions, which ultimately determine the structure of the thin film.

$$\mathrm{SiC}(s) \rightleftharpoons \mathrm{Si}(ad) + \mathrm{C}(ad) \tag{3.1a}$$

$$\mathrm{SiC}(s) + \mathrm{Si}(ad) \rightleftharpoons \mathrm{Si_2C}(ad) \tag{3.1b}$$

$$\mathrm{Si}(ad) \rightleftharpoons \mathrm{Si}(g) \tag{3.1c}$$

$$\mathrm{C}(ad) \rightleftharpoons \mathrm{C}(g) \tag{3.1d}$$

$$\mathrm{Si_2C}(ad) \rightleftharpoons \mathrm{Si_2C}(g) \tag{3.1e}$$

$$\vdots$$

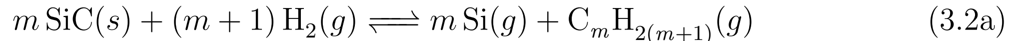

$$m\,\mathrm{SiC}(s) + (m+1)\,\mathrm{H_2}(g) \rightleftharpoons m\,\mathrm{Si}(g) + \mathrm{C}_m\mathrm{H}_{2(m+1)}(g) \tag{3.2a}$$

$$\mathrm{C}(ad) + 2\,\mathrm{H_2}(g) \rightleftharpoons \mathrm{CH_4}(g) \tag{3.2b}$$

$$\mathrm{Si}(ad) + 2\,\mathrm{H_2}(g) \rightleftharpoons \mathrm{SiH_4}(g) \tag{3.2c}$$

$$\vdots$$

$$\mathrm{C}(ad) + N_c\,\mathrm{C}(ad) \rightleftharpoons \mathrm{C}_{N_c+1}(island) \tag{3.3a}$$

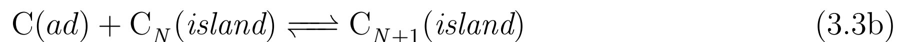

$$\mathrm{C}(ad) + \mathrm{C}_N(island) \rightleftharpoons \mathrm{C}_{N+1}(island) \tag{3.3b}$$

$$\vdots$$

For brevity, vertical dots indicate similar reactions that can occur. At high enough temperature, silicon and silicon-carbon compounds will sublimate from the surface, but at temperatures less than 1800 °C the vapor-phase is dominated by pure silicon, i.e., Equations 3.1a and 3.1c provide the main decomposition pathway. Reactions producing gaseous carbon or carbide molecules typically can be ignored because the equilibrium vapor pressures of these species are negligible. Therefore in the absence of external gases, carbon adatoms remain on the silicon carbide surface. Hydrogen, oxygen, or other gases can participate in etching reactions; for example, at high-temperature hydrogen reacts with the carbon in silicon carbide and graphite to form methane and other hydrocarbon gases (Eqs. 3.2a and 3.2b). Similarly, hydrocarbons can be used to deposit carbon adatoms onto the sample surface for CVD graphene growth [213]. Similar reactions for silicon adatoms (e.g., Eq. 3.2c) may contribute to the loss of silicon adatoms, but the reverse reaction may also be used to deposit silicon onto the substrate depending upon the mass balance of the system. Finally, free carbon adatoms diffuse across the substrate until they either nucleate a graphene island (Eq. 3.3a, with N_c as the critical island nucleus) or join a larger graphene island

(Eq. 3.3b). These adatoms may be single carbon atoms, but for epitaxial growth on Ru Loginova et al. found that island growth occurs via mobile carbon pentamers [86]. The graphene formation reactions are the least understood of those presented (e.g., the critical island size is unknown for graphene on SiC), and the actual growth process is made still more complex by the coupling between carbon diffusion and SiC step dynamics [110].

In this chapter I will present my measurements of the initial growth rate of graphene on both SiC(0001) and SiC(000$\bar{1}$). As graphene layers accumulate the growth rate will decrease, and the exact dependence of growth rate on graphene film thickness will depend upon the film quality [214]. By studying submonolayer graphene coverages on the SiC surface it is possible to focus solely on the initial desorption/adsorption kinetics.The graphene growth thickness was determined using low-energy electron diffraction (LEED) and Auger electron spectroscopy (AES). The experiments presented here explore methods that reduce the net rate of silicon desorption, i.e., control of reactions within equation 3.1. Furthermore, these results are used to develop a simple model that applies to all of the graphene growth techniques described above. In the final part of this study, silane gas as an additional silicon vapor source was introduced to confirm the extra level of control made possible through the reactions in equation 3.2.

3.2 Auger Attenuation Model

Auger electron attenuation measurements are a standard method for determining thin film thicknesses on conductive substrates [215]. The intensity of the substrate Auger electron peak decreases exponentially with thicker overlayer films [216].Auger electron peak intensities vary depending upon the sample composition and morphology and the operating conditions of the AES instrument [217]. Much of this systematic error is eliminated by calculating the ratio of the Auger electron intensities from the substrate

and the film. This is particularly simple when the substrate and thin film are comprised of completely different elements. This procedure is complicated when working with EG on SiC because both the substrate and the graphene film contain carbon. Nevertheless, the silicon Auger electron peak from the SiC decreases exponentially as the average number of graphene layers across the surface increases. An Auger signal attenuation model was previously developed in this laboratory for measuring the graphene thickness on SiC [131], but I have revised substantially to obtain greater accuracy for submonolayer film thickness measurements. It is theoretically possible, however, to use material parameters and the AES instrument design to predict attenuated Auger electron intensity ratios [218]. In this work, Auger signals were measured with the RFA AES electronics operated in the differential mode (see Section 2.3.1). The Auger signal attenuation model assumes the form described previously [131]. In the original model the measured Auger signals from the SiC were normalized using silicon and carbon sensitivity factors, whereas the new model incorporates sensitivity factors derived from the analytical form of the Auger electron current equation and SiC-specific material parameters.

$$I_{XYZ} = I_P \, T \, \sigma_{\alpha,X}(E_P) \, \gamma_{\alpha,XYZ} \, n_\alpha^\beta \, \lambda^\beta(E_{\alpha,XYZ}) \, [1 + r_\alpha^\beta(E_P, E_X)] \tag{3.4}$$

The Auger current I_{XYZ} from an XYZ Auger transition in an atom of element α embedded in a matrix β is defined in Equation 3.4 [219]. The matrix term refers to the environment surrounding and interacting with the atom of element α. For instance, a silicon atom may exist in bulk elemental silicon, an alloy such as SiC, or even some type of homogeneous mixture. The Auger transition probability $\gamma_{\alpha,XYZ}$ is a constant characteristic of an element α undergoing the Auger transition XYZ. The ionization cross-section $\sigma_{\alpha,X}(E_P)$ is dependent on the element, the core level X involved in the Auger transition, and the energy of the primary beam E_P. I_P is the excitatory current of high-energy electron primary beam from the spectrometer

electron gun, and T is the effective transmission rate of the spectrometer analyzer. Several of the terms in equation 3.4 actually depend upon the material matrix β, such as the atomic density, n_α^β, of the element α in the material β. The other two matrix dependent terms are the electron decay length λ^β and the backscattering factor r_α^β. The decay length characterizes the exponential decay in free electron current in matter as a function of electron energy. The backscattering factor models the effect of secondary electron scattering events on the measured spectrometer current. In practice, all of the non-instrument related products in Equation 3.4 are combined to form what are known as sensitivity factors,

$$S_{\alpha,XYZ}^{\beta} = \sigma_{\alpha,X}(E_P)\,\gamma_{\alpha,XYZ}\,\lambda^{\beta}(E_{\alpha,XYZ})\,[1 + r_\alpha^\beta(E_P, E_X)] \tag{3.5}$$

such that,

$$I_{XYZ} = I_P\,T\,n_\alpha^\beta\,S_{\alpha,XYZ}^{\beta} \tag{3.6}$$

Knowledge of the AES analyzer design and the sample material sensitivity factor is all that is strictly necessary to perform quantitative AES [218]. Sensitivity factors are often calculated by taking the ratio of the Auger signals from the experimental materials with the signal from an elemental standard [219]. The sensitivity factors for SiC have not been reported and the measurement of these quantities is not trivial. Bare SiC forms a native oxide in air, and annealing in UHV results in a variety of surface reconstructions that alter the depth-dependent silicon and carbon densities. The SiC sensitivity factor was empirically calculated by measuring the Auger signals of the well-understood $\sqrt{3} \times \sqrt{3}$ surface reconstruction [220]. I used the sensitivity factors for graphite ($S_{C,KLL}^{G} = 0.2$) and pure silicon ($S_{Si,LMM}^{Si} = 0.35$) measured with respect to the Auger signal from a cleaned aluminum substrate [139]. These sensitivity factors were acquired using a cylindrical-mirror analyzer (CMA), which measures the energy-scaled electron distribution $I_P \propto E \cdot N(E)$ with an energy resolution of $\Delta E/E \cong (0.3 - 0.6)\%$. The current measured by the RFA is proportional to the

energy-scaled differential electron distribution $I_P \propto \frac{d[E \cdot N]}{dE}$. Each spectrum acquired by the RFA was numerically transformed into the energy-scaled CMA form in order to use the chosen sensitivity factors [218].

$$\frac{S^{SiC}_{Si,LMM}}{S^{Si}_{Si,LMM}} = \frac{\lambda^{SiC}(E_{Si,LMM})}{\lambda^{Si}(E_{Si,LMM})} \cdot \frac{[1 - r^{SiC}_{Si}(E_p, E_{Si,LMM})]}{[1 + r^{Si}_{Si}(E_p, E_{Si,LMM})]} \tag{3.7a}$$

$$\frac{S^{SiC}_{C,KLL}}{S^{G}_{C,KLL}} = \frac{\lambda^{SiC}(E_{C,KLL})}{\lambda^{G}(E_{C,KLL})} \cdot \frac{[1 - r^{SiC}_{C}(E_p, E_{C,KLL})]}{[1 + r^{G}_{C}(E_p, E_{C,KLL})]} \tag{3.7b}$$

The generic form for the sensitivity factor of an XYZ Auger transition for element α in material β is shown in Equation 3.5 [219]. The bulk atomic density as a function of each atomic layer $n^{\beta}_{\alpha}(z)$, the decay length $\lambda^{\beta}(E_{\alpha,XYZ})$, and the backscattering factor $[1 + r^{\beta}_{\alpha}(E_p, E_X)]$ are the only terms which depend on the material composition [219] or matrix [218]. The ionization cross section $\sigma_{\alpha,X}$ for core level X in element α, and the probability that an excited atom of element α will decay through the XYZ Auger transition $\gamma_{\alpha,XYZ}$, are the same for different compounds containing the same element. Following similar methods described elsewhere [218, 219, 221, 222], these quantities and the elemental sensitivity factors for silicon and graphite were used to calculate the sensitivity factors for SiC (Eq. 3.7). The backscattering factors were calculated using a simple model employed by Leveque and Bonnet, which was found to agree well for both silicon and carbon [223].

Quantitative film thickness measurements with AES require well-calibrated values of the energy-dependent electron decay length and the Auger electron sensitivity factors for each material. The most commond electron decay length used in the quantitative electron spectroscopy is the inelastic mean free path (IMFP) [224], which is defined as "the average of distances, measured along trajectories, that particles with a given energy travel between inelastic collisions in a substance." [225] However, the IMFP neglects the effects of elastic scattering (i.e. diffraction) on electron trajectories [225]. The electron-attenuation length (EAL) is the appropriate parameter for

thin film overlayer experiments because it correctly accounts for the effect of elastic scattering on these types of measurements [216, 226]. The EAL may differ by more than 30% compared to the IMFP for a material [227, 228], and in general is a function of both the electron emission angle and the thin film thickness [229].

Measurement of the EAL for an overlayer-substrate system is complicated by the experimental difficulty of preparing calibrated films of known thickness and composition. I have used the average practical EAL as calculated using the National Institute of Standards and Technology (NIST) Electron Effective-Attenuation-Length Database (SRD 82) [229, 230]. This software program calculates the EAL with an analytical expression for the kinetic Boltzmann equation with the transport approximation [231], using a database of the material IMFP and other electron transport parameters. The graphene EAL was calculated from the experimental elastic-peak electron spectroscopy (EPES) IMFP database where available (energies greater than 200 eV), because EPES is regarded as the most accurate measurement of IMFP [224]. For lower energies the graphene EAL was calculated using IMFP data inferred from optical measurements [232], which agrees well with EPES results in this range of energies [233]. Based upon the sensitivity of the RFA instrument used for AES in the UHV-F system, I used an Auger signal attenuation threshold of 5%. This threshold corresponds to a maximum graphene thickness of 3 ML, which is close to the maximum thickness the RFA is capable of detecting. The EAL calculated for few-layer graphene agrees very well with values measured in a recent scanning AES experiment, although the authors of this paper described the decay length as the IMFP [234]. Figure 3.2 compares the EAL calculated with SRD 82 to the IMFP measured or calculated for graphite using a variety of methods. As expected, the EAL for few-layer graphene is consistently smaller than the bulk IMFP for graphite. The EAL for bulk (infinitely thick) SiC was calculated using only the optical database. Figure 3.3 confirms that the EAL is close to the IMFP for SiC as measured by both the optical

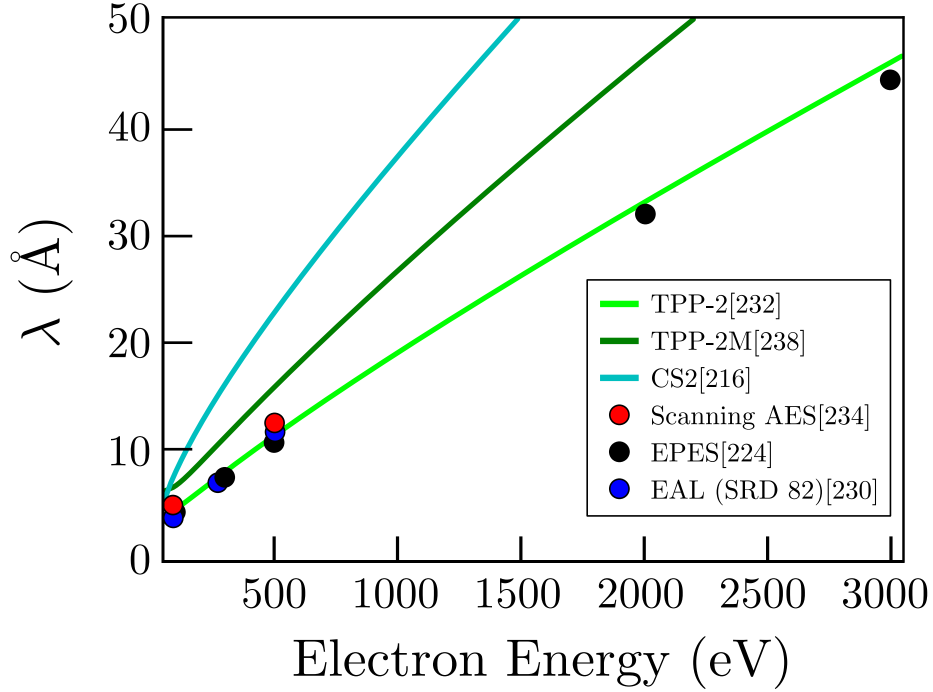

Figure 3.2: Comparison of the different models (lines) and measurements (points) of free electron decay lengths in graphite as a function of electron energy in eV. The electron EAL was calculated using the NIST Electron Effective-Attenuation-Length Database (SRD 82).

method [235] and EPES [236, 237].

Calculations for the Auger electron attenuation model proceeded much like that discussed in a previous work [131]. In short, the model compares the attenuation of the Si LMM Auger electrons from the SiC substrate with the C KLL Auger electrons from both the graphene and the substrate. The figure of merit for these models is a curve which relates the measured Si:C Auger signal ratio to average number of graphene layers on the SiC(0001) and SiC(000$\bar{1}$) surfaces (Fig. 3.4).The new model improved upon the previous one by including more accurate sensitivity factors (Eq. 3.7) and substituting the electron IMFP for the EAL from the SRD 82 [230]. For n graphene layers on the surface of SiC the carbon KLL Auger current from the graphene layers is

$$I_{carbon}^{graphite} = \sum_{m=1}^{n} I_{G,m} = \frac{1 - \exp\left[(-n)(\eta_{E_P}^{G} + \eta_{272eV}^{G})\right]}{1 - \exp\left[(-1)(\eta_{E_P}^{G} + \eta_{272eVG}^{G})\right]} \tag{3.8}$$

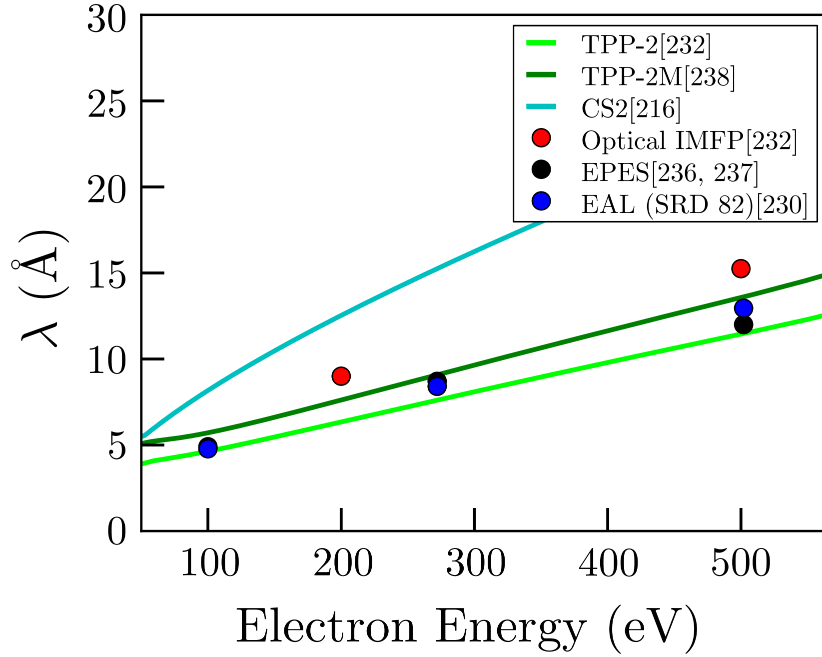

Figure 3.3: Comparison of the different models (lines) and measurements (points) of free electron decay lengths in SiC as a function of electron energy in eV. The electron EAL was calculated using the NIST Electron Effective-Attenuation-Length Database (SRD 82).

where $\eta^{\beta}_{eV} = (d_{\beta}/\lambda^{\beta}_{eV}) \times \cos(42.2°)$ is the ratio of the interlayer thickness d_{β} and the electron EAL for the material β (graphene or SiC) at kinetic energy eV, evaluated a take-off angle of 42.2° (which accounts for the acceptance angle of the RFA in the UHV-F system) [215]. For graphene the interlayer thickness of graphite was used ($d_G = 3.35\,\text{Å}$), and for SiC the bilayer height was used ($d_{SiC} = 2.5\,\text{Å}$). Structural models for the graphitized SiC surfaces are necessary to derive the Auger electron attenuation model in equations 3.8 - 3.12. The SiC(0001) surface develops a carbon-rich buffer layer between bare SiC and the first graphene layer [133, 207, 208, 239]. The buffer layer is modeled as a graphene layer covalently bonded to the SiC surface as motivated by recent experimental results [5, 213, 240]. It is possible to prepare a SiC(0001) surface with almost the entire surface covered by the graphene-SiC buffer layer as confirmed by LEED and scanning tunneling microscopy (STM) measurements

(see Section 2.3.2). My AES film thickness measurements on these samples are consistent with a SiC(0001) surface covered by a single layer of graphene. Therefore, I have modeled the EG/SiC(0001) interface as bare SiC, where the '1st' layer of graphene that is actually the covalently bonded graphene-SiC buffer layer. The carbon KLL and silicon LMM Auger currents from the top-most SiC bilayer are calculated by assuming attenuation from the graphene overlayers and partial attenutation from the partially subsurface carbon component of the SiC bilayer.

$$I_{Si,1}^{\mathrm{SiC(0001)}} = I_P T \cdot \exp\left[(-n)(\eta_{E_P}^{G} + \eta_{90eV}^{G})\right] \times \frac{n^{SiC}}{n^G} \cdot \frac{S_{Si,LMM}^{SiC}}{S_{C,KLL}^{G}} \tag{3.9a}$$

$$I_{C,1}^{\mathrm{SiC(0001)}} = I_P T \cdot \exp\left[(-n)(\eta_{E_P}^{G} + \eta_{272eV}^{G}) - \frac{1}{2}(\eta_{E_P}^{SiC} + \eta_{272eV}^{SiC})\right] \times \frac{n^{SiC}}{n^G} \cdot \frac{S_{C,KLL}^{SiC}}{S_{C,KLL}^{G}} \tag{3.9b}$$

This equation is referenced to the ratio of the atomic densities of SiC (n^{SiC}, respectively) and graphite (n^G). The Si and C Auger currents from SiC were normalized by the sensitivity factors calculated in equation 3.7. Once the Auger current from the topmost SiC bilayer is calculated, it is trivial to calculate the Auger current from bulk SiC by finding the summation of an infinite number of SiC bilayers.

$$I_{silicon}^{\mathrm{SiC}} = \sum_{m=1}^{\infty} I_{Si,m}^{\mathrm{SiC<0001>}} = \frac{I_{Si,1}^{\mathrm{SiC<0001>}}}{1 - \exp\left[(-1)(\eta_{E_P}^{SiC} + \eta_{90eV}^{SiC})\right]} \tag{3.10a}$$

$$I_{carbon}^{\mathrm{SiC}} = \sum_{m=1}^{\infty} I_{C,m}^{\mathrm{SiC<0001>}} = \frac{I_{C,1}^{\mathrm{SiC<0001>}}}{1 - \exp\left[(-1)(\eta_{E_P}^{SiC} + \eta_{272eV}^{SiC})\right]} \tag{3.10b}$$

Finally, the ratio of the Si and C Auger electrons is calculated using Equations 3.8 through 3.10.

$$\frac{Si_{Auger}}{C_{Auger}} = \frac{I_{silicon}^{\mathrm{SiC}}}{I_{carbon}^{\mathrm{SiC}} + I_{carbon}^{\mathrm{graphite}}} \tag{3.11}$$

Compared to the SiC(0001) surface, the EG interfacial layer on the SiC($000\bar{1}$) is much more poorly understood. Synchrotron X-ray diffraction on graphitized SiC($000\bar{1}$) has indicated the presence of a carbon-rich interface [241]. One group has recently

determined that the carbon face forms a graphene-like buffer layer that is stable when the oxygen exposure is minimized [6]. In this work, the furnace chamber gas line (see Fig. 2.11 in Section 2.2) was pumped down to 10^{-7} mbar before attempting growth, so the oxygen impurity concentration was certainly high enough to remove any evidence of a carbon face buffer layer. Consequentially and in agreement with ellipsometry measurements of few-layer graphene on SiC(000$\bar{1}$) [19], the carbon face interface was modeled as bare SiC. The Auger currents from the SiC(000$\bar{1}$) are similar in form to the currents from the SiC(0001) surface (Eqn. 3.10), but must be altered to respect the different polar termination (the SiC(0001) surface is Si-terminated, while the SiC(000$\bar{1}$) surface is C-terminated).

$$I_{Si,1}^{\mathrm{SiC}(000\bar{1})} = I_P T \cdot \exp\left[(-n)(\eta_{E_P}^{G} + \eta_{90eV}^{G}) - \frac{1}{2}(\eta_{E_P}^{SiC} + \eta_{90eV}^{SiC})\right] \times \frac{n^{SiC}}{n^{G}} \cdot \frac{S_{Si,LMM}^{SiC}}{S_{C,KLL}^{G}} \quad (3.12a)$$

$$I_{C,1}^{\mathrm{SiC}(000\bar{1})} = I_P T \cdot \exp\left[(-n)(\eta_{E_P}^{G} + \eta_{272eV}^{G})\right] \times \frac{n^{SiC}}{n^{G}} \cdot \frac{S_{C,KLL}^{SiC}}{S_{C,KLL}^{G}} \quad (3.12b)$$

The figure of merit for these models is a curve which relates the measured Si/C Auger signal ratio to average number of graphene layers on the SiC(0001) and SiC(000$\bar{1}$) surfaces (Fig. 3.4). Structural models for the graphitized SiC surfaces are necessary to derive the Auger electron attenuation model in equations 3.8-3.12. The SiC(0001) surface develops a carbon-rich buffer layer between bare SiC and the first graphene layer [133, 207, 208, 239]. The buffer layer is modeled as a graphene layer covalently bonded to the SiC surface as motivated by recent experimental results [5, 213, 240]. It is possible to prepare a SiC(0001) surface with almost the entire surface covered by the graphene-SiC buffer layer as confirmed by LEED and scanning tunneling microscopy (STM) measurements (see Section 2.3.1). My AES film thickness measurements on these samples are consistent with a SiC(0001) surface covered by a single layer of

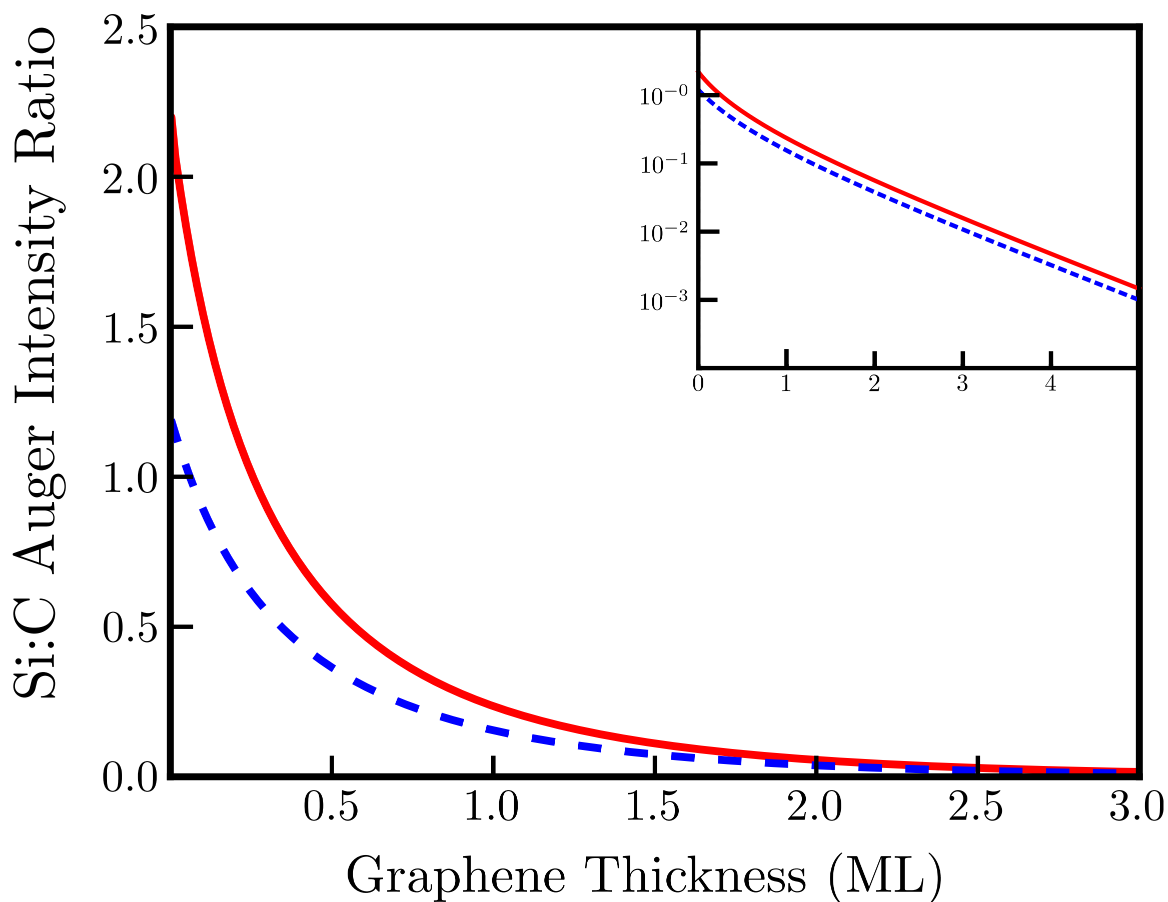

Figure 3.4: Theoretical model of the attenuation of the Si LMM Auger electron signal relative to the C KLL Auger signal for graphene on both SiC(0001) (red/solid line) and SiC(000$\bar{1}$ (blue/dashed line). An abrupt interface between SiC and graphene was assumed based upon the most recent models of these systems [5, 6]. The inset shows the same plot on a logarithmic scale which demonstrates that the Si Auger intensity decays with the same exponential slope for both SiC surfaces. The offset between the two curves is due to the different relative orientation of the Si-C bilayer for each SiC surface termination.

graphene, and provide a better means of determining graphene sample coverage compared to the previous model [131].

3.3 Kinetic Theory of Graphene Growth on Silicon Carbide

In a 1D geometry the graphitization rate of SiC is fundamentally controlled by the silicon and carbon vapor rate equations:

$$\dot{n}_{\mathrm{Si}} = \frac{1}{V}\left(\sum_i A_i \cdot F^i_{silicon} + \sum_j A_j \cdot F^j_{silicon}\right) \tag{3.13a}$$

$$\dot{n}_{\mathrm{C}} = \frac{1}{V}\left(\sum_i A_i \cdot F^i_{carbon} + \sum_j A_j \cdot F^j_{carbon}\right) \tag{3.13b}$$

where $\dot{n}_x$ is the net rate of change of Si or C density in the volume surrounding the SiC substrate, V is the internal furnace volume, F^i_x and F^j_x are expressions for all possible sources and sinks of Si or C vapor, and A_i is the relevant area for a particular flux term. For example, the contribution to the silicon vapor from SiC sublimation $F^{\mathrm{SiC}}_{silicon}$ is multiplied by the surface area of SiC A_{SiC}. The graphene growth rate equation for SiC is dependent only on source flux terms from the SiC and sink flux terms for deposition onto the SiC,

$$\dot{g}(t) = \frac{F^{\mathrm{SiC}}_{silicon} + F^{gas}_{carbon} + F^{\mathrm{SiC}}_{carbon} + F^{gas}_{silicon}}{\rho_G} \tag{3.14a}$$

$$F^{\mathrm{SiC}}_{silicon} = F^{\mathrm{SiC}}_{\mathrm{Si}} + 2F^{\mathrm{SiC}}_{\mathrm{Si_2C}} + F^{\mathrm{SiC}}_{\mathrm{SiC_2}} + F^{\mathrm{SiC}}_{\mathrm{SiH_4}} \tag{3.14b}$$

$$F^{\mathrm{SiC}}_{carbon} = F^{\mathrm{SiC}}_{\mathrm{Si_2C}} + 2F^{\mathrm{SiC}}_{\mathrm{SiC_2}} + F^{\mathrm{SiC}}_{\mathrm{CH_4}} \tag{3.14c}$$

where ρ_G is the atomic density of single monolayer of graphene. Loss of Si vapor from the substrate ($F^{\mathrm{SiC}}_{silicon}$) and deposition of C ($F^{gas}_{carbon}$) provides C adatoms for graphene formation. Likewise, loss of C containing vapor ($F^{\mathrm{SiC}}_{carbon}$) and Si deposition ($F^{gas}_{silicon}$) tends to reduce the total amount of C adatoms available for graphene growth. The fluxes in Equation 3.14 correspond to the sublimation/condensation and etching/deposition reactions in equations 3.1 - 3.2. The benefit of formulating the

graphitization rate in terms of equations 3.13 and 3.14 is that it can describe nearly every scenario for graphene growth on SiC. Nevertheless, the large number of possible chemical reactions which can contribute to graphitization obfuscates a first-principle investigation.

The open geometry, UHV configuration is attractive because $\dot{n}_{\mathrm{Si}} = 0$ and $n_{\mathrm{Si}} = 0$ as silicon vapor cannot accumulate in the chamber, and therefore only the physical sublimation parameters are relevant. The problem simplifies further because only monoatomic silicon sublimation is prevalent in the common experimental temperature range of $1250 - 2000\,^{\circ}\mathrm{C}$. With these assumptions equation 3.14a simplifies to $\dot{g}(t) = \frac{F_{\mathrm{Si}}^{\mathrm{SiC}}}{\rho_G}$, and the submonolayer graphitization rate becomes equimolar with the silicon sublimation rate. Although advantageous for certain studies, silicon sublimation and graphene growth occurs out of equilibrium in the open geometry, UHV configuration, resulting in difficult process control and poor surface quality. The problems associated with the open geometry, UHV configuration are ameliorated by including additional sources of silicon vapor. For instance, EG has been grown on SiC in UHV systems in the presence a silicon-precursor gas [6, 242, 243] or with direct flux of sublimated silicon [244]. These silicon sources enter Equation 3.13a as a constant, effective Si vapor density n_{Si} which reduces the SiC sublimation rate F_{Si}^{SiC} in equation 3.15. In the CCS configuration residual silicon on the furnace walls acts as an additional source of silicon vapor F_{Si}^{wall} in equations 3.13a retarding the sublimation rate of the SiC sample. Powdered silicon will react with carbon nanotubes to form SiC at temperatures above $1000\,^{\circ}\mathrm{C}$ [245]. Silicon *vapor* does not react with graphite at temperatures below $1700\,^{\circ}\mathrm{C}$ [246]. However, SiC formation has been observed on the walls of the graphite enclosures used in CCS furnaces for expitaxial graphene growth on SiC samples [247]. It is likely that after many heating cycles that a significant quantity of elemental silicon will accumulate on the walls of a CCS furnace and react with the graphite walls to form SiC. Since the UHV-F furnace was operated at temperatures below $1700\,^{\circ}\mathrm{C}$

any silicon deposition onto the furnace walls should occur primarily during after furnace is allowed to cool. Furthermore, after *each* growth experiment the furnace was outgassed at $1600\,^{\circ}$C to prevent solid-phase silicon enrichment. Therefore, the only sources of silicon vapor in our experiments are from the SiC sample or from a silicon-precursor gas. The enclosure in CCS furnace limits the physical vapor transport, or leak rate, of gas out of or into the furnace (F_{leak}) [19]. In general F_{leak} can be either positive or negative depending upon the relative silicon density inside and outside of the furnace. Multiple leak terms are necessary if the furnace is heated in the presence silicon or carbon containing gas species. In this work I have only considered the effect of silicon gas species, particularly in the form of silane (SiH_4). Therefore, the Si vapor rate equation $\dot{n}_{\mathrm{Si}} = (1/V)(A_{\mathrm{SiC}} \cdot F_{\mathrm{Si}}^{\mathrm{SiC}} + A_{wall} \cdot F_{\mathrm{Si}}^{wall} + A_c \cdot F_{\mathrm{Si}}^{leak})$ in the CCS furnace configuration, where A_{SiC} and A_{wall} are the surface area of the SiC substrate and the internal furnace walls, respectively, and A_c is the cross-sectional area of the furnace leak orifice.

The sublimation rate of monoatomic SiC is modeled using the Hertz-Knudsen equation (Eqn. 3.15) [248]:

$$F_{\mathrm{Si}}^{\mathrm{SiC}} = \beta \frac{\bar{v}_{\mathrm{Si}}}{4}(n_{\mathrm{Si}}^{eq} - n_{\mathrm{Si}}) \tag{3.15}$$

In the Hertz-Knudsen equation $\bar{v}_{\mathrm{Si}}$ is the average thermal speed of silicon atoms in the vapor, n_{Si} is the silicon vapor density in the isothermal volume V (assuming that the vapor density is homogenous), and β is the SiC evaporation coefficient [214]. The equilibrium silicon vapor density sublimated from SiC, $n_{\mathrm{Si}}^{eq} = (C_0/k_B T)e^{-\frac{\Delta H}{k_b T}}$, is a function of only the furnace temperature, where C_0 is a constant and ΔH is the enthalpy of sublimation for SiC [105].

The leak rate is formulated in terms of the general equation of diffusion with isothermal/isobaric conditions and no external forces (Eqn. 3.16) [249], which is

valid for the pressures/temperatures studied:

$$F_{\mathrm{Si}}^{leak} = \frac{n^2}{n_{\mathrm{Ar}}} D \nabla (\frac{n_{\mathrm{Si}}}{n}) = \frac{n}{n_{\mathrm{Ar}}} \frac{D}{h} \Delta n_{\mathrm{Si}} \tag{3.16}$$

Here h is the length the furnace leak hole, which in the UHV-F system corresponds to the annular space between the graphite furnace and sample holder (see inset of Figure 2.11). The relative silicon density $\Delta n_{\mathrm{Si}} = n_0^{ext} - n_{\mathrm{Si}}$, where n_{Si}^{ext} is the silicon density outside of the furnace. D is the effective diffusivity of the annular pore, where the effective diffusivity models the probability for silicon atoms to leak out of the furnace. The diffusivity is decreased by interatomic collisions (bulk gas or Fickian diffusion) and collisions with the wall of the annular pore (molecular or Knudsen flow). The effective diffusivity is described by the Bosanquet equation [250, 251],

$$\frac{1}{D} = \frac{1}{D_K} + \frac{1}{D_F} \tag{3.17}$$

In the Knudsen flow regime the conductance of the leak is calculated directly from the kinetic theory of gases as $U = A_c(\bar{v}_{\mathrm{Si}}/4)W$, where the transmission probability W only depends on the geometry of the leak [252]. Because the width of the annular pore is relatively large compared to the surface roughness, it is reasonable to express this conductance in terms of a diffusivity D_K (Eqn. 3.18).

$$D_K = U\frac{h}{A_c} = h\frac{\bar{v}_{\mathrm{Si}}}{4}W \tag{3.18}$$

Following a treatment of this problem given by Turner [253], the transmission probability for the annular pore between the furnace and the rest of the growth chamber is given in Equation 3.19.

$$\begin{aligned} \delta &= \frac{\pi(2r-d)}{d} \\ C &= \frac{3}{8}\ln(2\delta) + \frac{3}{8}\delta\ln(1+\frac{1}{\delta}) \\ W &= \frac{d(2r-d)}{(r-d)^2}\frac{1}{(2+\frac{3h}{8dC})} \end{aligned} \tag{3.19}$$

The Fickian diffusivity D_F was modeled using the first approximation of the elastic rigid sphere with the Chapman-Enskog theory [249]. The generalized Chapman-Enskog equation for the diffusion of a gas A in the presence of gas B is given in equation 3.21.

$$\frac{1}{D_F} = \frac{1}{D_{\mathrm{Si,Si}}} + \frac{1}{D_{\mathrm{Si,Ar}}} \tag{3.20}$$

$$D_{\mathrm{Si,Ar}} = \frac{3}{8n\sigma_{\mathrm{Si,Ar}}}\left[\frac{k_B T(m_{\mathrm{Si}} + m_{\mathrm{Ar}})}{2\pi m_{\mathrm{Si}} m_{\mathrm{Ar}}}\right]^{\frac{1}{2}} \propto \frac{T^{\frac{3}{2}}}{P} \tag{3.21}$$

Both Fickian diffusivities depend on the total gas density $n = n_{\mathrm{Si}} + n_{\mathrm{Ar}}$, the reduced atomic mass $\frac{m_{\mathrm{Si}}+m_{\mathrm{Ar}}}{m_{\mathrm{Si}} m_{\mathrm{Ar}}}$, and the average collision diameter $\sigma_{\mathrm{Si,Ar}} = \frac{1}{2}(\sigma_{\mathrm{Si}} + \sigma_{\mathrm{Ar}})$.

Modeling the silicon vapor flux from the residual silicon on the furnace walls is complicated by the fact that we do not know if it is elemental Si or SiC, and the graphite used for CCS furnace can be porous. To simplify the residual furnace silicon. I have chosen to model it as a constant, initial silicon density. Solving the rate equation $\dot{n}_{\mathrm{Si}} = (1/V)(A_{\mathrm{SiC}} \cdot F_{\mathrm{Si}}^{\mathrm{SiC}} + A_c \cdot F_{\mathrm{Si}}^{leak})$ results in the time-dependent density of silicon vapor:

$$n_{\mathrm{Si}}(t) = n^* + (n_0 - n^*)e^{\frac{-t}{\tau}} \tag{3.22a}$$

$$n^* = \frac{n_{\mathrm{Si}}^{eq}}{1+\epsilon} + \frac{n_{\mathrm{Si}}^{ext}}{1+\epsilon^{-1}} \tag{3.22b}$$

$$\epsilon = \frac{4}{\bar{v}_{\mathrm{Si}}} \frac{A_c}{\beta A_{\mathrm{SiC}} \frac{n}{n_{\mathrm{Ar}}} \frac{D}{h}} \tag{3.22c}$$

$$\tau = \frac{4V}{\beta A_{\mathrm{SiC}}(\bar{v}_{\mathrm{Si}} + 4\frac{A_c}{\beta A_{\mathrm{SiC}}} \frac{n}{n_{\mathrm{Ar}}} \frac{D}{h})} \tag{3.22d}$$

where n_0 is the constant, initial silicon density from the furnace walls and n* is the steady-state silicon density inside the furnace (Eqn. 3.22b). The ϵ characterizes the relative degree of confinement for any particular furnace. When the furnace is well-confined $\epsilon \ll 1$ (Eqn. 3.22c) because the leak rate is slow relative to the silicon sublimation rate and $n^* \approx n_{\mathrm{Si}}^{eq}$. When the furnace is poorly confined $\epsilon \gg 1$ and

the steady-state silicon vapor density will approach the density outside the furnace, $n^* \approx n_{\mathrm{Si}}^{ext}$. In general, n_{Si}^{ext} is either constant or slowly varying with respect to the time constant τ (Eqn. 3.22d).

The graphitization rate $\dot{g}$ is proportional to the silicon sublimation rate F_{Si}^{SiC} (Eqn. 3.15). For the UHV-F geometry and taking $\beta = 1$ The steady-state silicon vapor density n^* is within 5% of the equilibrium silicon vapor density n_{Si}^{eq} in the Knudsen regime, and the deviation decreases at higher inert gas pressure. The characteristic time constant τ (Eqn. 3.22d) is approximately 40 μs for UHV-F, so the silicon vapor density is essentially at steady-state throughout the entire growth. At steady-state, $F_{Si}^{\mathrm{SiC}} = F_{Si}^{leak}$ so the graphitization rate is proportional to the saturation density n^* and the effective diffusivity D. Therefore, after a short transient period graphene grows at a constant rate when the graphene/SiC system is in near-equilibrium with the surrounding vapor-phase.

The functional dependence of the graphene growth rate on furnace temperature and pressure exhibits three regimes: a low-pressure regime where the growth rate is controlled by the geometric size of the leak (Eqn. 3.23a), a high-pressure regime where the growth rate is further limited by diffusion through the gas (Eqn. 3.23b), and an intermediate regime where the Knudsen and Fickian diffusivities contribute equally to the leak rate.

$$\dot{g}\, T^{\frac{1}{2}} = \dot{G}_K = \Psi_K \cdot e^{-\frac{\Delta H}{k_B T}} \tag{3.23a}$$

$$\dot{g}\, \frac{P}{T^{\frac{1}{2}}} = \dot{G}_F = \Psi_F \cdot e^{-\frac{\Delta H}{k_B T}} \tag{3.23b}$$

There are some limitations to the model as currently presented. First of all, this model is only correct for submonolayer growth. As more graphene forms and covers the surface, it becomes increasingly more difficult for silicon vapor to escape the layered structure [214]. This is a purely kinetic effect that can be modeled by a decrease in the evaporation coefficient β as the graphene thickness increases. A

specific analytical expression for β would depend upon the graphene stacking orientation and the possible presence of a stable, strongly bound interfacial buffer layer. Other more poorly understood factors would alter the form of β, such as the type, density, and location of defects present throughout the graphene layers. For example, the graphene growth rates on hexagonal silicon carbide are dramatically different for thicker graphene films with larger domains, as discussed in the following section. In addition, I have only presented the results of the graphene growth model pertinent to the CCS configuration.

3.4 Results

3.4.1 High Pressure Argon Growth

Graphene samples grown in an argon environment were studied with LEED to gain insight into the composition and quality of the epitaxial film. According to graphene thickness measurements collected with AES, the SiC(0001) surfaces were mostly covered by the graphene buffer layer irrespective of changes in growth temperature or pressure. The graphene, SiC, and $(6\sqrt{3} \times 6\sqrt{3})$R30° diffraction peaks are visible at most electron energies. The intensity of the graphene and SiC diffraction spots shown in Figure 3.5 are essentially the same indicating that this particular sample is predominantly buffer layer graphene [254]. This identification was confirmed by Auger electron attenuation measurements (not shown). The diffraction patterns are strikingly similar to the ones observed in previous epitaxial graphene growth on SiC(0001) in UHV, despite the fact that these samples were grown in relatively high pressures of argon. The similarities in the diffraction pattern between the two cases implies that the complex chemical bonding between the SiC and graphene is maintained when grown in a high-pressure inert gas, and more broadly that the graphitization mechanisms for enclosed geometry, CCS and open geometry, UHV configurations are related. Diffraction patterns from the SiC($000\bar{1}$) surfaces graphitized in the UHV-F

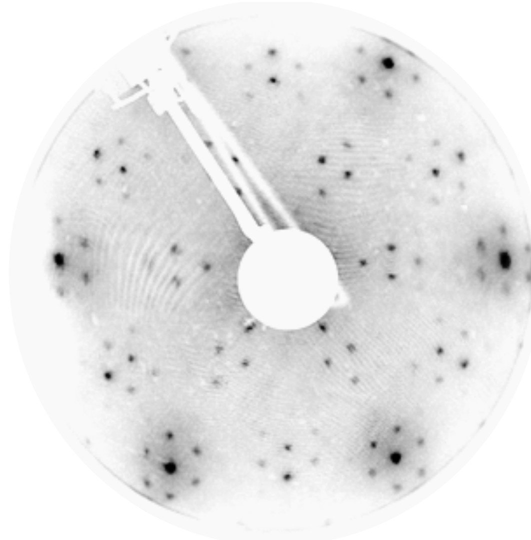

72 eV

Figure 3.5: LEED pattern from EG grown on SiC(0001) in the UHV-F furnace. This sample was grown until 1 ML of graphene surface coverage corresponding to predominantly buffer layer graphene on SiC(0001), as confirmed by the prominence of the graphene, SiC, and $(6\sqrt{3} \times 6\sqrt{3})$R30° diffraction peaks.

furnace (Fig. 3.6) are very different from the ones observed in earlier UHV studies [205]. The SiC(000$\bar{1}$) graphene is epitaxial with the SiC substrate at 0° and 30°. The diffraction spots are azimuthally broadened by between $\pm\, 2^\circ - 7^\circ$ depending upon the growth conditions.[1] These broadened spots indicate rotational disorder in the graphene domains, as was seen previously for high-quality multilayer epitaxial graphene [241, 255]. In general, the diffraction spots rotated at 30° with respect to the SiC are more intense compared to weaker spots near 0°, especially for submonolayer graphene coverages (Fig. 3.6a). The near 0° spots are much more intense on thicker graphene films grown in the UHV-F furnace (Fig. 3.6b). The intensification of the near-0° spots as a function of graphene coverage demonstrates that the first layer of graphene grown on SiC(000$\bar{1}$) is formed in good epitaxy with the SiC surface, and subsequently grown layers accrue 30° rotational stacking faults.

The azimuthal broadening of the epitaxial graphene diffraction spots on SiC(000$\bar{1}$)

[1]These angles were measured using the GNU Image Manipulation Program's 'Measure' tool.

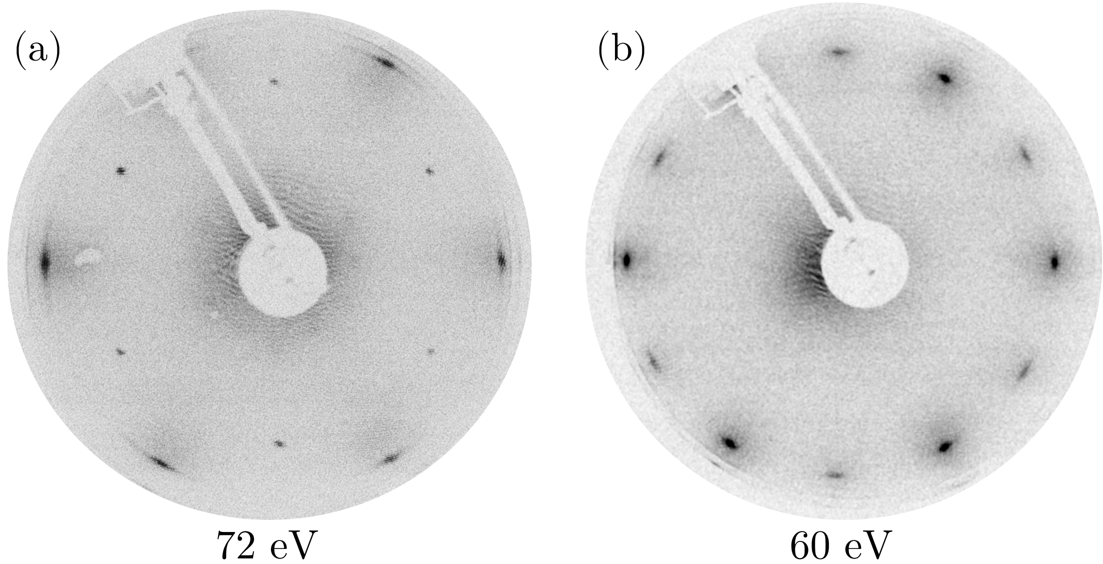

Figure 3.6: LEED patterns from EG grown on SiC(000$\bar{1}$) in the UHV-F furnace. (a) LF003 was heated at 1450 °C for 20 minutes in 827 mbar of argon gas, which resulting in 0.4 ML of graphene. Graphene diffraction spots are epitaxial with the SiC by 30 degree rotation, and there is very little azimuthal broadening. (b) LF011 was graphitized at 1625 °C for 20 minutes in 827 mbar of argon gas. The average graphene thickness on LF011 was 3.2 ML, as confirmed the lack of visible SiC spots. All graphene spots were broadened azimuthally but there was no 'ring' of diffraction intensity characteristic of rotational disorder.

is attributed to rotational stacking faults between either (a) domains within a single graphene layer or (b) different graphene layers [241]. For instance, the diffraction pattern for graphene on SiC(000$\bar{1}$) grown in the open geometry, UHV configuration is almost entirely disordered in the azimuthal direction [111, 205]. These graphene diffraction 'rings' or 'streaks' are commonly observed for EG grown on SiC(000$\bar{1}$) grown in the CCS furnace configuration [19], although in this case it has been shown that the graphene films are not entirely disordered [241, 256, 257]. These diffraction spots of conventional CCS-style multilayer graphene on SiC(000$\bar{1}$) are much broader than the spots from the UHV-F furnace and a significant amount of diffraction from graphene domains are visible at every orientation (measured using the LEED optics in the UHV-F system) [19]. Nevertheless, the majority of the graphene domains do have an epitaxial relationship with the SiC. In this particular example the diffraction

spots near-0° have the greatest intensity at about ±7°. In the past, samples grown in the de Heer CCS furnace exhibited near-0° spots at ±2.2° [255]. Other groups have reported similar results but with different near-0° spot orientations [6]. Although the UHV-F and de Heer furnaces are similarly constructed, I have operated my furnace in an initially silicon deficient state by high temperature outgassing prior to any growth experiment. As will be discussed in the silane section below, the additional silicon has an immediate effect on the apparent domain size and rotational order of EG films on SiC(000$\bar{1}$). It is also likely that variations in the substrate material have a drastic effect on the evolution of the rotational disorder in multilayer epitaxial graphene [258].

I measured the time-averaged growth rates (ie. carbon coverage/growth time) for samples with less than or equal to one ML of graphene. For the purposes of this work I do not distinguish between pristine graphene and graphene-SiC interfacial superstructures, such as the silicon face buffer layer [5, 213, 240]. The average growth rates for all of the samples grown in this furnace are shown in Figure 3.7. The growth rates demonstrate no clear trend with respect to growth temperature (Fig. 3.7a) or argon pressure (Fig. 3.7b). However, graphene growth rates normalized using the high-pressure limit of equation 3.23b (ie. scaled by a factor of $P/T^{\frac{1}{2}}$) have a clear exponential dependence on the inverse furnace temperature. The normalized growth rates do not show any clear dependence on the SiC polytype, surface polarity, or surface preparation. The lines in Figure 3.8 were calculated by an orthogonal distance regression fitting algorithm[2] of Equation 3.23b to the scaled graphene growth rate data for each SiC surface. For the carbon face (solid line) the fitting parameters are: $\log \Psi_F = 31.32 \pm 2.50 \log\left(\frac{ML}{sec}\,\text{mbar}\,K^{-\frac{1}{2}}\right)$, and $\Delta H = 5.33 \pm 0.36$eV. For the silicon face (dashed line) the fitting parameters are: $\log \Psi_F = 34.33 \pm 3.77 \log\left(\frac{ML}{sec}\,\text{mbar}\,K^{-\frac{1}{2}}\right)$, and $\Delta H = 5.81 \pm 0.54$ eV. The ΔH terms

[2]Fit to data was calculated using the orthogonal distance regression algorithm in the Scipy Python package.

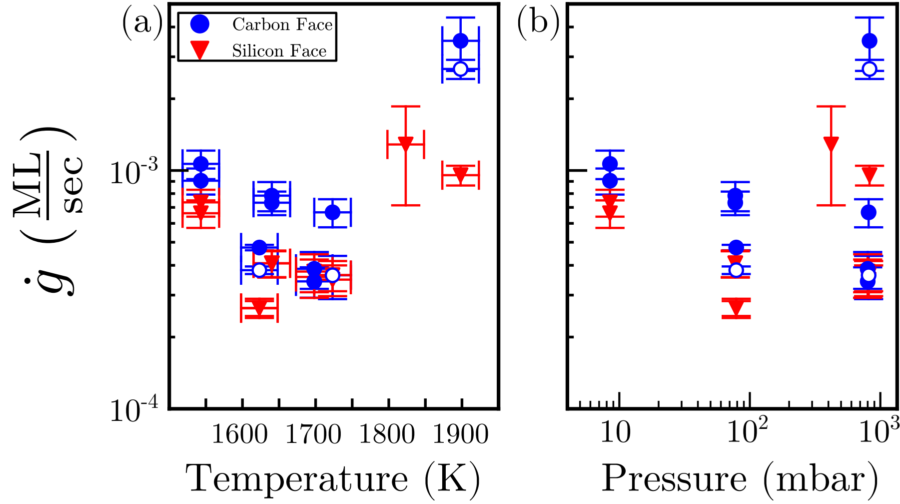

Figure 3.7: Graphene growth rates versus (a) temperature and (b) pressure for both of the SiC terminations studied. Carbon face CMP samples are indicated with an open symbol, all other samples were hydrogen etched prior to growth.

agree well with the enthalpy of sublimation from the literature for the SiC-C system (which were previously reported in terms of the base 10 logarithm) [105]. The SiC-C system is defined as SiC exposed to an abundance of additional carbon. The vapor pressure of SiC in the SiC-C system was studied by heating an equimolar mixture of SiC and graphite powder in high-temperature Knudsen cell [214]. Ψ_F is strongly dependent on the geometric shape and size of the furnace, and as such a CCS furnace can be characterized by the measured Ψ_F.

The growth rates for the two SiC faces are almost equivalent for submonolayer graphene coverages. Previous observations clearly show that the growth rates for each SiC face diverges as a function of film thickness [256]. The gray region in Figure 3.8 delineates the few multilayer samples grown in this study. In contrast with the submonolayer samples, the growth rate for multilayer samples was much slower than predicted by equation 3.23b. It is logical to assume that previously formed graphene layers present a kinetic barrier to further graphitization. The growth rate should be

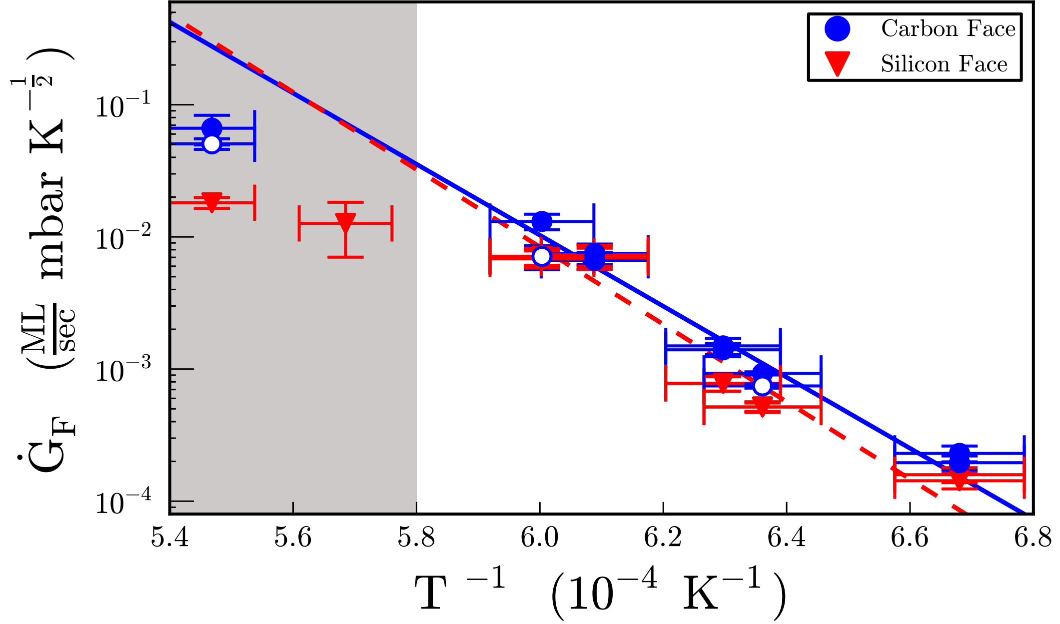

Figure 3.8: Graphene growth rates for carbon face (triangles) and silicon face (circles) SiC, normalized according to the sublimation-diffusion relationship derived in Equation 3.23b. The fits to equation 3.23b for each silicon carbide termination is displayed to show the high level of agreement with the proposed model. For the carbon face (solid line), $\log \Psi_F = 31.32 \pm 2.50 \log\,(\frac{ML}{sec}\,\text{mbar}\,K^{-\frac{1}{2}})$, and $\Delta H = 5.33 \pm 0.36$eV. For the silicon face (dashed line), $\log \Psi_F = 34.33 \pm 3.77 \log\,(\frac{ML}{sec}\,\text{mbar}\,K^{-\frac{1}{2}})$, and $\Delta H = 5.81 \pm 0.54$ eV. Carbon face CMP samples are indicated with an open symbol. Data points in the grey region are samples which were grown to more than a single monolayer of carbon as determined by AES and/or ellipsometry.

strongly dependent on the evaporation coefficient β, which models the mechanisms which kinetically limit silicon sublimation. It has been shown that SiC-graphite can have very small evaporation coefficients ($2 \cdot 10^{-3}$ to $5 \cdot 10^{-2}$) sublimated in Knudsen cells similar to the UHV-F furnace [214, 259].Figure 3.8 also shows that the growth rate of multilayer carbon face samples is faster than the growth rate of multilayer silicon face samples. Part of this discrepancy may be due to the sample quality. The surface of the carbon face samples grown in these conditions was roughened by large pits, some of which are several nanometers deep (Fig. 3.9a). The silicon face samples were step bunched with an average step-height of 4 nm, with comparatively smooth terraces (Fig. 3.9b). The overall film thickness appears to play a minor role in the reduction of the carbon face growth rate (3.7 graphene layers for the multilayer samples in Figure 3.8, as measured by ellipsometry). In contrast, the silicon face growth rate almost seems to saturate after the formation of a complete buffer layer across the sample (Only 1.25 graphene layers for the multilayer samples in Figure 3.8, as measured by AES). It is likely that the strongly-coupled buffer layer on the silicon face presents a much larger kinetic barrier to further sublimation/graphitization compared to the decoupled graphene layers on the carbon face. In addition, the film thickness of silicon face graphene grown in UHV is determined primarily by temperature; higher temperatures will produce thicker graphene films, but longer growth time will have little effect on the final thickness [8, 205, 208, 210]. Therefore, a change in the thermodynamic barrier to sublimation (i.e. ΔH) for the buffer layer/silicon carbide interface may not be ruled out at this time. Despite difficulties in using this model to predict graphitization rates a priori, empirically determined values of Ψ_F and ΔH can be used to calibrate the graphitization growth rates for all well-confined furnaces.

A similar analysis is possible for growth in systems where gases are used under

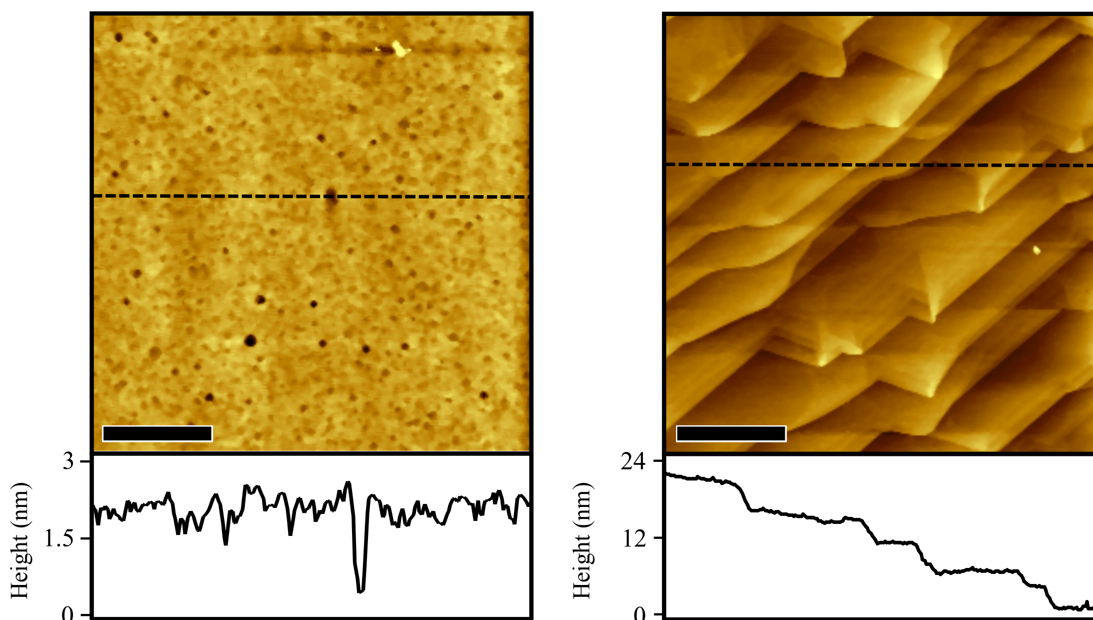

Figure 3.9: AFM of two samples grown simultaneously at 1625 ° C for 20 minutes in 827 mbar of argon gas. The height profiles were acquired along the dashed lines in each image. (a) The carbon face of Sample LF011 has an average surface coverage of 3.2 ML of graphene, with an RMS surface roughness of 0.35 nm. The surface has roughened following graphitization, such that the original unit-cell step structure is no longer visible in this image. (b) In contrast, the silicon face of sample LF010 has an average surface coverage of 1.15 ML, and the steps have bunched into 4.06 ± 0.94 nm steps. The terraces between each step bunch have an RMS surface roughness of 0.14 nm.

continuous flow. This technique has been used successfully to grow large-scale homogeneous graphene samples [260–262]. Under continuous flow, a thin, nearly-stagnant boundary layer of the carrier gas will form above the SiC surface. However, the average thermal speed of the silicon gas is more than $1\,\frac{\mathrm{km}}{\mathrm{s}}$ at the growth temperatures used in these studies. Because the diffusion coefficients are fairly high in this regime as well (at least $10\,\frac{\mathrm{cm}^2}{\mathrm{s}}$), the silicon will rapidly sublimate out of the boundary layer. Entrainment of the silicon vapor in the inert gas may occur at fairly low flow rates and inert gas pressures. It is possible that the exposed surfaces surrounding the SiC are hot enough to reflect a large portion of the silicon vapor back onto the substrate, especially in hot-wall systems similar to UHV-F. Therefore, in continuous gas flow systems the loss of silicon vapor and the concomitant graphitization rate depends on the Fickian diffusivity, the silicon vapor entrainment probability in the inert gas, and the gas flow rate, in complete analogy with the leak rate determined by Fickian and Knudsen diffusion terms associated with stagnant gas systems.

3.4.2 Growth in Silane Gas

Figure 3.9 demonstrates that near-equilibrium growth is suitable for preparing high-quality graphene samples on SiC(0001). Although the carbon face surface morphology is improved in comparison to normal UHV samples [111], it still suffers from significant surface roughening. Increasing the degree of confinement (smaller furnace volume and lower leak rate) is inconvenient for the UHV-F furnace. An additional source of silicon vapor is used instead in order to improve the carbon face. The CCS method of coating the furnace walls with residual silicon is effective but difficult to model as it depends on the furnace history [19]. Silane gas can be used to fill the furnace with a specific quantity of silicon prior to growth. To test this hypothesis, one sample(LF014) was grown in 827 mbar of 0.7% silane/argon mixture (Linde Electronics, DSM Grade) at $1600\,^{\circ}$C for 20 minutes. The silane/argon gas cylinder was attached to the same gas

line used for the pure argon gas experiments (not shown in Figure 2.11).

The surface morphology of this sample characterized via AFM shows smooth terraces separated by step bunches 2 nm high (Fig. 3.10a). The distinguishing topographical features of multilayer EG on SiC($000\bar{1}$) grown at high temperature in CCS furnaces are large step bunches and otherwise atomically smooth terraces [19], interspersed with several nanometer high pleats which run preferentially parallel and perpendicular to the step edges [256, 263]. LF014 shares all of these features, which indicates that the silane gas and residual silicon on the furnace walls impact EG growth on SiC($000\bar{1}$) in similar ways. The orientation of the top 3 4 layers of sample LF014 as determined by LEED (Fig. 3.10b) is dramatically different compared to the samples studied in the previous sections, which were grown in the UHV-F furnace in argon gas (Fig. 3.6). Previous samples possessed graphene diffraction peaks rotated at 0° and 30° with respect to the SiC lattice. LF014 has diffraction peaks at 30° and ±10° with respect to the SiC as well significant diffraction intensity at all other angles. The peaks are azimuthally broader compared to graphene diffraction peaks observed in UHV or argon grown samples. The strong similarity with EG on SiC($000\bar{1}$) samples prepared in a silicon overpressure [6, 19, 264] strongly indicates that the orientation of the first several graphene layers (top layer, downwards) is determined by the initial quantity of additional silicon vapor in the furnace.

It is instructive to compare LF014 to sample LF011, which was grown in a comparable total pressure of argon at a slightly higher temperature of 1650 ° C. The number of graphene layers grown on LF011 was approximately 3 ML as measured by both AES and ellipsometry, while the graphene thickness of LF014 had approximately 6 ML of graphene. Therefore, the average growth rate of LF014 was more than double that of sample LF011, despite the fact that the growth on LF014 occurred at the same overall pressure, a slightly lower temperature, and (most importantly) in the presence of additional silicon vapor from the silane gas. One possible explanation is

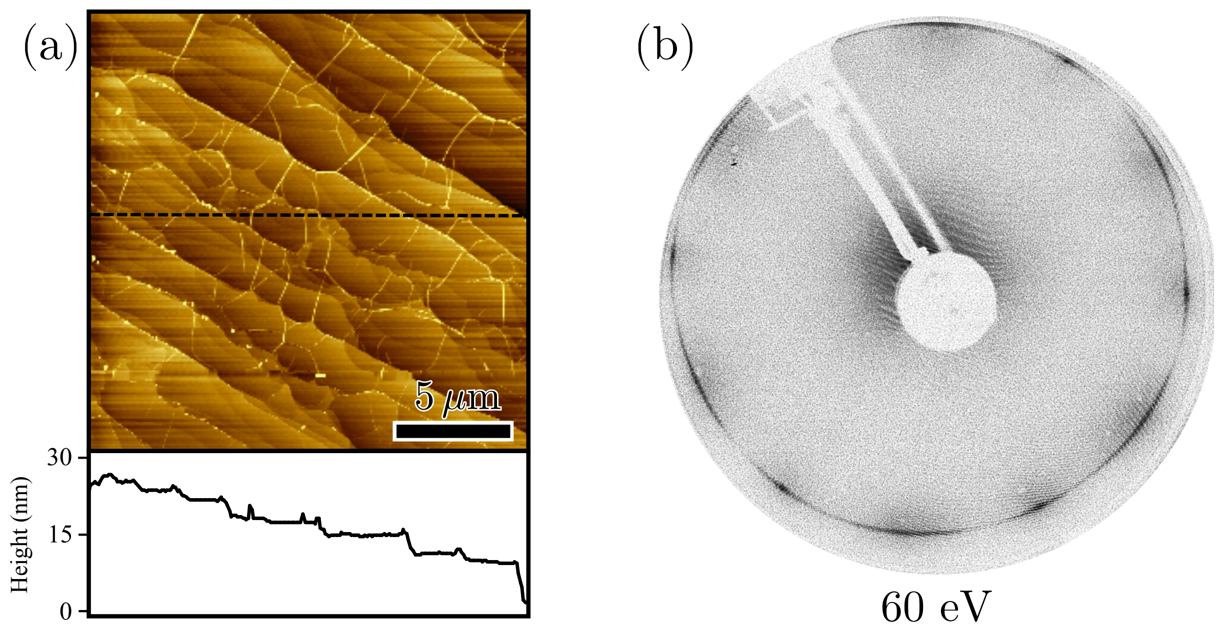

Figure 3.10: AFM and LEED of sample LF014, which was grown in 827 mbar of 0.7% silane/argon mixture. (a) AFM and of the carbon face of sample LF014, which was grown in 827 mbar of 0.7% silane/argon mixture for 20 minutes. The silicon carbide is step bunched (average step height is 2.15 ± 1.01 nm), with $1-3$ nm high pleats in the graphene running across the otherwise smooth terraces with an RMS surface roughness of 0.10 nm. (b) LEED of sample LF014 shows a typical diffraction pattern expected for high-quality multilayer epitaxial graphene grown on SiC$(000\bar{1})$. Compared to samples grown in similar Argon environments (ie. Fig. 3.6), the graphene on LF014 is much thicker (No evidence of SiC diffraction peaks) and contains much more rotational disorder.

that the evaporation coefficient β of the carbon face decreases more slowly with increasingly more graphene layers when the surface morphology is smoother, indicating high mobility of subsurface silicon adatoms. Graphene growth on the silicon face in argon appears to show the opposite behavior in terms of β versus sample roughness, perhaps due to the stable interfacial buffer layer on this surface. At this time, I am unable to authoritatively account for this discrepancy in the SiC($000\bar{1}$) EG growth rate in the presence of silane gas.

3.5 Conclusion

In this chapter I have provided a detailed model based on kinetic rate equations for studying epitaxial graphene growth on SiC in various situations, and have verified the model by comparison with experimental graphene growth rates for samples grown in a CCS style furnace. This model can be used to characterize graphene growth rates in different furnaces, allowing particular growth conditions to be easily duplicated. The model was general form to easily include more chemical reactions and/or physical processes as necessary. I have confirmed that the graphene growth rate in a well-confined hot-wall furnace depends on the total silicon leak rate out of the furnace. I also demonstrated how an inert gas overpressure may be used to decrease the growth rate of epitaxial graphene on SiC in this type of furnace. This type of control is important because the overall growth rate will still depend upon the net conductance of all leaks out of the furnace, as described in my model by the effective diffusivity term D (Eqn. 3.23). The diffusivity is proportional to the cross-sectional area A_c of each leak regardless of the furnace pressure. The furnace geometry is only a coarse control of the graphene growth rate because the dimensions will vary depending upon the design and machining process. The inert gas is a useful fine control of the diffusivity because it is easy to accurately measure the gas pressure prior to growth. Therefore, reasonably high pressure inert gas is useful for carefully tuning the graphene growth

rate in different furnace systems. This method is only useful for reducing the graphene growth rate; however increasing the graphene growth rate is possible by introducing additional furnace leaks or enlarging existing leaks. I have measured values for the enthalpy of sublimation of 6H and 4H SiC, and they are in close agreement with the literature. The initial growth rates for the SiC(0001) and SiC($000\bar{1}$) are essentially the same but begin to diverge as the number of layers increases. The strongly-bonded buffer layer drastically reduces the growth rate on the SiC(0001) surface by kinetically restricting the availability for further SiC sublimation. The reduction in growth rate on the SiC($000\bar{1}$) is much less dramatic and seems to depend on both the growth conditions (silane, argon, or UHV) and perhaps the substrate morphology.

Studying SiC samples graphitized in different furnace pressures and temperatures has revealed how the silicon vapor pressure and sublimation rate impact the substrate morphology. Confined furnace growth in UHV dramatically reduces the surface roughening observed in samples grown in the open geometry, UHV configuration. Samples were grown with similar SiC sublimation rates (as inferred from the average growth rates) over a wide range of furnace pressures and temperatures, and it was shown that the surface morphology consistently improves with higher inert gas pressures. These trends imply that the silicon vapor pressure is the critical factor for improving the surface quality and that the improvement stems from SiC decomposition and EG formation occurring closer to thermodynamic equilibrium. In the open geometry an inert buffer gas is ineffective because the diffusion-sublimation rate remains rapid when vapor transport is not constrained by geometry. Therefore, I expect that graphene growth in an open geometry, UHV configuration will always suffer from significant surface degradation because it necessarily occurs out of equilibrium, unless an additional source of silicon vapor is used to push the system closer to chemical equilibrium.

At temperatures higher than $1500\,^{\circ}$C the surface roughness actually increased on

the SiC(0001) surface because of substrate step bunching, although the graphene covered terraces were atomically smooth. Step bunching was not observed on SiC($000\overline{1}$) until an additional silicon source was introduced in the form of silane gas. Graphene grown on the SiC($000\overline{1}$) in the presence of silane was very similar to the multilayer epitaxial graphene grown by the CCS method, in terms of surface morphology (as measured by AFM) and composition (as measured by LEED and AES). Raman spectroscopy and transport measurements indicated a significant degree of disorder in silane grown SiC($000\overline{1}$) graphene, possibly due to inadvertent hydrogen etching. A detailed examination of the impact of silane on graphitization is beyond the scope of this thesis, but these results have demonstrated how controlling the silicon vapor pressure with an additional source can drastically improve the graphene quality, most likely because the silicon carbide surface is in chemical equilibrium with the vapor from the very beginning of the growth process.

CHAPTER IV

SIDEWALL GRAPHENE NANORIBBONS STUDIED BY SCANNING TUNNELING MICROSCOPY

In most senses, graphene is the ideal channel material for field-effect transistors (FETs). Graphene is a ballistic electrical conductor at room temperature with excellent thermal conductivity. Electronic screening in graphene is very weak, making the material highly susceptible to electrostatic doping in the FET configuration [265]. Unfortunately, intrinsic graphene is a very poor FET channel material because it is not a semiconductor. The lack of a band gap makes it very difficult to turn current OFF in graphene FET devices. The carrier density should be zero for undoped graphene (where the Fermi energy coincides with the Dirac Point), but all graphene FETs exhibit a device dependent minimum conductivity on the order of $(1-4)\frac{e^2}{h}$ at zero doping. The minimum conductivity in graphene has been attributed to the extrinsic disorder in the form of Coulomb impurities in the substrate or oxide and the very weak screening in undoped graphene [49, 52, 266, 267]. The electric field from Coulomb impurities creates a network of electron and hole doped puddles or PN junctions across the graphene surface [268]. These PN junctions do not contribute significantly to the device resistance because of the Klein tunneling effect [47], which is a consequence of pseudospin conservation in graphene [30].

Efforts to engineer a band gap in graphene have generally followed one of three different tactics. It is possible to introduce a band gap into the graphene by chemical modification of the graphene lattice. This technique is attractive because carbon materials can be modified using the large body of techniques from liquid-phase chemistry

[269–273], or reacted with chemically reactive species [274–277]. Chemical modification unfortunately tends to introduce disorder into the graphene crystal lattice which drastically reduces the carrier mobility, although some progress has been made in this direction lately [278, 279].

A more popular alternative for band gap engineering in graphene has been to use quantum confinement. Theoretically, cutting bulk graphene into laterally confined graphene nanoribbons (GNRs) will alter the allowed electronic states in the material [280]. Quantum confinement or the quantum size effect is a consequence of the uncertainty principle, $\Delta x \Delta p_x \geq \frac{\hbar}{2}$, which states that the uncertainty in a particles momentum increases as the position becomes better determined. Reducing the width of a conductive material constrains the positions of electrons laterally, increasing the uncertainty in particle momentum ($\Delta p_x \geq \frac{\hbar}{2\Delta x}$) as well as the minimum kinetic energy of the particle ($E_{min} = \langle p_x c \rangle = \Delta p_x c$ for Dirac particles). Confinement also increases the energy gap between allowed electron states in analogy with the particle-in-a-box problem:

$$E_n = p_n c = \hbar k c = \hbar c \frac{\pi}{L} n \tag{4.1}$$

where Equation 4.1 is valid for a Dirac particle in a 1D box of width L, and $n = 0, 1, 2 \ldots$ is the state index. The energy gap in a 1D box is inversely proportional to the box width: $E_g/n = E_n/(n) = hc/2L$. Therefore, if quantum confinement can generate a gap in GNRs the size of the gap would be inversely proportional to the width of the ribbon.

However, theory predicts that the band structure of perfect GNRs is extremely sensitive to nanoribbon edge termination. Graphene supports three different types of edges: zig-zag (Fig. 4.1a), armchair (Fig. 4.1b), and chiral (a periodic mixture of zig-zag and armchair edges, Fig. 4.1a). Armchair nanoribbons are predicted to be metallic when the width is $N = 3M - 1$, where N is the width of the ribbon in terms

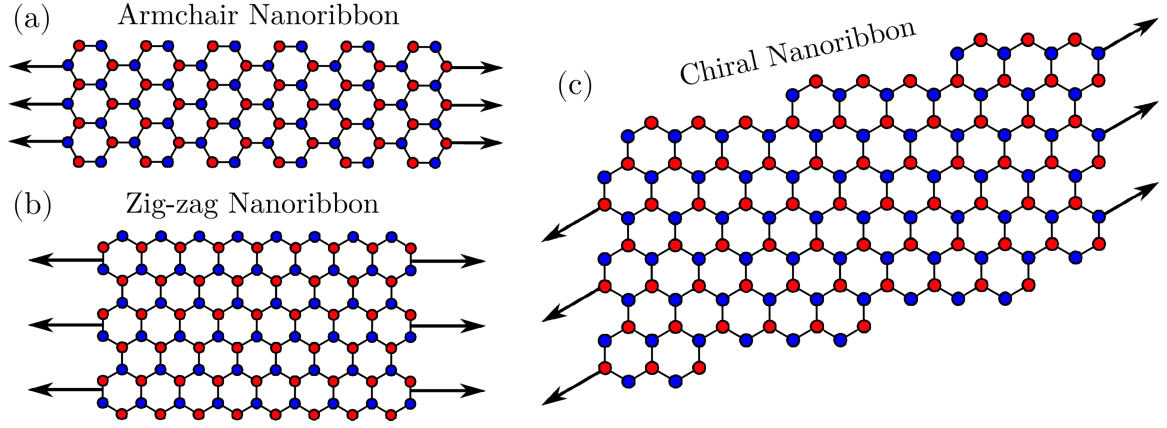

Figure 4.1: Graphene nanoribbons are formed by cutting a graphene sheet into narrow strips. In general there exist three different classes of ideal nanoribbons (a-c) as defined by the orientation of the ribbon with respect to the graphene crystal lattice. (a) Zig-zag nanoribbons have have edge-terminated atoms belonging to a single carbon sublattice, while (b) armchair ribbons have atoms from both sublattices at the edge. Another possibility is to have a periodic arrangement of zig-zag and armchair edge sites, called (c) chiral nanoribbons.

of the number of carbon atoms in one sublattice and M is an integer, but otherwise they are predicted to be semiconducting with narrower ribbons possessing a wider band gap as expected [280]. Zig-zag nanoribbons are metallic because of a flat band at $E = 0$ that consists of a massless Dirac fermionic wave function localized at zig-zag graphene and graphite edges, which decays exponentially into the middle of the ribbon [281]. This so-called 'edge-state' is a consequence of the fact that the atoms along a zig-zag edge all belong to a single carbon sublattice, or more appropriately because the projection of the 2D band structure maintains the distinctness of each Dirac cone at $\mathbf{K}$ and $\mathbf{K}'$ [282]. Every chiral nanoribbon also supports an edge-state along the zig-zag components of the edge, with the spectral density of the edge-state almost linearly proportional the fraction of zig-zag to armchair edge sites [283]. Therefore, according to the non-interacting tight-binding approximation only 2/3 of all uniform width armchair nanoribbons gain an energy band gap through quantum confinement, and the rest of all nanoribbons are metallic. However, including electron-electron interactions can spontaneously open a band gap through magnetic ordering along

and across the nanoribbon [282]. It has also been predicted that passivating the dangling bonds at the GNR can open a band gap in the electronic structure of the material, including both zig-zag and chiral ribbons [284].

Given the large parameter space and the several possibilities regarding the theoretical band structure of a GNR with a particular edge orientation, it is clear that a systematic study of the electronic properties of this material is warranted. GNRs have been fabricated by various groups using standard lithographic etching techniques to cut nanostructure from larger sheets of graphene. Although early results indicated large energy gaps that scaled roughly with the inverse of the ribbon width [285], it was later determined that the observed gaps in patterned GNRs was the result of charge localization along the ribbon length because of lithography-induced edge roughness [286]. Edge roughness on the scale of several graphene unit-cells act as randomly placed short-range scattering defects which strongly backscatter charge carriers [287], resulting in Anderson localization and conduction gaps near the Dirac point in rough GNRs [288, 289]. In the high edge disorder limit nanoconstrictions along the GNR form a series of interconnected quantum dot states [290]. For very narrow ribbons (less than 10 nm wide) even very little edge disorder can incite Anderson localization and a transport gap [287]. In general, the edge roughness is an unavoidable consequence of the masking/etching lithography process. Some progress has been made to combat the edge roughness incurred during GNR lithography [291, 292]. A different technique involves 'un-zipping' carbon nanotubes into GNRs with very smooth edges [293, 294]. These ultra-smooth nanoribbons are ballistic conductors with carrier mobilities as high as 3200 $\frac{\mathrm{cm}^2}{\mathrm{V \cdot s}}$ (comparable to 'dirty', intrinsic graphene on SiO_2) [295]. Sub-10 nm ultra-smooth nanoribbons were found to be both ballistic and metallic, which may be a consequence of the edge state associated with zig-zag and chiral graphene edges [280–283, 296]. Low-temperature STM was performed on these ultra-smooth nanoribbons to study edge and electronic structure [297]. Only zig-zag or

chiral nanoribbons were located in this study, and scanning tunneling spectroscopy (STS) measurement of sub-20 nm ultra-smooth nanoribbons revealed a small width-dependent gap (~ 50 meV for a nanoribbon that was 8 nm wide) [297]. Although the ultra-smooth GNRs are promising materials, they suffer from the same drawbacks as carbon nanotubes in terms of controlling ribbon type and placement onto a substrate.

Controlled, epitaxial GNR growth on an insulating substrate is possible with SiC(0001) (silicon face or silicon termination) [119]. As discussed in Chapter 3, epitaxial graphene growth on SiC is driven by the imbalance in vapor pressure between Si and C. At temperatures less than $1800\,^{\circ}$C essentially only monoatomic silicon is sublimated from SiC [105], leaving the residual carbon adatoms behind to form graphene. The first layer of graphene grown on SiC(0001) is covalently bonded to the substrate, which changes the semi-metallic graphene into a wide-band gap or insulating phase known as the 'buffer layer' or 'layer-0.' Further carbon layers are grown beneath the initial buffer layer, converting the initial buffer layer into a layer of graphene and forming a new buffer layer at the interface with the SiC [5]. Graphene growth on SiC(0001) tends to begin at substrate step edges as determined by the common observation of thicker graphene films adjacent to steps compared to the remainder of the SiC terrace [110, 260]. The nucleation of graphene at step edges is sensible because the Si atoms on the steps have more dangling bonds and are less stable compared to silicon on the basal plane, so the local silicon vapor pressure near SiC steps should be greater than the average silicon vapor pressure of the entire surface. In order to minimize the surface energy, unit-cell or higher SiC steps can redistribute into high-index nanofacets during annealing in vacuum or in a reducing atmosphere [102, 298–302]. The crystalline orientation of the facet depends on a variety of parameters such as step height, surface miscut angle/orientation, annealing temperature/time, and the surface termination (Si or C face) [303, 304]. Graphene has been shown to grow rapidly on low-angle SiC facets or 'sidewalls' compared to

the growth rate on SiC(0001) terraces [304]. This 'sidewall graphene' does not appear to interact or to covalently bond with the SiC facet [301, 302], which should preserve the electronic properties associated with graphene. Therefore, combining preferential graphene growth on SiC facets with the ability to control the graphitization rate on SiC by restricting silicon sublimation (See Ch. 3) enables the fabrication of GNRs located on SiC nanofacets, separated from one another by the insulating buffer layer on the SiC terraces.

The main advantage of this technique is that the GNR width is controlled by the initial height of the SiC steps, and it is possible to control the vertical etching rate of SiC with nanometer scale precision using reactive ion etching. Conceivably, the edge roughness of the sidewall GNRs should be minor compared to lithographically patterned ribbons. Lithography of bulk graphene is limited by the resolution/smoothness of the etch mask and the lateral uniformity of the graphene etching process. Edge disorder of sidewall GNRs should (assuming that the graphene growth is limited to the nanofacet itself) be determined by the atomic-scale roughness of the SiC nanofacets and sidewalls. Furthermore, there is evidence that the graphene on the sidewalls largely maintains the epitaxial relationship with the SiC(0001) surface, because the sidewall graphene covalently bonds with the epitaxial graphene buffer layer that resides on the SiC terraces [301]. This epitaxial relationship then couples the edge orientation of the GNR to the SiC crystal axes, such that controlling the orientation of the SiC steps defined by lithography is equivalent to controlling the edge orientation of the resulting GNRs.

Graphene grown on the sidewall facets of SiC(0001) appears to be the ideal method for creating a semiconductor material that retains the electronic properties of graphene. However, the transport measurements of these GNRs lack any evidence of edge disorder-related transport *or* a simple band gap, regardless of nanoribbon edge orientation or width [305]. These nanoribbons demonstrate room-temperature

ballistic conduction, with ballistic mean free paths as high as $15\,\mu$m. The average conductance of these ballistic nanoribbons is approximately $\sigma_0 = \frac{e^2}{h}$, indicating that the transport is dominated by a single, nondegenerate quantum channel. Ballistic transport by a single quantum channel was expected in zig-zag and chiral nanoribbons, but it was also predicted that the channel would be spin-degenerate ($\sigma_0 = \frac{2e^2}{h}$) [296]. In addition, a recent ARPES study found that the *overgrown* sidewall GNRs (i.e. where graphene is continuous from the sidewall onto the terrace) form a semiconducting region in between the metallic terrace and sidewall graphene. Clearly, there are a great number of unanswered questions regarding sidewall GNRs that will help us understand these previous experiments. Scanning tunneling microscopy (STM) is an excellent tool for this kind of investigation, because it allows one to study both the morphology and the electronic structure of the nanoribbons simultaneously. Furthermore, some questions concerning sidewall GNRs can only be answered using a local, scanning probe technique like STM.

4.1 Types of Sidewall Graphene Nanoribbons

Sidewall GNR samples were grown using confinement-controlled sublimation (CCS) in a custom built low-vacuum furnace [19]. The furnace used to grow these samples is shown in Figure 4.2. Two different sidewall GNR samples were studied for this project. The first type of self-organized sidewall nanoribbon (sample 25Ed30) was grown directly on a nominally on-axis, conductive ($0.015 - 0.028$ Ω-cm) 4H SiC(0001) substrate by annealing in a custom single-user CCS furnace (Fig. 4.2a) at $1500\,^\circ$C for 9 minutes. The 4H SiC(0001) wafer was miscut toward the $[1\bar{1}00]$ crystal direction with an angle less than $0.1\,^\circ$C. Characteristic Atomic-Force Microscopy (AFM) and Electrostatic Force Microscopy (EFM) performed on sample 25Ed30 following growth is shown in Figure 4.3. The AFM images reveal that the surface formed giant step bunches during the growth process, which is typical for high-quality CCS growth

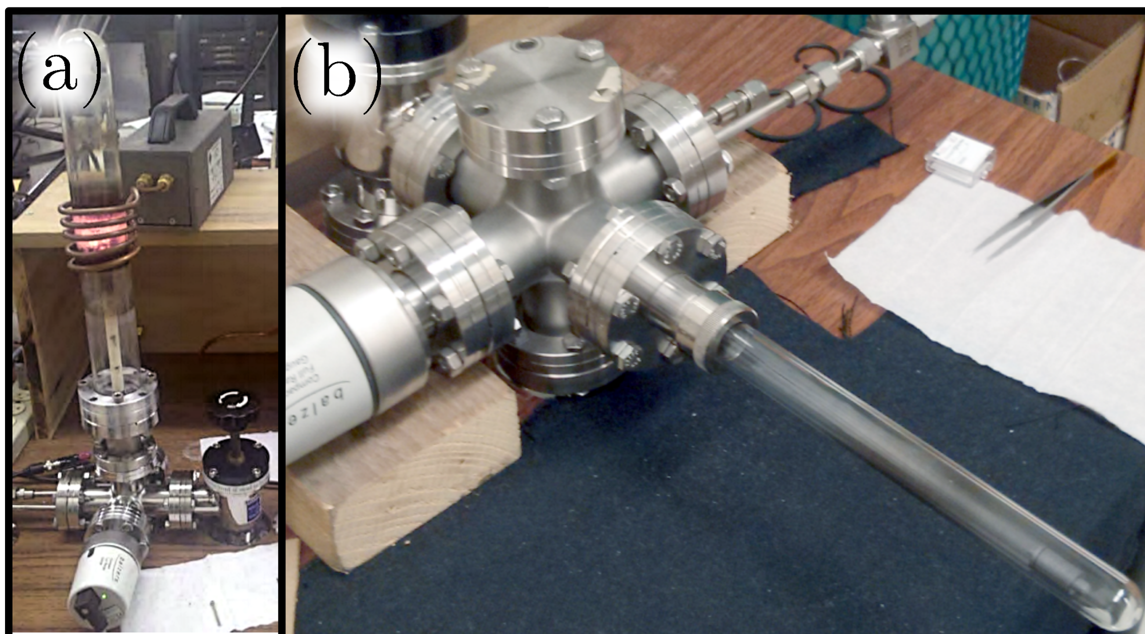

Figure 4.2: Images of the low-vacuum CCS furnaces used to grow sidewall GNRs on SiC(0001) in this study.

on the SiC(0001) surface [19, 110, 260]. EFM acquired simultaneously with AFM (Fig. 4.3b) clearly show that the surface capacitance changes significantly along the SiC sidewall. The capacitance change is attributed to the GNR on the SiC sidewall, where the change occurs because the local work function of graphene ($\sim 4.6\,\mathrm{eV}$) [306] is different from SiC ($\sim 4.8\,\mathrm{eV}$) [307].

Unfortunately, the simultaneous formation of step-flow induced step bunches and GNRs was difficult to repeat experimentally. To improve the likelihood of self-organized GNR formation, step bunches were pre-formed on separate dimple ground vicinal samples by dry etching in 1 atm of hydrogen at $1800\,^{\circ}\mathrm{C}$ [116, 300]. The dimple ground sample (HDS009) was prepared using initially on-axis, conductive ($0.015 - 0.028$ Ω-cm) 6H SiC(0001) (More information regarding dimple grinding and intentional step bunching by high-temperature hydrogen etching is available in sections 2.1.3 and 2.1.2, respectively). The step bunches formed in this manner were relatively straight (given the curvature of the vicinal surface) and well-ordered as

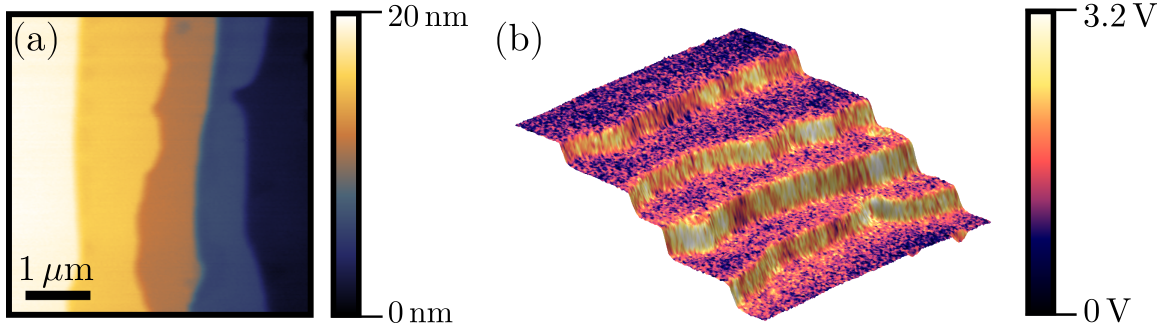

Figure 4.3: AFM and EFM measurements of sample 25Ed30 (on-axis GNR) after graphitization. (a) AFM shows that step bunching has occurred across the surface, which an average step height of 4 nm in this region. (b) a 3D representation of the sample in (a) with the EFM data as on overlay. The surface potential on the SiC sidewall nanofacets changes by approximately 2 V relative to the SiC terraces, indicating the presence of sidewall GNRs.

determined by optical microscopy (Fig. 2.8), atomic force microscopy, and scanning electron microscopy (Fig. 2.9). The height of the step bunches varied smoothly between $5 - 30$ nm as a function of the local miscut angle in the dimple. Sidewall GNRs were subsequently formed on the hydrogen etching induced step bunches by annealing in a custom multiple-user CCS furnace (Fig. 4.2b) at 1565 °C for a total of 1 minute. AFM/EFM and Raman spectroscopy performed post-growth provides evidence of GNR growth on the sidewalls of SiC (not shown).

4.2 Methods

Sample 25Ed30 was stored in air for one month before being transferred into the RT-UHV system. The sample was outgassed in vacuum at a minimum of 300 °C using an electron beam heater (section 2.2). Low-energy electron diffraction (LEED) and Auger electron spectroscopy (AES) were performed in-situ (section 2.3.1) following sample heating. STM measurements were performed in ultra-high vacuum using the room temperature STM described in section 2.3.2.2. Tungsten tips were electron-beam annealed and characterized by Field-Emission Microscopy prior to STM experiments.

4.3 Results

4.3.1 SiC Sidewall Nanofacet Structure

LEED was performed on 25Ed30 several hours after transfer into vacuum. The diffraction pattern was very weak and there was a bright, diffuse background intensity characteristic of surface contamination. The LEED patterns improved substantially after flash heating to 850 ° C, 1100 ° C, and finally 1450 ° C for 2 minutes each. Although the diffraction peaks sharpened and the diffusive background decreased after the annealing regimen, the spot sizes were fairly large and the $(6\sqrt{3} \times 6\sqrt{3})R30^{\circ}$ reconstruction pattern was weak compared to UHV grown epitaxial graphene on SiC(0001) (Fig. 4.4a). Sample HDS009 was transferred into vacuum within one hour of growth to keep surface contamination to a minimum. The initial LEED pattern displayed sharp, bright diffraction peaks and a very weak diffuse background. Heating sample HDS009 up to 850 ° C further improved the quality of the diffraction pattern (Fig. 4.4b), which was more comparable to UHV grown graphene and substantially more ordered compared to sample 25Ed30. Directly prior to an STM experiment sample HDS009 was briefly reheated to 850 ° C, and was not heated higher than 850 ° C.

LEED patterns shown in Figure 4.4 appear almost indistinguishable from LEED patterns on SiC(0001) surfaces covered predominantly with buffer layer graphene after graphitization in the UHV-F furnace (Fig. 3.5). The diffraction patterns are similar to those observed for buffer layer samples grown ex-situ in other CCS furnaces (not shown). Because the epitaxial relationship between the buffer layer and the SiC is maintained and the sidewall GNRs are expected to be sp^2−bonded with the buffer layer [301, 302], we can assume that if the GNR is well-ordered it will have a zig-zag edge orientation for steps running perpendicular to the $\langle 1100 \rangle$ directions. The presence of the $(6\sqrt{3} \times 6\sqrt{3})R30^{\circ}$ diffraction pattern conclusively demonstrates that the SiC(0001) terraces are covered by at least bare buffer layer or layer-0 graphene

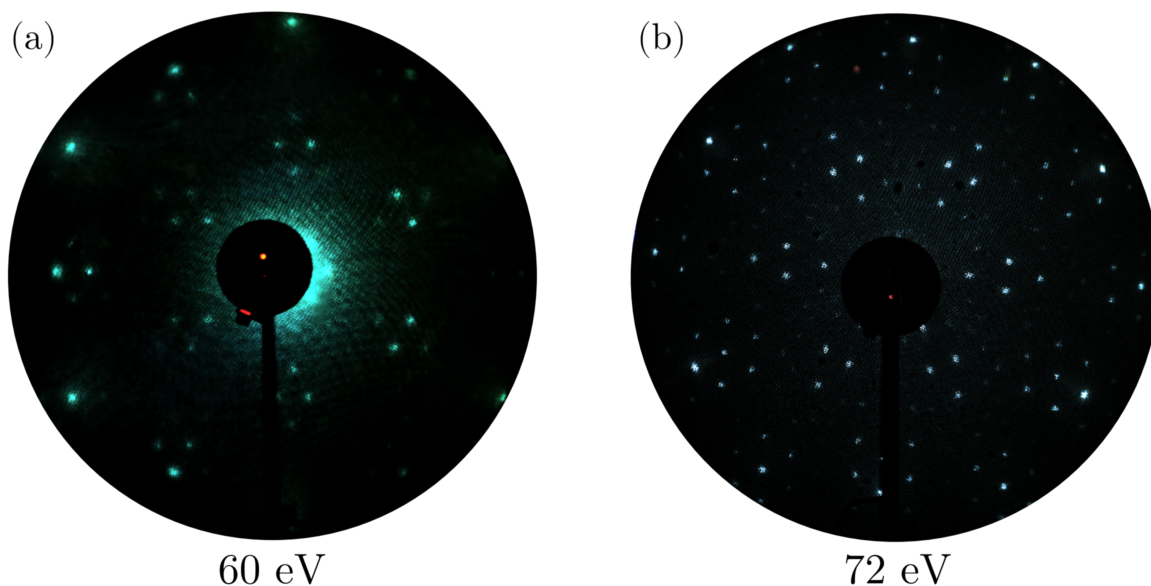

Figure 4.4: LEED on samples (a) 25Ed30 (on-axis GNR) and (b) HDS009 (dimpled GNR), after outgassing as described in the text. Both LEED patterns are consistent with a buffer layer covered SiC(0001) surface, although the dimpled GNR sample is much more ordered than the on-axis sample.

[239]. The graphene and SiC diffraction peaks have approximately the same magnitude at an electron energy of 106 eV corresponding to the Bragg diffraction peak of SiC. The unity ratio between the graphene and SiC diffraction peaks at 106 eV was associated with predominantly buffer layer on the SiC(0001) surface as confirmed by Auger electron spectroscopy in Chapter 3.

AES was used to measure the graphene film thickness on samples 25Ed30 and HDS009 based upon the relative attenuation of the Si Auger electron intensity versus the C Auger electron intensity. The graphene film thickness was calculated exactly as described in section 3.2. Briefly, the model assumes that the buffer layer, the first graphene layer grown on SiC(0001), is structurally equivalent to ideal graphene. Auger signal attenuation measurements on both samples were consistent with one graphene layer (i.e. buffer layer) on SiC(0001).

Figure 4.5a shows a large-scale STM image of a self-organized sidewall GNR on a nominally on-axis SiC(0001) surface (sample 25Ed30). The step is very straight over

the approximately 500 nm range of the STM. It is clear even from this large scale image that the step has relaxed into a high index nanofacet as confirmed by the higher resolution STM images in Figure 4.6. The SiC sidewall and small regions near the top and bottom of the sidewall are up to one order of magnitude smoother than the majority of the SiC surface. Based upon the EFM (Fig. 4.3) and Raman Spectroscopy measurements (not shown), it is reasonable to associate the smooth features on the SiC sidewalls with the presence of graphene. However, the EFM measurements only show a clear work function change on the SiC sidewalls (Fig. 4.3b), whereas the STM measurements almost always show that the graphene on the sidewalls grows continuously onto the terraces of the SiC. The majority of these measurements find that sidewall GNR overgrowth favors the top terrace over the bottom one (as previously predicted) [308]. The same general features are evident for GNRs grown on the dimpled SiC (sample HDS009), although in general these sidewalls have more variability in structure (Fig. 4.5b).

The SiC sidewalls on both the on-axis and dimpled samples relaxed into lower energy nanofacets. The angle of the SiC sidewall with respect to the surface normal defines the crystallographic plane of the nanofacet. For instance, the sidewall angle in Figure 4.6a is $\sim 28^{\circ}$ with respect to the surface normal. This angle corresponds to the SiC($1\bar{1}07$) facet, which was also observed in patterned SiC sidewalls with edges

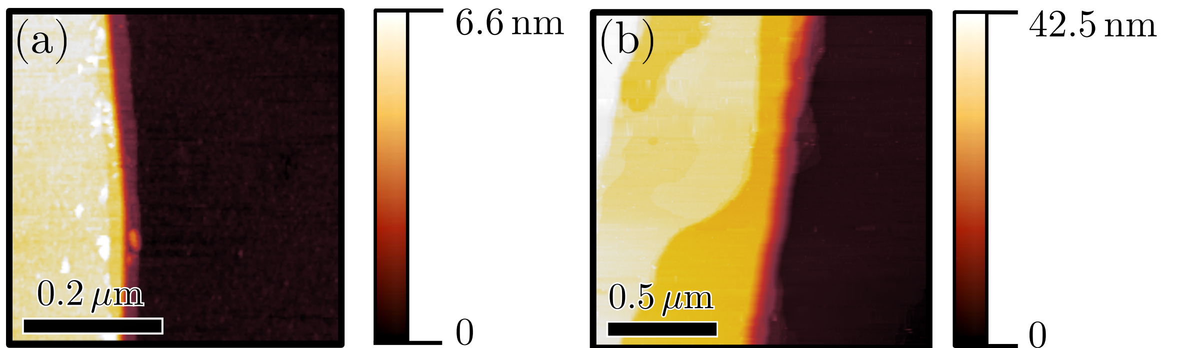

Figure 4.5: Large-scale STM images of GNR covered sidewalls nanofacets on (a) on-axis (25Ed30) and (b) dimpled SiC (HDS009).

perpendicular to the $[1\bar{1}00]$ crystal plane [119]. Upon closer inspection the profile of the sidewall consists of two separate $\sim 32\,^{\circ}$ nanofacets corresponding to a SiC($1\bar{1}06$) nanofacets separated by a nearly flat, narrow region (see inset of Fig. 4.6a). Since the region separating the two nanofacets in Figure 4.6a is so narrow that it is attractive to consider this feature as the merger between two separate step bunches, or perhaps as the incomplete relaxation of a single step bunch. It is also common to observe step bunches that are more completely distinguished by multiple nanofacets. The graphene is continuous across the entire step bunch in Figure 4.6b, but here the sidewall has split into two distinct SiC($1\bar{1}07$) ($\sim 28\,^{\circ}$) nanofacets [308]. In general, the facet angle for single step sidewalls was greater than the facet angle for multiple step sidewalls. There exists a narrow, nearly flat flat region near the top of these two nanofacets as well (see insert of Fig. 4.6b). Including this narrow region the average facet angle across both sidewall nanofacets is $\sim 25\,^{\circ}$, corresponding to the SiC($1\bar{1}08$) facet. The SiC($1\bar{1}08$) was the most common facet observed on sample 25Ed30, and was determined to be the most common facet observed for patterned SiC sidewall in a separate study [119].

The nanofacets formed on the dimpled SiC sample depend strongly upon the original step bunch height, as well as the formation of of multiple or single nanofacets per step bunch. The STM scan in Figure 4.7a was acquired near the rim of the dimple,

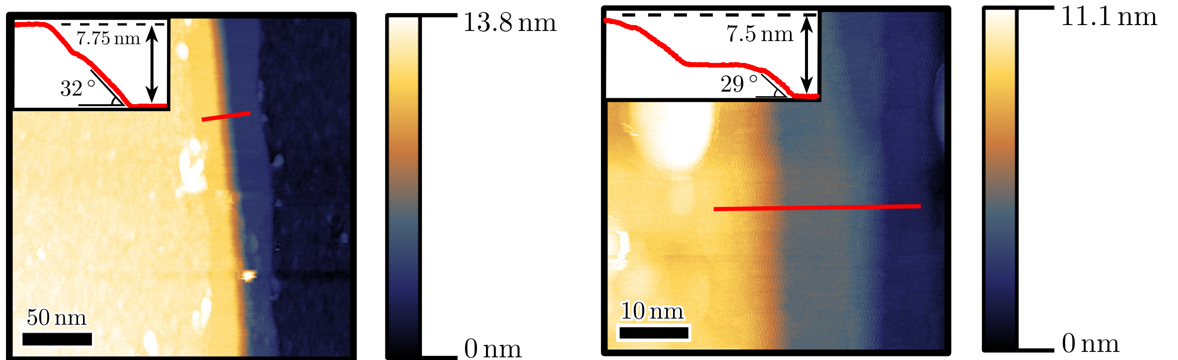

Figure 4.6: Detailed STM images of sidewall nanofacets on on-axis SiC (25Ed30)

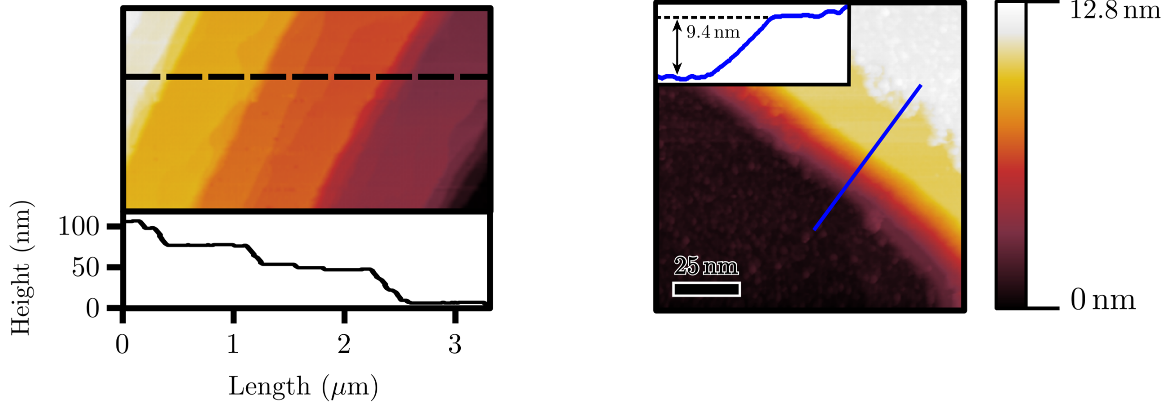

Figure 4.7: Detailed STM images of sidewall nanofacets on dimpled SiC (HDS009)

where the vicinal angle approached 4° and well-organized bunches of 30-nm steps were present before graphitzation as determined by SEM and AFM. The sidewalls in Figure 4.7a have become disordered after GNR growth, with sidewall heights ranging from 20 nm to 40 nm. These step bunches have very shallow nanofacet angles between 11° and 12°, corresponding to either SiC($1\bar{1}0\,19$) or SiC($1\bar{1}0\,18$). Figure 4.7b shows a more ordered sidewall GNR closer to the center of the dimple, with a step height of 10 nm. However, upon closer inspection this sidewall consists of closely spaced, multiple nanofacets similar to what was observed in Figure 4.6 for the on-axis SiC sample. In this case the lower nanofacet is $\sim 18°$ [SiC($1\bar{1}0\,12$)], which transitions to a $\sim 22°$ nanofacet [SiC($1\bar{1}09$)] near the top of the sidewall.

4.3.2 Atomic-scale structure of sidewall graphene nanoribbons

Atomic-scale imaging and graphene is complicated by the fact that this material has a very small lattice constant of only 2.46 Å which requires an extremely small STM tip radius in order to image. STM tips with a small radius of curvature are notoriously unstable, which is further complicated by the already troublesome tunneling characteristics of the buffer layer on these samples. Nevertheless, the atomic-scale resolution of the GNRs was achieved in several locations on both the on-axis and dimpled samples.

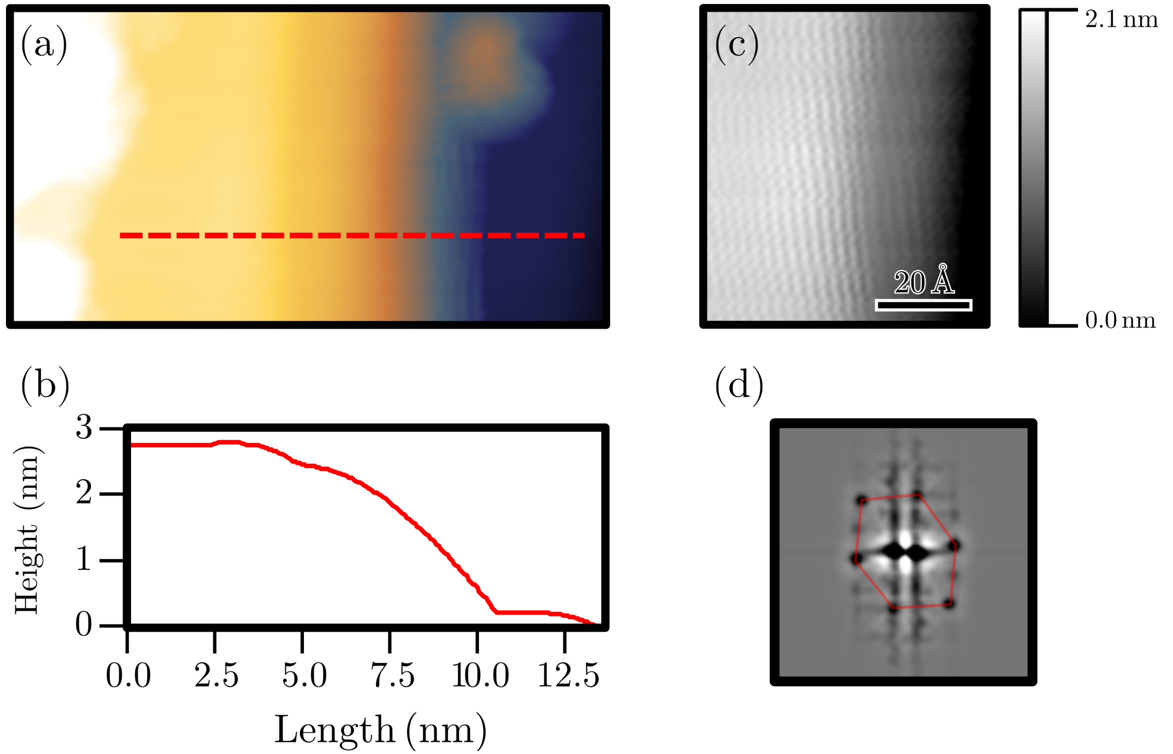

Figure 4.8: (a) STM image ($V_B = 1.0\,V$, $I_t = 50\,pA$) of the top portion of a multiple nanofacet step bunch on the on-axis sample. (b) The entire step bunch is $\sim 10\,nm$ high, but only the top 3 nm as shown in the profile. (c) Carefully subtracting the background height variation from the SiC substrate reveals the atomic lattice of sidewall GNR on both the terrace and the nanofacet. The atomic lattice was made prominent and added back to the background to demonstrate that the graphene lattice is continuous onto the SiC nanofacet (local height enhancement). This image is local height enhanced to display both the atomic lattice and SiC sidewall. Near the sidewall the graphene lattice bulges upward $\sim 1\,\text{Å}$ and the graphene lattice is distorted relative to the imaging on the terrace, as shown in (d) the FFT power spectrum of the atomic lattice, where white/black is low/high power.

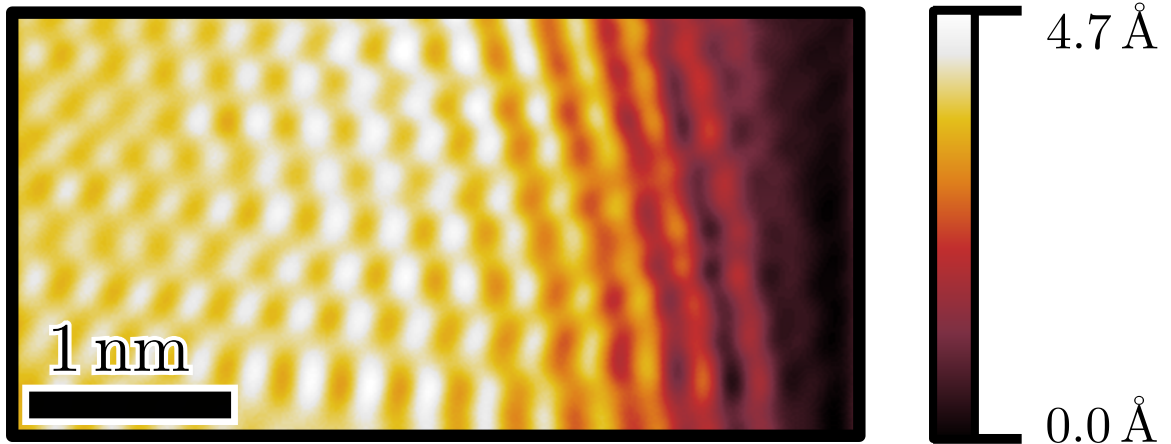

Figure 4.9: Higher resolution STM image ($V_B = 0.7\,V$, $I_t = 50\,pA$) of the top portion of the sidewall GNR shown in Figure 4.8. The profile across the middle of image shows that the graphene gradually bulges upward 3 Å over $\sim 3\,nm$ before proceeding onto the SiC sidewall nanofacet. The asymmetric sublattice imaging is strongest in the middle of the bulge, where the graphene lattice is most distorted.

Figure 4.8 is an STM image of the graphene lattice acquired near the top of a multifaceted, 10 nm SiC step bunch on sample 25Ed30. The GNR zig-zag edge is oriented almost parallel to the step edge as expected from LEED. The physical edge of every GNR is obscured by large debris (cf. Figs. 4.6 and 4.7). The graphene lattice appears well-ordered without any significant defects, although there is some distortion of the lattice. The higher resolution STM image in Figure 4.9 shows the graphene as it transitions from the overgrown basal plane onto the sidewall nanofacet. Near the curved portion of the GNR where the graphene begins to transition onto the SiC sidewall, the lateral lattice constant appears to expand and the carbon sublattice imaging becomes asymmetric, which is often associated with broken inversion symmetry of the graphene lattice. According to the height profile in Figure 4.8 this region corresponds to a slight upward bulge in the GNR. Once the GNR has settled onto the SiC sidewall the lattice constant returns to normal and symmetric sublattice imaging resumes. According to the FFT of the STM image shown in Figure 4.8d, The atomic lattice appears to have both uniaxial compressive strain roughly perpendicular to the step ($\sim$ 10%) and a slight amount of shear strain. Weaker peaks may be attributed

to the distortion of the lattice over the bulge, which changes the apparent direction of the lattice. Interestingly, these peaks appear to have very little compressive strain with the shear strain remaining, indicating that the upward bulge in the image allows the lattice to partially relax.

The atomic lattice of a GNR on the dimpled SiC sample is displayed in Figures 4.10 and 4.11. These images were acquired on the top part of the same SiC sidewall shown in Figure 4.7b. The graphene lattice is imaged on both the basal plane and the nanofacet of the SiC. Unlike the graphene on the on-axis sample, the graphene on the dimpled sample does not bulge upwards near the step edge. Instead it abruptly curves over the step edge (Fig. 4.10b), which results in what appears to be a $(\sqrt{3}\times\sqrt{3})R30^{\circ}$ electronic scattering pattern in the curved region. The most striking feature on the basal plane is the presence of a strong, long wavelength hexagonal pattern alongside the graphene lattice. The graphene only appears to image in the 'dark' regions of the hexagonal pattern, which abruptly ends at the step edge. These features are more clear in the background subtracted version of this image in Figure 4.11a. Figure 4.11b shows the 2D FFT of the background subtracted image. The FFT shows a complicated set of reciprocal-space peaks. The circled outer peaks are attributed to the graphene lattice. According to the FFT calibration the graphene lattice nearly uniformly compressively strains by $\sim 12\,\%$.

Figure 4.12a shows a larger scale STM scan acquired in the same region at a higher sample bias where only the long wavelength, hexagonal pattern is imaged. The scan was background subtracted to remove the change in height from the SiC sidewall nanofacet. The long wavelength pattern is almost identical to the $(6\sqrt{3}\times 6\sqrt{3})R30^{\circ}$ graphene buffer layer grown on SiC(0001) in UHV [210, 309], as shown in Figure 4.12b. The preferential imaging of the graphene lattice in some regions and the larger-scale buffer layer reconstruction elsewhere was previously observed (see Figure 6.1 in reference [132]). In STM the $(6\sqrt{3}\times 6\sqrt{3})R30^{\circ}$ images as a 6×6 corrugation with

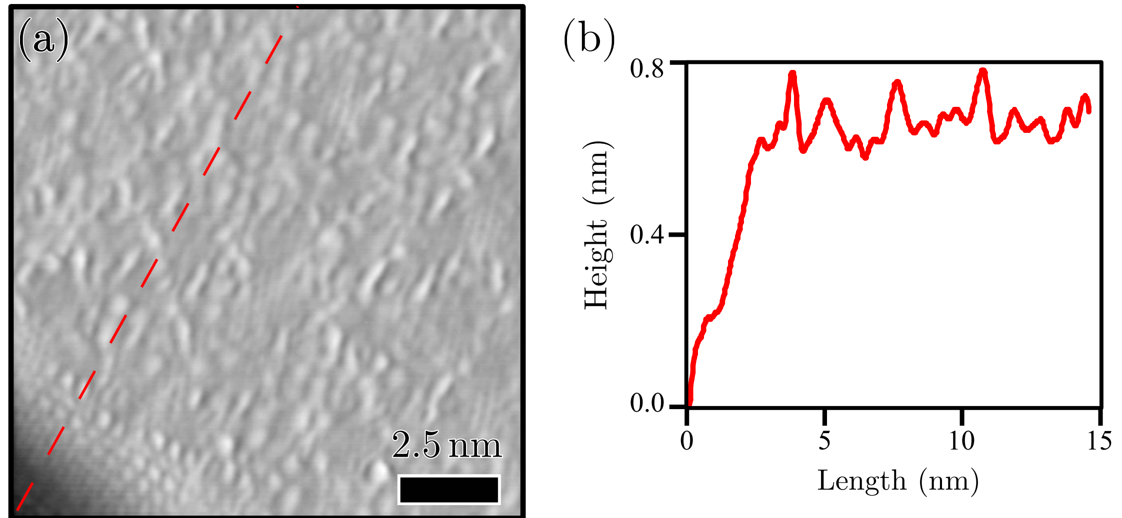

Figure 4.10: (a) Atomic sale resolution STM image (V_B = -0.6 V, I_t = 30 pA) of the GNR on the dimpled SiC sample (HDS009), on the same SiC sidewall shown in Figure 4.7b. The graphene lattice is continuous across the basal plane and SiC nanofacet, and what may be a $(\sqrt{3} \times \sqrt{3})$R30° electronic scattering pattern is present in the transitionary region where the graphene abruptly curves over the edge. The atomic scale information was local height enhanced to simultaneously display the graphene lattice and the large-scale features of the SiC sidewall. (b) Profile of the local height enhanced image along the dashed line in (a).

respect to the SiC lattice constant (a = 3.08 Å) which is visible beneath overlying graphene layers at higher bias [239]. For instance, Figure 4.12b shows a region of

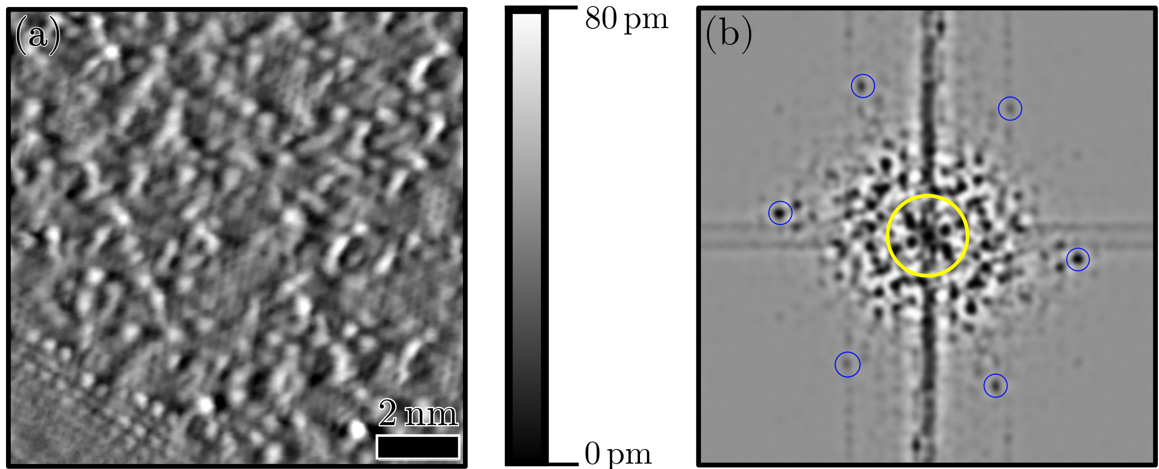

Figure 4.11: (a) Background subtracted image of Figure 4.10, and (b) 2D Fast-Fourier Transform (FFT) of the background subtracted image. The peaks attributed to graphene lattice are highlighted by the outer circles. The graphene lattice constant is uniformly compressively strained by ∼ 12 %.

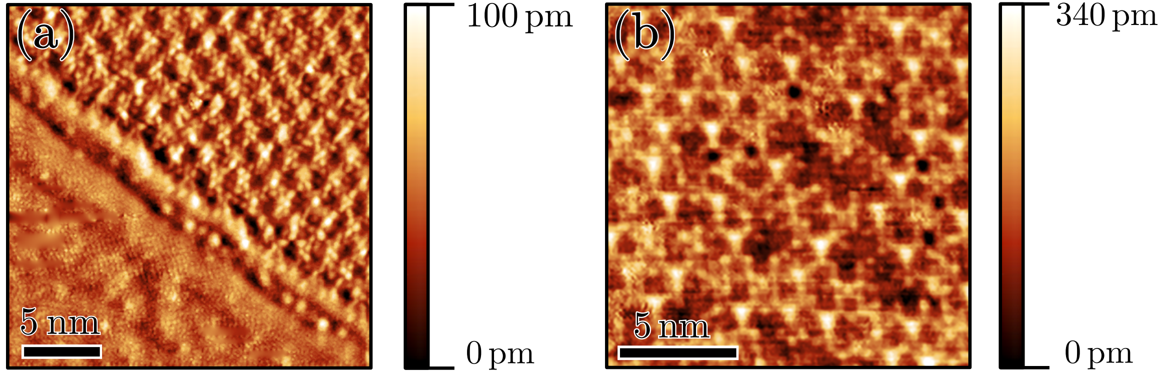

Figure 4.12: (a) (V_B = -1.5 V, I_t = 30 pA) STM image (V_B = 1 V, I_t = 100 pA) of the graphene (layer-1) on top of the graphene buffer layer (layer-0) on SiC(0001) . At this voltage bias the LDOS of the buffer layer is much greater than the LDOS of the graphene overlayer, so the buffer layer dominates the tunneling current and the constant height image. The buffer layer lattice is constant is uniformly compressively strained by $\sim$ 12 % as determined by FFT (not shown). The sample in (b) was grown in UHV by thermal annealing with an electron beam heater (section 2.2)

layer-1 graphene where only the SiC orbitals are evident at a sample bias of 1 V. The long wavelength hexagonal pattern in Fig. 4.12b has an average lattice constant of 16.14 Å, which, assuming a 6×6 corrugation, corresponds to 2.69 Å for the SiC lattice. Although strained, the reconstruction is hexagonal and rotated by 30 ° with respect to the graphene lattice, and has approximately the same amount of compressive strain found in the graphene lattice imaged in Figure 4.11. The buffer layer imaged lacks some of the obvious 'tetramer' or 'hexagon' features which are commonly observed for the UHV grown buffer layer [239]. The apparent height corrugation of the buffer layer graphene in Figure 4.12a and the sublattice symmetry of graphene lattice imaged in Figure 4.11 indicates that the basal plane portion of the GNR is one layer thick (layer-1).

As shown in Figures 4.6 and 4.8 the GNRs on the on-axis sample do not show a 6×6 reconstruction. It was previously demonstrated that the amplitude of the 6×6 corrugations decreases rapidly with the number of graphene layers present [134]. Based upon these results it seems that the overgrown, basal plane portion of the GNRs are multilayered on the on-axis sample and single-layer (i.e. layer-1

graphene) on the dimpled sample. The thickness of the sidewall portion of each GNR is much more difficult to ascertain by STM. However, cross-sectional transmission electron microscopy of graphitized SiC(0001) step bunches clearly demonstrates that many more graphene layers are present on the sidewall nanofacets even when the SiC(0001) surface is only covered by buffer layer or monolayer graphene [301, 302]. Few-layer graphene on SiC(0001) is Bernal stacked which induces an asymmetric sublattice imaging from the broken sublattice inversion symmetry [132]. Strangely, the asymmetric sublattice imaging occurs predominantly near the step edge where the graphene appears to bulge upwards but is absent for the graphene resting on the basal plane of SiC(0001). One possibility is that these features appear because there is a significant amount of strain in the GNR, and possibly different amounts of strain in each graphene layer. The presence of strain in GNRs on SiC(0001) can be thought of as a consequence of the different thermal expansion coefficients of SiC and graphene. The thermal expansion coefficient of SiC is positive which implies that the material expands with rising temperature. Conversely, graphene has a negative thermal expansion coefficient which implies that it will actually contract with rising temperature. For complete graphene monolayers (layer-1) grown across SiC(0001) the resulting strain is distributed across terraces that can exceed several micrometers thus diminishing this effect. Sidewall GNRs are both limited in their lateral dimension and covalently bonded to the graphene buffer layer and/or SiC substrate, so in this system the strain is distributed over a comparatively small region and the effects can be much more dramatic. In order to mediate the lattice strain the laterally pinned GNR could partially delaminate from the SiC substrate near the step edge, thus forming the observed upward bulge and the distortion of the lattice.

The effect of strain is even more pronounced for multilayered epitaxial graphene (MEG) on SiC($000\bar{1}$), where it is common to observe several nm graphene 'pleats' running parallel and perpendicular to step bunches across the surface [19]. MEG

is characterized by multiple rotational stacking faults which effectively decouple the graphene layers from one another and the SiC substrate, as evidenced by an increase in the out-of-plane lattice constant relative to Bernal stacked graphite as measured by X-ray diffraction [133]. These facts would suggest that graphene layers are more capable of mechanical deformation when the interaction between the substrate and the graphene, and the interaction between the graphene layers itself, is weaker. For instance pleats have not been observed for monolayer (layer-1) or bilayer (layer-2) epitaxial graphene on SiC(0001), but pleat-like features have been observed for thicker graphene layers grown on this surface [310]. As the thickness of the graphene increases, the coupling between the graphene and the SiC substrate decreases thus increasing the likelihood of mechanical deformation in the presence of strain. Furthermore, mechanical deformation and the resulting inhomogeneous strain field in the GNR could result in a slight rotational stacking fault between successive graphene layers in the ribbon, thus preserving the sublattice symmetry over the basal plane portion of GNR [137, 255]. Further evidence of strain is presented in the next section, which concerns the electronic states of different GNR's as measured by scanning tunneling spectroscopy (STS).

4.3.3 Electronic States in sidewall graphene nanoribbons

STS measurements were performed on the sidewall GNRs presented in the previous section. In the simplest approximation, STS measures the electron energy dependent local density of states (LDOS) of the surface beneath the tip (Section 2.3.2). Figure 4.13 is a 3D representation of the the on-axis, sidewall GNR in Figure 4.8. The colored circles indicate the approximate locations of STS performed as the sample drifted laterally. The sample drift velocity and STS locations were confirmed by comparison to topographical STM images acquired both before and after the series of STS measurements, which are shown in Figures 4.14 - 4.16. The first two figures

show how the electronic states in the GNR change as the ribbon transitions from the sidewall nanofacet onto the SiC terrace. The first STS measurement (red or rightmost marker in Figure 4.13) was acquired just over the edge the SiC step on the sidewall nanofacet, whereas the second (purple or middle marker in Figure 4.13) was acquired on the left side of the bulge discussed in the previous section. An energy gap of 400 meV is present in both Figures 4.14 and 4.15. In addition, a collection of energy states are present at higher energies in the form of peaks in the STS measurements. These states demonstrate electron-hole symmetry as would be expected for graphene [45], which is indicated by the black lines in each Figure. These black lines are the electron states (acquired at positive sample bias) mirrored about E_D, the assumed Dirac point energy (note that energies are referenced at $V_B = E_F = 0$). E_D is determined visually to maximize the electron-hole symmetry. In both cases $E_D < 50$ meV, indicating that the graphene in these regions is slightly p-doped, in agreement with recent transport [305] and ARPES [311] measurements. The overall dI/dV scale of the electron and hole states varies by approximately a factor of 2, which can be attributed to asymmetry in the tunneling matrix M at positive and negative sample bias [181]. If these electronic states are indexed by integers in order of increasing energy ($N = 1, 2, \ldots$ for the electron states, and $N = -1, -2, \ldots$ for the holes states), it can be shown that the energy of each states $E_N = E_1\sqrt{N}$. The $\sqrt{N}$ energy scaling is succinctly shown by the energy level fan plots in Figures 4.14 and 4.15.

The $\sqrt{N}$ energy scaling is also observed in the case of monolayer graphene in a perpendicular magnetic field B. The magnetic field induces quantized cyclotron orbits, causing the graphene density of states to reorganize into quantized states known as Landau levels. The Landau levels are responsible for the quantum hall effect (QHE) in two-dimensional electron gases, as described in section 1.2.2. The energy of a Landau Level in graphene is $E_N = \lambda v_F \sqrt{2e\hbar B|N|}$, where $\lambda = \pm 1$ for

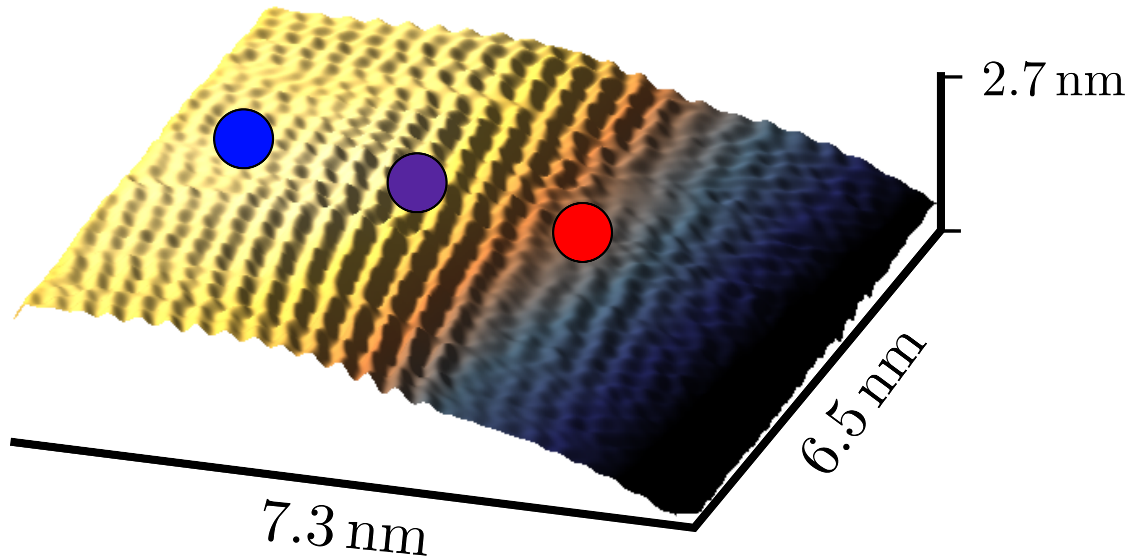

Figure 4.13: 3D rendering of the on-axis, sidewall GNR in Figure 4.8c. The colored marks represent the approximate locations were STS was performed as the sample drifted laterally with respect to the tip scanning window.

the electron and holes states, respectively. In my experiment, there was no applied magnetic field, so the electronic states observed by STS must have a different origin which yields a similar electronic structure.

Theory predicts that strain in graphene can result in a zero magnetic field QHE [45]. Strain which distorts the graphene smoothly also distorts the $\mathbf{K}$ and $\mathbf{K}'$ points in the graphene Brillouin zone, similar to the manner in which a magnetic field affects the charge carriers in a two-dimensional electron gas [312]. More generally, a 2D strain field generates a gauge field in the electronic states of graphene. The gauge field may consist of either a scalar and/or vector potential field, depending upon the spatial dependence of the 2D strain field. These potentials enter the graphene Hamiltonian analogously to the scalar and vector potentials from electromagnetism. The strain field must be non-uniform to generate a pseudo-magnetic field because $\mathbf{B} = \nabla \times \mathbf{A}$. Interestingly, a non-uniform strain field was observed in the crystal lattice of the GNR in the previous section (Fig. 4.9). Assuming that the electronic states near

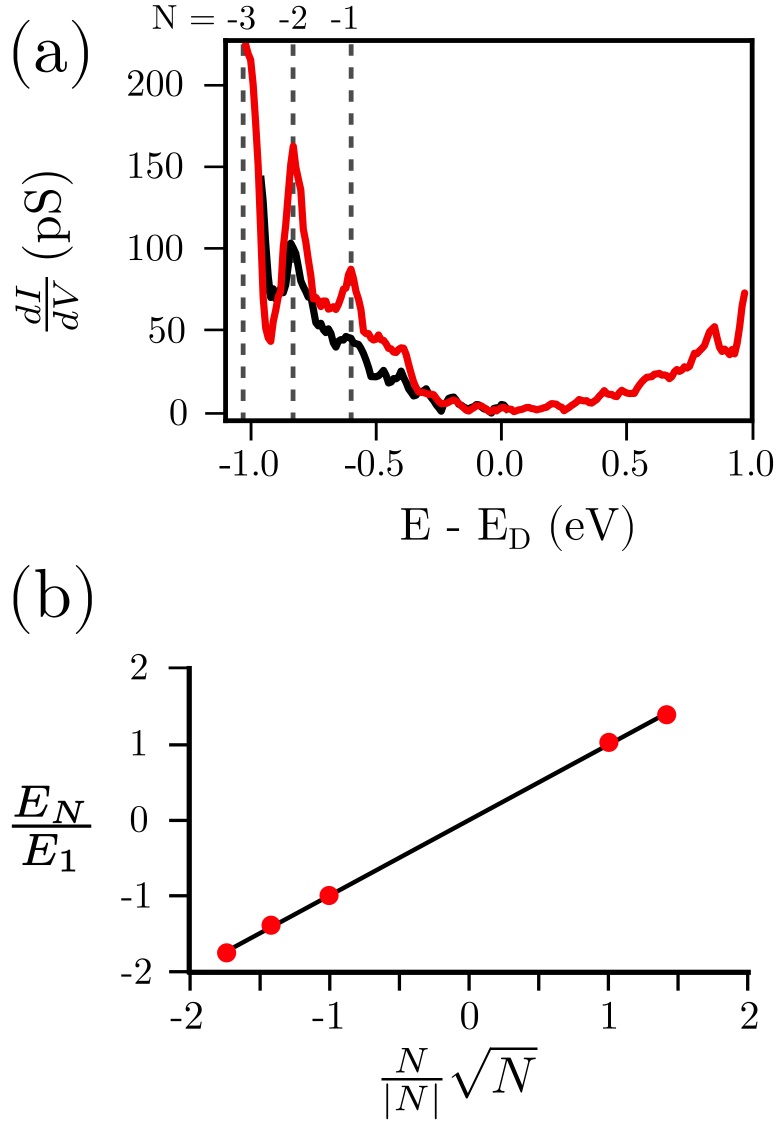

Figure 4.14: (a) STS (red line) on the on-axis, sidewall GNR in Figure 4.13 at the red (right hand side) marker. A possible energy gap (limited by the noise level of the current) of $\sim 400\,\text{meV}$ is centered about the Fermi energy ($V_B = 0\,\text{V}$). Several distinct peaks are present at higher energies at both positive and negative sample bias. The black line at negative sample bias is the electron states (positive sample bias) mirrored about the E_D to demonstrate electron-hole symmetry. The peak energy spacing is $E_N \propto \sqrt{N}$ where N is the index of the peak. (b) Pseudo-Landau level fan plot for the peaks identified in (a).

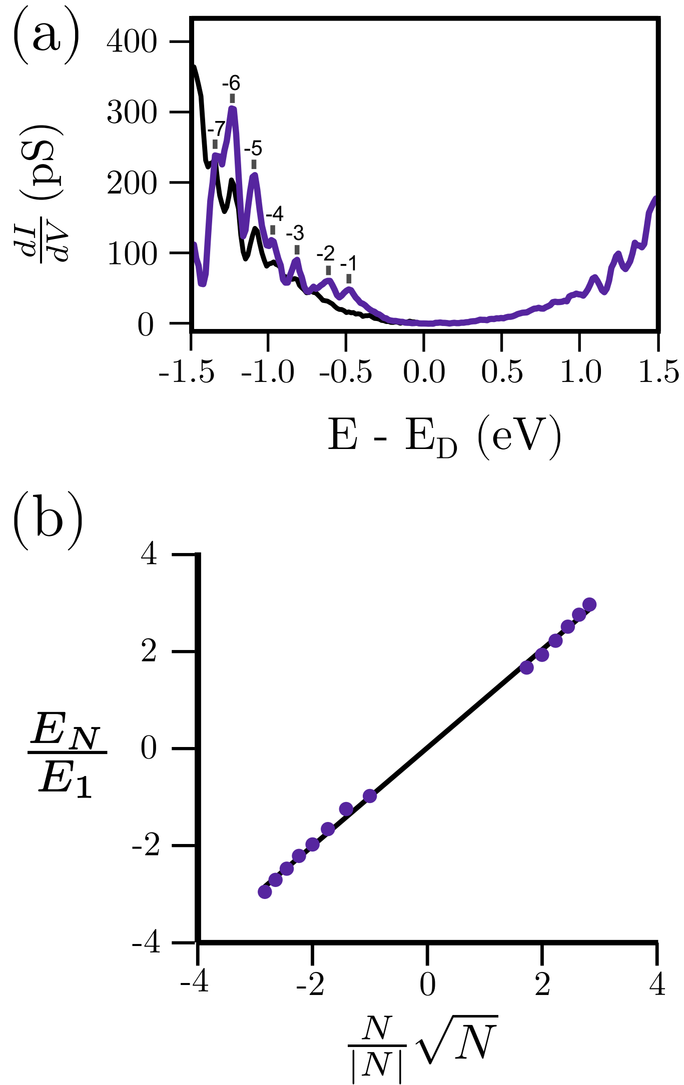

Figure 4.15: (a) STS (purple line) on the on-axis, sidewall GNR in Figure 4.13 at the purple (middle) marker. The energy gap of $\sim 400\,\text{meV}$ about the Fermi energy ($V_B = 0\,\text{V}$) is more distinct in this region. This STS scan swept a larger range of sample biases compared to figure 4.14, revealing even more electron-hole symmetric peaks (identified by tick marks) at higher energy. (b) Pseudo-Landau level fan plot for the peaks identified in (a)

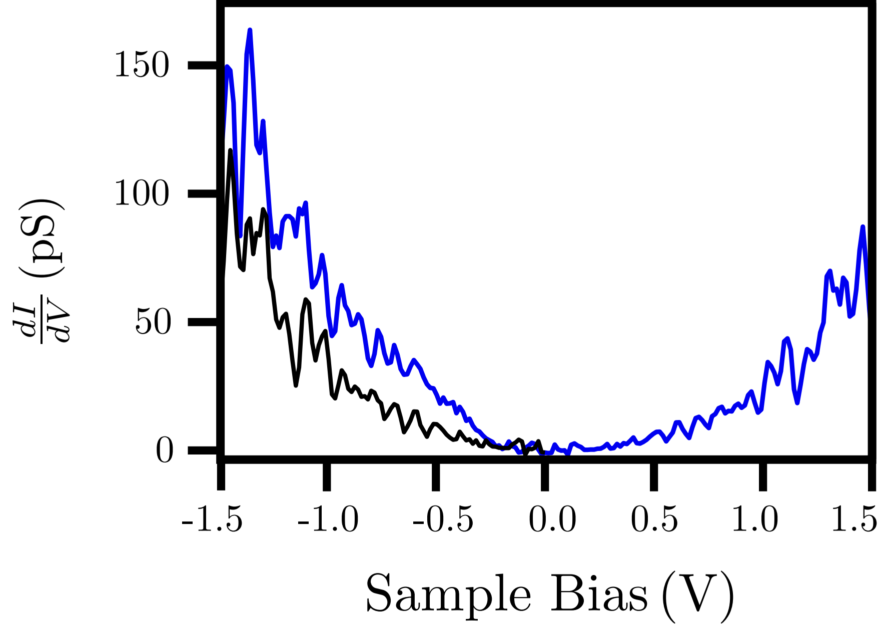

Figure 4.16: STS (blue line) on the on-axis, sidewall GNR in Figure 4.13 at the blue (left hand side) marker. There is no clear energy gap in this region but a large collection of peaks are visible which display electron-hole symmetry. However, unlike the previous spectra, only some the peaks seem to follow a $E_N \propto \sqrt{N}$ energy dependence.

the curved/distorted region of the on-axis GNR are pseudo-Landau levels (LLs) resulting from strain, it is possible to calculate a corresponding pseudo-magnetic field $B_p = E_1/(2ev_F{}^2\hbar)$. For the graphene sidewall (red location), $B_p = 270\,\mathrm{T}$, whereas on the curved portion of the GNR bulge (purple location) the pseudo-magnetic field decreased to $B_p = 185\,\mathrm{T}$. Pseudo-magnetic fields from non-uniform strain were previously observed by STS of graphene grown on Pt, where the thermal expansion mismatch between the substrate and the graphene resulted in fairly large graphene 'bubbles' with peak pseudo-magnetic fields exceeding 300 T [313]. Other groups have also measured electronic states in graphene consistent with pseudo-magnetic fields on both Cu [314] and graphite [315]. All previous observations of pseudo-magnetic fields in graphene were accomplished at low-temperature; for all measurements presented in this thesis the epitaxial graphene was stuided at room-temperature.

The last STS measurement was acquired near the physical edge of the GNR,

where it has fully settled onto the SiC terrace (blue or leftmost marker in Figure 4.13) This plot is significantly different compared to the previous two. For instance, there is no obvious energy gap in the spectrum. There are a very large number of peaks in the spectrum and they mostly appear to obey electron-hole symmetry. Electron-hole symmetry was confirmed by comparison with the mirrored states as done previously, which also confirmed that the graphene in this region is only slightly p-doped. However, the majority of these peaks actually seem to disperse linearly with respect to sample bias, and at this point their origin is unclear. However, since this spectra was acquired close to the physical edge of the GNR it is possible that these states are related to an edge-induced change in the electronic structure or due to quantum confinement.

STS measurements were also performed on the dimpled GNR sample. Figure 4.17 shows spectra acquired on the dimpled GNR discussed in the previous section (Figure 4.10). The color coded narrow strips on the SiC sidewall nanofacet (lower-left hand corner of Figure 4.17a) denote regions where STS spectra were acquired and averaged together, with the corresponding color coded, averaged spectra shown in Figure 4.17b. The average spectra on the SiC sidewall exhibit electron-hole symmetry and peaks that correspond roughly with pseudo-LL states in graphene. However, there appears to be a separate set of peaks linearly spaced in energy which obscure these pseudo-LL states. There also appears to be a large energy gap in all of these spectra, although it is difficult to conclude this with certainty. Figure 4.17c shows STS of the GNR acquired on the basal plane terrace of SiC (gray region in the upper-right hand corner of Figure 4.17a). The STS on the SiC terrace is more reminiscent of STS performed on monolayer graphene (layer-1). The slight shoulder in the density of states (DOS) at $\sim 0.5\,\mathrm{V}$ is often attributed to the the graphene Dirac point where the overall DOS should reach a minimum, corresponding to significant n-doping of the graphene on the terrace. In fact, this value is consistent with the typical doping level of layer-1

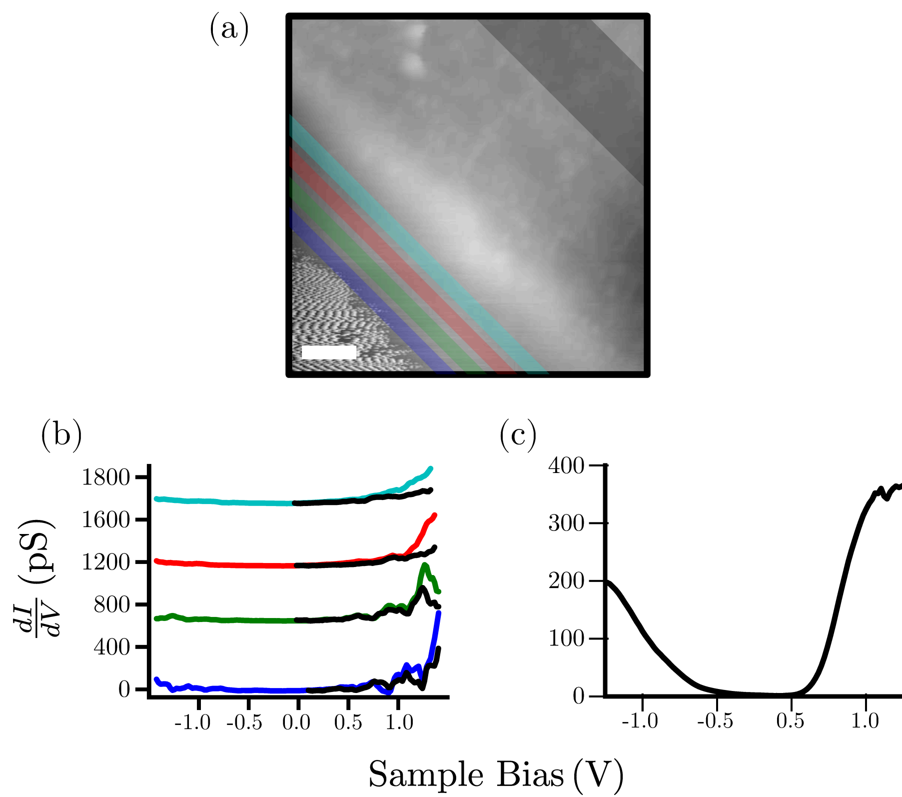

Figure 4.17: STS of a sidewall GNR on the dimpled SiC sample. (a) Color coded regions of interest wherein spectra were averaged together and plotted in (b) and (c). The image shows the line-by-line subtracted topography of the GNR as it transitions from the basal plane to the nanofacet of the SiC. The scale bar is equal to 2 nm.

graphene on SiC(0001). Conversely, the spectra from the SiC appear either undoped or slightly p-doped. Therefore, the GNR has a very large doping profile that is consistent with recent ARPES measurements [311].

In many ways, STS of the dimpled GNRs are more complicated compared to the STS on the on-axis sample discussed earlier in this section. The graphene on the on-axis sample is multilayered and so the doping is uniform throughout the nanoribbon. Based upon my analysis the on-axis GNRs are nominally undoped or only slightly p-doped across the entire width. The dimpled GNR has a doping profile which transitions from nominally undoped on the SiC sidewall to $\sim 0.5\,\text{eV}$ on the SiC terrace. This voltage gradient occurs over a space of about 10 nm, corresponding to an in-plane electric field of about $1 \times 10^7\,\text{V/m}$. In addition, the graphene on the terrace of the dimpled SiC is *uniformly*, compressively strained, with no evidence of a bulge at the SiC step edge which can relax the graphene lattice (the apparent bulge in Figure 4.17 is consequence of the line-by-line subtraction method used). The only strain gradient evident on the dimpled GNR is right at the boundary where the graphene curves over onto the SiC sidewall nanofacet (Fig. 4.11). However, this transition does not occur smoothly over the graphene atomic lattice, resulting in what appears to be a $(\sqrt{3} \times \sqrt{3})\text{R}30°$ electronic scattering pattern at the SiC edge. Furthermore, the graphene lattice imaged on the SiC nanofacet in Figure 4.11 does not appear non-uniformly strained. Both the doping profile and the lack of a clear strain gradient could contribute to the complexity of the STS acquired on the dimpled SiC GNRs.

4.3.4 Buffer Layer

The $(6\sqrt{3} \times 6\sqrt{3})\text{R}30°$ diffraction patterns in Figure 4.4 implies that the surface phase on the sidewall GNR SiC terraces is the interfacial graphene-SiC buffer layer. However, it is difficult to identify the characteristic $(6\sqrt{3} \times 6\sqrt{3})\text{R}30°$ or 6×6 buffer layer surface reconstruction usually observed for epitaxial graphene grown in UHV

[205, 210, 309]. The lack of a diffuse background in the LEED pattern after heating to at least 850 ° C disfavors a thin, amorphous film coating the buffer layer graphene. The ratio of the graphene and SiC diffraction peaks and Auger signal attenuation measurements are consistent with layer-0 or bare buffer layer SiC(0001). However, it is worth commenting that these techniques measure the *average* surface composition over an area of approximately $0.2\,\mathrm{mm}^2$. The AES model present in section 3.2 is strictly valid only for surfaces with a uniform coverage of graphene layers. Non-uniform and uniform graphene coated substrates with the same average surface coverage will have different Si/C Auger electron intensity ratios because of the electrons are exponentially attenuated as a function of layer thickness. In addition, the coherence length for standard LEED optics is between $10 - 20\,\mathrm{nm}$ so it is impossible to comment on the long-range order of the buffer layer surface beyond this limit.

STM on the ex-situ grown sidewall GNR samples was made considerably difficult by the disordered surface phase present on the majority of the SiC surface. ARPES measurements indicate that the buffer layer graphene on SiC(0001) is an insulator, so tunneling on this surface actually occurs through the buffer layer into the doped SiC [316]. This can lead to very small tip-sample separations and it is even possible that the STM tip is in contact with buffer layer during these measurements [317]. The buffer layer is also much more chemically reactive than graphene [318], as evidenced by larger, mobile features on this surface which can irreparably damage STM tips during scans. Therefore, very little systematic STM was performed on this surface.

4.4 Conclusion

In this chapter I have discussed the generic features of GNRs and some of the particularly exciting and challenging aspects of sidewall GNRs on SiC(0001). Room-temperature STM in UHV was utilized to study the atomic-scale structure of sidewall GNRs on both on-axis and off-axis (dimpled) SiC(0001) samples, grown ex-situ using

CCS. I have shown that the exact structure of SiC sidewall nanofacets can differ from what is usually measured using AFM, and that EFM is insensitive to GNR overgrowth and edge structure. The SiC nanofacets self-assembled during GNR growth were found to depend upon the SiC step bunch height and the local SiC vicinality (ie. step bunch density). This finding could be used to control GNR device fabrication in a single-step or multiple-step process. All SiC nanofacets were found to consist of multiple merged or segregated sidewall nanofacets, where large step bunches were more likely to form multiple distinct nanofacets.

Atomic-scale STM images have conclusively proved the presence of graphene on SiC sidewall nanofacets after high-temperature annealing. The graphene crystal lattice is found to be continuous from the upper SiC basal plane terraces onto the SiC sidewalls. STM images show that the crystallographic orientation of graphene nanoribbons is determined primarily by the epitaxial relationship between graphene and the SiC(0001) surface. This observation can be used to predict and/or control the edge-type (zig-zag vs. armchair) of a sidewall GNR. Because of the high formation temperatures, sidewall GNRs should have minimal edge roughness, particularly non-overgrown GNRs. Unfortunately, I only observed overgrown GNRs, and the physical edge of the GNR was never directly imaged because of obscuring debris stemming from the disordered terrace buffer layer graphene.

Overgrown sidewall GNRs consisted of either single-layer or multiple-layers on the basal plane, but in each case, the graphene thickness on the sidewall itself remains undetermined. The amount of graphene overgrowth (total nanoribbon width) and thickness of the overgrown portions seems to depend on the growth parameters, the local step-density and the initial step bunch height. Multilayered sidewall GNRs were shown to possess non-uniform, compressive strain fields near the the SiC sidewall edges. Conversely, the single-layered GNR studied was under apparently uniform compressive strain. The compressive strain in the GNR graphene lattice was as high

as 12 %. The interfacial graphene-SiC buffer layer on the basal plane of SiC(0001) underneath a monolayer, overgrown GNR had a similar amount of compressive strain. Based upon STM imaging of the GNR crystal lattice, I proposed that the strain fields are inhomogeneous in multilayered GNRs which would preserve the electronic properties of monolayer graphene as famously observed in MEG on SiC($000\bar{1}$). This was confirmed using STS measurements in distorted regions of the GNR, which indicated the presence of strain-induced quantized energy states and large energy gaps near the Fermi energy consistent with inhomogeneous strain fields in monolayer graphene.

CHAPTER V

CONCLUSION

5.1 Summary of Results

In this thesis I have presented my research on the growth of epitaxial graphene on SiC(0001) and SiC(000-1), and the electronic properties of self-organized epitaxial graphene nanoribbons on SiC(0001). I have systematically demonstrated that the sub-monolayer growth of epitaxial graphene on SiC can be understood by considering the thermodynamic properties of SiC and basic mass-transfer theory. I have integrated these concepts into a model based on kinetic rate equations, which was verified by comparison with experimental graphene growth rate data that I acquired using a novel UHV furnace. These findings provide a theoretical basis for controlling the growth rate of the epitaxial graphene on SiC, which is particularly important for directly growing nanostructures of graphene on SiC. I performed scanning tunneling microscopy measurements on epitaxial graphene nanoribbons grown on the sidewall nanofacets of SiC(0001). For the overgrown nanoribbons that studied I was able to determine that the graphene crystal lattice is continuous from the sidewall nanofacets onto the SiC terraces with atomic-scale resolution. Physical distortions of the graphene lattice were observed indicating a large degree of strain in this material. Scanning tunneling spectroscopy measurements in the distorted regions were used to detect quantized electronic states, which are expected for strained graphene. My measurements appear to be the first to resolve such states at room temperature, and in a system where the strain field potentially could be designed by careful lithographic patterning and graphene growth.

The growth of epitaxial films is controlled by both the growth conditions (ie. In

terms of MBE, the deposition flux and substrate temperature), and the quality and type of substrate used. The substrate quality is even more important for epitaxial graphene growth on SiC because the carbon adatoms which ultimately form the graphene are released from the substrate during thermal decomposition. I have shown that the growth of sub-monolayer epitaxial graphene can be accurately modeled using a kinetic rate equation for the sublimation of SiC. At the experimental temperature range studied only silicon is sublimated, so the graphene growth rate directly tracks the silicon sublimation rate. I have confirmed this model by direct comparison with experimental graphene growth rate measurements performed in a novel, in-situ RF induction graphene growth furnace based on the confinement-controlled sublimation design. In the simplest form the kinetic graphene growth rate model has only two dependent variables (the furnace temperature and pressure) and two fitting parameters. One of these fitting parameters (ΔH) is highly constrained because it is the enthalpy of sublimation for SiC. An unconstrained fit of the sub-monolayer graphene growth rate resulted in a SiC (ΔH) which is in agreement with both experimental and theoretical results in the literature. Therefore, the growth rate fitting procedure effectively characterizes the properties of new furnaces. Once characterized, the model can be used to predict the graphene growth rate at any furnace pressure or temperature. The sub-monolayer growth rate model was presented in a generalized form which can easily incorporate different chemical reactions (such as etching of the SiC or graphene by hydrogen gas) or physical processes (such as higher temperature sublimation of carbon molecules). In addition, the model can be extended to include the mean-field effects of atomistic surface diffusion processes on the graphene growth rate and structure.

Traditionally, graphene growth on Si and C faces of SiC has been considered as different processes because of the observed dissimilar growth rates and epitaxial structure. On the contrary, I have demonstrated that the graphene grows at the same

rate for both faces of SiC in the sub-monolayer regime. This finding implies that the *initial* growth process may be similar for both faces of SiC. The difference in growth rates for thicker graphene films implies that the growth mechanism begins to diverge after a monolayer of graphene has formed. Multiple-layer graphene growth rates were consistently lower than what was predicted by the sub-monolayer growth rate model, with the C face growth rate decreasing slower compared to the Si face growth rate as expected. Unlike traditional epitaxial material, graphene grows in a 'bottom-down instead of the normal 'top-up configuration; the last graphene layer grown is at the bottom of the multilayer stack. The formation of subsurface graphene layers is still controlled by the sublimation rate of the SiC substrate, which should decrease as a function of the number of graphene layers. Although not definitive, AFM images of the surface graphene layer indicate that the graphene quality is correlated with the decrease in the silicon sublimation rate. It is also possible that the covalently bonded interfacial graphene buffer layer on the Si face of SiC plays a role in the sharp decrease in the graphene growth rate after a complete buffer layer has formed. Further research is necessary to determine how the graphene growth changes from sub-monolayer to the multi-layer regimes.

Scanning tunneling microscopy was used to study structure and electronic properties of self-organized sidewall graphene nanoribbons grown on SiC(0001). EFM indicated that the graphene growth was limited to the SiC sidewall nanofacets. STM measurements of these samples showed that the GNRs were consistently overgrown with a significant fraction of the nanoribbon width residing on the SiC basal plane terraces. Atomic resolution STM images proved that the overgrown GNR crystal lattice is continuous from SiC nanofacets onto the SiC terraces. I also observed a large degree of distortion in the graphene lattice on and near the SiC nanofacets. Out-of-plane distortions were observed were the graphene lattice curves over on the SiC sidewalls. In addition, the graphene lattice in these regions was non-uniformly

compressively strained relative to orientation of the sidewall nanofacet. The strain in the GNR changes the electronic properties of the material by inducing quantized energy states in the form of pseudo-Landau levels. These quantized states appeared to open a band gap in the GNR at the graphene Dirac point, despite the fact theory predicts a single quantized state at this energy. The largest band gap measured was approximately 0.4 eV. The STS measurements also detected a large doping profile across the width of the overgrown graphene nanoribbons that is consistent with a recent ARPES study.

5.2 Future Studies

Epitaxial graphene on SiC is an incredibly rich system with many possible future experiments. A natural progression of my research would be to measure the graphene growth rate on a finer time-scale to determine how the growth rate changes as a function of graphene thickness. Monitoring the graphene growth rate during graphene growth would be the ideal manner to perform this measurement. Reflection high-energy electron diffraction (RHEED) is commonly used to monitor the growth rate during MBE growth with sub-monolayer resolution, but this technique cannot probe sample grown in a CCS style furnace, and may not be compatible with the extreme temperatures/pressures involved with epitaxial graphene growth in general. Surface X-ray scattering would be ideal for this type of growth experiment because the SiC sample could be physically confined and still remain accessible to the high energy beams from a synchrotron source.

Integrating an SPM instrument such as STM or atomic-scale AFM into the UHV-F system would enable an atomistic look at the growth process. SPM would complement the large-scale measurements acquired by LEED and AES by providing snapshots of

the graphene growth process from start to finish. In-situ STM would enable direct observation of the graphene-SiC interfacial buffer layers. In addition, ex-situ grown sidewall graphene nanoribbon samples are predominantly covered by the graphene buffer layer, which appears to become contaminated upon transfer out of the growth furnace. This contamination tends to accumulate at the edges of the graphene nanoribbons, thus obscuring their physical structure. An in-situ STM could be used to directly characterize the sidewall graphene nanoribbons grown on SiC(0001), and could provide confirmation of the graphene nanoribbon edge structure.

REFERENCES

[1] S. Freinkel, "A brief history of plastic's conquest of the world," *Scientific American*, 2011. [Online]. Available: http://www.scientificamerican.com/article.cfm?id=a-brief-history-of-plastic-world-conquest

[2] M. Segal, "Selling graphene by the ton," *Nature Nanotechnology*, vol. 4, no. 10, pp. 612–614, 2009. [Online]. Available: http://www.nature.com.prx.library.gatech.edu/nnano/journal/v4/n10/full/nnano.2009.279.html

[3] M. Segal, "Material history: Learning from silicon," *Nature*, vol. 483, no. 7389, pp. S43–S44, 2012. [Online]. Available: http://dx.doi.org/10.1038/483S43a

[4] V. Gavryushin. (2013) Graphene brillouin zone and electronic energy dispersion. The Wolfram Demonstrations Project. [Online]. Available: http://demonstrations.wolfram.com/GrapheneBrillouinZoneAndElectronicEnergyDispersion/

[5] C. Riedl, C. Coletti, T. Iwasaki, A. A. Zakharov, and U. Starke, "Quasi-free-standing epitaxial graphene on SiC obtained by hydrogen intercalation," *Physical Review Letters*, vol. 103, no. 24, p. 246804, 2009.

[6] N. Srivastava, G. He, Luxmi, and R. M. Feenstra, "Interface structure of graphene on SiC($000\bar{1}$)," *Physical Review B*, vol. 85, no. 4, p. 041404, 2012. [Online]. Available: http://link.aps.org/doi/10.1103/PhysRevB.85.041404

[7] K. S. Novoselov, D. Jiang, F. Schedin, T. J. Booth, V. V. Khotkevich, S. V. Morozov, and A. K. Geim, "Two-dimensional atomic crystals," *Proceedings of the National Academy of Sciences of the United States of America*, vol. 102, no. 30, pp. 10 451–10 453, 2005. [Online]. Available: http://www.pnas.org/content/102/30/10451.abstract

[8] C. Berger, Z. Song, T. Li, X. Li, A. Y. Ogbazghi, R. Feng, Z. Dai, A. Marchenkov, E. H. Conrad, P. N. First, and W. A. DeHeer, "Ultrathin epitaxial graphite: 2d electron gas properties and a route toward graphene-based nanoelectronics," *Journal of Physical Chemistry B*, vol. 108, pp. 19 912–19 916, 2004.

[9] K. S. Novoselov, V. I. Fal'ko, L. Colombo, P. R. Gellert, M. G. Schwab, and K. Kim, "A roadmap for graphene," *Nature*, vol. 490, no. 7419, pp. 192–200, 2012. [Online]. Available: http://dx.doi.org/10.1038/nature11458

[10] S. Bae, H. Kim, Y. Lee, X. Xu, J.-S. Park, Y. Zheng, J. Balakrishnan, T. Lei, H. Ri Kim, Y. I. Song, Y.-J. Kim, K. S. Kim, B. Özyilmaz, J.-H. Ahn, B. H. Hong, and S. Iijima, "Roll-to-roll production of 30-inch graphene films for transparent electrodes," *Nature Nanotechnology*, vol. 5, no. 8, pp. 574–578, 2010. [Online]. Available: http://www.nature.com.prx.library.gatech.edu/nnano/journal/v5/n8/full/nnano.2010.132.html

[11] K. Kim, J.-Y. Choi, T. Kim, S.-H. Cho, and H.-J. Chung, "A role for graphene in silicon-based semiconductor devices," *Nature*, vol. 479, no. 7373, pp. 338–344, 2011. [Online]. Available: http://www.nature.com.prx.library.gatech.edu/nature/journal/v479/n7373/full/nature10680.html

[12] H. Yang, J. Heo, S. Park, H. J. Song, D. H. Seo, K.-E. Byun, P. Kim, I. Yoo, H.-J. Chung, and K. Kim, "Graphene barristor, a triode device with a gate-controlled schottky barrier," *Science*, vol. 336, no. 6085, pp. 1140–1143, 2012. [Online]. Available: http://www.sciencemag.org/content/336/6085/1140

[13] B. H. Hong, "Korean graphene research activities and roadmap," 2012, talk presented at the Graphene Conference, April 10-13, 2012 in Brussels, Belgium.

[14] Q. Tannock, "Exploiting carbon flatland," *Nature Materials*, vol. 11, no. 1, pp.

2–5, 2012. [Online]. Available: http://www.nature.com/nmat/journal/v11/n1/full/nmat3211.html

[15] H. Park, A. Afzali, S.-J. Han, G. S. Tulevski, A. D. Franklin, J. Tersoff, J. B. Hannon, and W. Haensch, "High-density integration of carbon nanotubes via chemical self-assembly," *Nature Nanotechnology*, vol. 7, no. 12, pp. 787–791, 2012. [Online]. Available: http://www.nature.com.prx.library.gatech.edu/nnano/journal/v7/n12/full/nnano.2012.189.html

[16] Y. Q. Wu, D. Farmer, A. Valdes-Garcia, W. J. Zhu, K. A. Jenkins, C. Dimitrakopoulos, P. Avouris, and Y. M. Lin, "Record high RF performance for epitaxial graphene transistors," in *Electron Devices Meeting (IEDM), 2011 IEEE International*, 2011, pp. 23.8.1–23.8.3.

[17] L. Liao and X. Duan, "Graphene for radio frequency electronics," *Materials Today*, vol. 15, no. 78, pp. 328–338, 2012. [Online]. Available: http://www.sciencedirect.com/science/article/pii/S1369702112701384

[18] M. Bohr, "Moore's law in the innovation era," *Proceedings of SPIE*, vol. 7974, p. 797402, 2011. [Online]. Available: http://dx.doi.org/10.1117/12.883462

[19] W. A. de Heer, C. Berger, M. Ruan, M. Sprinkle, X. Li, Y. Hu, B. Zhang, J. Hankinson, and E. Conrad, "Large area and structured epitaxial graphene produced by confinement controlled sublimation of silicon carbide," *Proceedings of the National Academy of Sciences*, vol. 108, no. 41, pp. 16 900–16 905, 2011. [Online]. Available: http://www.pnas.org/content/108/41/16900.abstract

[20] P. R. Wallace, "The band theory of graphite," *Physical Review*, vol. 71, no. 9, pp. 622–634, 1947.

[21] J. W. McClure, "Diamagnetism of graphite," *Physical Review*, vol. 104,

no. 3, pp. 666–671, 1956. [Online]. Available: http://link.aps.org/doi/10.1103/PhysRev.104.666

[22] J. W. McClure, “Band structure of graphite and de haas-van alphen effect,” *Physical Review*, vol. 108, no. 3, pp. 612–618, 1957.

[23] J. C. Slonczewski and P. R. Weiss, “Band structure of graphite,” *Physical Review*, vol. 109, no. 2, pp. 272–279, 1958.

[24] S. Iijima, “Helical microtubules of graphitic carbon,” *Nature*, vol. 354, no. 6348, pp. 56–58, 1991. [Online]. Available: http://dx.doi.org/10.1038/354056a0

[25] R. Saito, M. Fujita, G. Dresselhaus, and M. Dresselhaus, “Electronic structure of chiral graphene tubules,” *Applied Physics Letters*, vol. 60, no. 18, pp. 2204–2206, 1992.

[26] N. Hamada, S.-i. Sawada, and A. Oshiyama, “New one-dimensional conductors: Graphitic microtubules,” *Physical Review Letters*, vol. 68, no. 10, pp. 1579–1581, 1992. [Online]. Available: http://link.aps.org/doi/10.1103/PhysRevLett.68.1579

[27] H. Ajiki and T. Ando, “Electronic states of carbon nanotubes,” *Journal of the Physical Society of Japan*, vol. 62, no. 4, pp. 1255–1266, 1993. [Online]. Available: http://jpsj.ipap.jp/link?JPSJ/62/1255/

[28] H. Ajiki and T. Ando, “Aharonov-bohm effect in carbon nanotubes,” *Physica B: Condensed Matter*, vol. 201, pp. 349 – 352, 1994. [Online]. Available: http://www.sciencedirect.com/science/article/pii/0921452694911126

[29] J.-C. Charlier, P. Lambin, and T. Ebbesen, “Electronic properties of carbon nanotubes with polygonized cross sections,” *Physical Review B*, vol. 54, no. 12, pp. 8377–8380, 1996.

[30] T. Ando, T. Nakanishi, and R. Saito, “Berry’s phase and absence of back scattering in carbon nanotubes,” *Journal of the Physical Society of Japan*, vol. 67, no. 8, pp. 2857–2862, 1998. [Online]. Available: http://jpsj.ipap.jp/link?JPSJ/67/2857/

[31] C.-H. Kiang, M. Endo, P. M. Ajayan, G. Dresselhaus, and M. S. Dresselhaus, “Size effects in carbon nanotubes,” *Physical Review Letters*, vol. 81, no. 9, pp. 1869–1872, 1998. [Online]. Available: http://link.aps.org/doi/10.1103/PhysRevLett.81.1869

[32] R. Saito, G. Dresselhaus, and M. S. Dresselhaus, “Trigonal warping effect of carbon nanotubes,” *Physical Review B*, vol. 61, no. 4, pp. 2981–2990, 2000. [Online]. Available: http://link.aps.org/doi/10.1103/PhysRevB.61.2981

[33] T. Ando, A. B. Fowler, and F. Stern, “Electronic properties of two-dimensional systems,” *Reviews of Modern Physics*, vol. 54, no. 2, 1982.

[34] N. H. Shon and T. Ando, “Quantum transport in two-dimensional graphite system,” *Journal of the Physical Society of Japan*, vol. 67, no. 7, pp. 2421–2429, 1998. [Online]. Available: http://jpsj.ipap.jp/link?JPSJ/67/2421/

[35] F. Bloch, “Quantum mechanics of electrons in crystal lattices,” *Zeitschrift für Physik*, vol. 52, pp. 555–600, 1928.

[36] C. Bena and G. Montambaux, “Remarks on the tight-binding model of graphene,” *New Journal of Physics*, vol. 11, no. 9, p. 095003, 2009. [Online]. Available: http://stacks.iop.org/1367-2630/11/i=9/a=095003

[37] N. W. Ashcroft and N. D. Mermin, *Solid State Physics*. Brooks Cole, 2005.

[38] C. W. J. Beenakker, “Colloquium: Andreev reflection and klein tunneling in

graphene," *Reviews of Modern Physics*, vol. 80, no. 4, pp. 1337–1354, 2008. [Online]. Available: http://link.aps.org/doi/10.1103/RevModPhys.80.1337

[39] K. S. Novoselov, A. K. Geim, S. V. Morozov, D. Jiang, M. I. Katsnelson, I. V. Grigorieva, S. V. Dubonos, and A. A. Firsov, "Two-dimensional gas of massless dirac fermions in graphene," *Nature*, vol. 438, no. 7065, pp. 197–200, 2005. [Online]. Available: http://dx.doi.org/10.1038/nature04233

[40] Y. Zhang, Y. Tan, H. L. Stormer, and P. Kim, "Experimental observation of the quantum hall effect and berry's phase in graphene," *Nature*, vol. 438, no. 7065, pp. 201–204, 2005. [Online]. Available: http://dx.doi.org/10.1038/nature04235

[41] C. Berger, Z. Song, X. Li, X. Wu, N. Brown, C. Naud, D. Mayou, T. Li, J. Hass, A. N. Marchenkov, E. H. Conrad, P. N. First, and W. A. de Heer, "Electronic confinement and coherence in patterned epitaxial graphene." *Science (New York, N.Y.)*, vol. 312, no. 5777, pp. 1191–1196, 2006. [Online]. Available: http://www.ncbi.nlm.nih.gov/pubmed/16614173

[42] D. L. Miller, K. D. Kubista, G. M. Rutter, M. Ruan, W. A. de Heer, P. N. First, and J. A. Stroscio, "Observing the quantization of zero mass carriers in graphene," *Science*, vol. 324, no. 5929, pp. 924–927, 2009. [Online]. Available: http://www.sciencemag.org/content/324/5929/924.abstract

[43] S. Y. Zhou, G.-H. Gweon, A. V. Fedorov, P. N. First, W. A. de Heer, D.-H. Lee, F. Guinea, A. H. Castro Neto, and A. Lanzara, "Substrate-induced bandgap opening in epitaxial graphene," *Nature Materials*, vol. 6, no. 10, pp. 770–775, 2007. [Online]. Available: http://dx.doi.org/10.1038/nmat2003

[44] M. Sprinkle, D. Siegel, Y. Hu, J. Hicks, A. Tejeda, A. Taleb-Ibrahimi, P. Le Fèvre, F. Bertran, S. Vizzini, H. Enriquez, S. Chiang, P. Soukiassian, C. Berger, W. A. de Heer, A. Lanzara, and E. H.

Conrad, "First direct observation of a nearly ideal graphene band structure," *Physical Review Letters*, vol. 103, p. 226803, 2009. [Online]. Available: http://link.aps.org/doi/10.1103/PhysRevLett.103.226803

[45] A. H. Castro Neto, F. Guinea, N. M. R. Peres, K. S. Novoselov, and A. K. Geim, "The electronic properties of graphene," *Reviews of Modern Physics*, vol. 81, no. 1, p. 109, 2009. [Online]. Available: http://link.aps.org/abstract/RMP/v81/p109

[46] O. Klein, "Die reflexion von elektronen an einem potentialsprung nach der relativistischen dynamik von dirac," *Zeitschrift für Physik*, vol. 53, no. 3-4, pp. 157–165, 1929. [Online]. Available: http://dx.doi.org/10.1007/BF01339716

[47] M. I. Katsnelson, K. S. Novoselov, and A. K. Geim, "Chiral tunnelling and the klein paradox in graphene," *Nature Physics*, vol. 2, no. 9, pp. 620–625, 2006. [Online]. Available: http://dx.doi.org/10.1038/nphys384

[48] R. Hull, *Properties of Crystalline Silicon*, ser. EMIS Datareviews Series, R. Hull, Ed. INSPEC, The Institution of Electrical Engineers, 1999. [Online]. Available: http://books.google.com/books?id=C_TWB_0rRLgC

[49] E. H. Hwang, S. Adam, and S. Das Sarma, "Carrier transport in two-dimensional graphene layers," *Physical Review Letters*, vol. 98, p. 186806, 2007. [Online]. Available: http://link.aps.org/doi/10.1103/PhysRevLett.98.186806

[50] E. H. Hwang and S. Das Sarma, "Acoustic phonon scattering limited carrier mobility in two-dimensional extrinSiC graphene," *Physical Review B*, vol. 77, p. 115449, 2008. [Online]. Available: http://link.aps.org/doi/10.1103/PhysRevB.77.115449

[51] S. V. Morozov, K. S. Novoselov, M. I. Katsnelson, F. Schedin, D. C. Elias, J. A. Jaszczak, and A. K. Geim, "Giant intrinSiC carrier mobilities in graphene

and its bilayer," *Physical Review Letters*, vol. 100, p. 016602, 2008. [Online]. Available: http://link.aps.org/doi/10.1103/PhysRevLett.100.016602

[52] J.-H. Chen, C. Jang, S. Xiao, M. Ishigami, and M. S. Fuhrer, "IntrinSiC and extrinSiC performance limits of graphene devices on sio2," *Nature Nanotechnology*, vol. 3, no. 4, pp. 206–209, 2008. [Online]. Available: http://dx.doi.org/10.1038/nnano.2008.58

[53] K. Bolotin, K. Sikes, Z. Jiang, M. Klima, G. Fudenberg, J. Hone, P. Kim, and H. Stormer, "Ultrahigh electron mobility in suspended graphene," *Solid State Communications*, vol. 146, no. 910, pp. 351 – 355, 2008. [Online]. Available: http://www.sciencedirect.com/science/article/pii/S0038109808001178

[54] X. Du, I. Skachko, F. Duerr, A. Luican, and E. Y. Andrei, "Fractional quantum hall effect and insulating phase of dirac electrons in graphene," *Nature*, vol. 462, no. 7270, pp. 192–195, 2009. [Online]. Available: http://dx.doi.org/10.1038/nature08522

[55] K. I. Bolotin, F. Ghahari, M. D. Shulman, H. L. Stormer, and P. Kim, "Observation of the fractional quantum hall effect in graphene," *Nature*, vol. 462, no. 7270, pp. 196–199, 2009. [Online]. Available: http://dx.doi.org/10.1038/nature08582

[56] C. R. Dean, A. F. Young, I. Meric, C. Lee, L. Wang, S. Sorgenfrei, K. Watanabe, T. Taniguchi, P. Kim, K. L. Shepard, and J. Hone, "Boron nitride substrates for high-quality graphene electronics," *Nature Nanotechnology*, vol. 5, no. 10, pp. 722–726, 2010. [Online]. Available: http://dx.doi.org/10.1038/nnano.2010.172

[57] P. Neugebauer, M. Orlita, C. Faugeras, A. Barra, and M. Potemski, "How perfect can graphene be?" *Physical Review Letters*, vol. 103, no. 13, p.

136403, 2009. [Online]. Available: http://link.aps.org.www.library.gatech.edu:2048/doi/10.1103/PhysRevLett.103.136403

[58] M. Orlita, C. Faugeras, P. Plochocka, P. Neugebauer, G. Martinez, D. K. Maude, A. Barra, M. Sprinkle, C. Berger, W. A. de Heer, and M. Potemski, "Approaching the dirac point in High-Mobility multilayer epitaxial graphene," *Physical Review Letters*, vol. 101, no. 26, p. 267601, 2008. [Online]. Available: http://link.aps.org.www.library.gatech.edu:2048/doi/10.1103/PhysRevLett.101.267601

[59] E. Acheson, "Production of artificial crystalline carbonaceous materials," United States Patent No. 492.767, 1893, see http://web.mit.edu/invent/iow/acheson.html; http://people.clarkson.edu/ ekatz/scientists/acheson.html. [Online]. Available: http://people.clarkson.edu/~ekatz/scientists/acheson.html

[60] S. E. Saddow and A. Agarwal, Eds., *Advances in Silicon Carbide Processing and Applications*, 1st ed. Norwood, MA: Artech House, Inc., 2004.

[61] J. A. Lely, "Darstellung von einkristallen von siliciumcarbid und beherrschung von art und menge der eingebauten verunreinigungen," *Berichte der Deutschen Keramischen Gesellschaft*, vol. 32, p. 299, 1955.

[62] S. J. Pearton, *Processing of Wide Band Gap Semiconductors*, 1st ed. New York, USA: Elsevier, Inc., 2013.

[63] P. G. Neudeck, "SiC technology," in *The VLSI Handbook*, 1st ed., W.-K. Chen, Ed. Boca Raton, Florida: CRC Press, 2006.

[64] G. Harris, *Properties of Silicon Carbide*, ser. Emis Datareviews Series. INSPEC, Institution of Electrical Engineers, 1995, no. 13. [Online]. Available: http://books.google.com/books?id=Yy_B8GzxNlgC

[65] R. F. Davis, G. Kelner, M. Shur, J. Palmour, and J. Edmond, "Thin film deposition and microelectronic and optoelectronic device fabrication and characterization in monocrystalline alpha and beta silicon carbide," *Proceedings of the IEEE*, vol. 79, no. 5, pp. 677–701, 1991.

[66] Y. Tairov and V. Tsvetkov, "Investigation of growth processes of ingots of silicon carbide single crystals," *Journal of Crystal Growth*, vol. 43, no. 2, pp. 209–212, 1978. [Online]. Available: http://www.sciencedirect.com/science/article/pii/0022024878901690

[67] R. F. Davis, J. Carter, Calvin H., and C. E. Hunter, "Sublimation of silicon carbide to produce large, device quality single ..." U.S. Patent 4 866 005, 12, 1989, U.S. Classification: 117/98; 117/99; 117/101; 117/107; 117/951; 148/DIG.21; 148/DIG.148 International Classification: H01L 21205; H01L 2136. [Online]. Available: http://www.google.com/patents/US4866005

[68] R. Stein, P. Lanig, and S. Leibenzeder, "Influence of surface energy on the growth of 6H- and 4H-SiC polytypes by sublimation," *Materials Science and Engineering: B*, vol. 11, no. 14, pp. 69–71, 1992. [Online]. Available: http://www.sciencedirect.com/science/article/pii/092151079290193D

[69] D. Barrett, J. McHugh, H. Hobgood, R. Hopkins, P. McMullin, R. Clarke, and W. Choyke, "Growth of large SiC single crystals," *Journal of Crystal Growth*, vol. 128, pp. 358–362, 1993. [Online]. Available: http://www.sciencedirect.com/science/article/pii/002202489390348Z

[70] A. Powell, J. Jenny, S. Muller, H. Mcd. Hobgood, V. Tsvetkov, R. Lenoard, and C. Carter, "Growth of SiC substrates," *International Journal of High Speed Electronics and Systems*, vol. 16, no. 03, pp. 751–777, 2006. [Online]. Available: http://www.worldscientific.com/doi/abs/10.1142/S0129156406004016

[71] M. Treu, R. Rupp, and G. Solkner, "Reliability of SiC power devices and its influence on their commercialization - review, status, and remaining issues," in *Reliability Physics Symposium (IRPS), 2010 IEEE International*, 2010, pp. 156–161.

[72] S. Müller, E. Sanchez, D. Hansen, R. Drachev, G. Chung, B. Thomas, J. Zhang, M. Loboda, M. Dudley, H. Wang, F. Wu, S. Byrappa, B. Raghothamachar, and G. Choi, "Volume production of high quality SiC substrates and epitaxial layers: Defect trends and device applications," *Journal of Crystal Growth*, vol. 352, no. 1, pp. 39–42, 2012. [Online]. Available: http://www.sciencedirect.com/science/article/pii/S0022024811009079

[73] S. Tiwari, T. Undeland, S. Basu, and W. Robbins, "Silicon carbide power transistors, characterization for smart grid applications," in *Power Electronics and Motion Control Conference (EPE/PEMC), 2012 15th International*, 2012, pp. LS6d.2–1–LS6d.2–8.

[74] W. Qian, M. Skowronski, G. Augustine, R. C. Glass, H. M. Hobgood, and R. H. Hopkins, "Characterization of polishing-related surface damage in (0001) silicon carbide substrates," *Journal of The Electrochemical Society*, vol. 142, no. 12, pp. 4290–4294, 1995. [Online]. Available: http://jes.ecsdl.org/content/142/12/4290

[75] L. Zhou, V. Audurier, P. Pirouz, and J. A. Powell, "Chemomechanical polishing of silicon carbide," *Journal of The Electrochemical Society*, vol. 144, no. 6, pp. L161–L163, 1997. [Online]. Available: http://jes.ecsdl.org/content/144/6/L161

[76] M. K. Linnarsson, M. S. Janson, A. Schöner, and B. G. Svensson, "Aluminum and boron diffusion in 4H-SiC," *MRS Proceedings*, vol. 742,

2002. [Online]. Available: http://journals.cambridge.org.prx.library.gatech.edu/article_S1946427400151887

[77] M. Capano, S. Ryu, and J. Cooper, "Surface roughening in ion implanted 4H-silicon carbide," *Journal of Electronic Materials*, vol. 28, no. 3, pp. 214–217, 1999. [Online]. Available: http://www.springerlink.com/index/h0mj338524qu4460.pdf

[78] S. P. Rao, "Implant annealing of al dopants in silicon carbide using silane overpressure," Dissertation, University of South Florida, Tampa, FL, 2005. [Online]. Available: http://purl.fcla.edu/fcla/etd/SFE0001213.

[79] S. Nie, J. M. Wofford, N. C. Bartelt, O. D. Dubon, and K. F. McCarty, "Origin of the mosaicity in graphene grown on cu(111)," *Physical Review B*, vol. 84, p. 155425, 2011. [Online]. Available: http://link.aps.org/doi/10.1103/PhysRevB.84.155425

[80] L. Brillson, *Surfaces and Interfaces of Electronic Materials*, 1st ed., ser. Wiley - IEEE. Wiley-VCH, 2010, vol. 7. [Online]. Available: http://books.google.com/books?id=rFCSlTEcxGMC

[81] M. C. Bartelt and J. W. Evans, "Scaling analysis of diffusion-mediated island growth in surface adsorption processes," *Physical Review B*, vol. 46, no. 19, pp. 12 675–12 687, 1992. [Online]. Available: http://link.aps.org/doi/10.1103/PhysRevB.46.12675

[82] J. A. Stroscio and D. T. Pierce, "Scaling of diffusion-mediated island growth in iron-on-iron homoepitaxy," *Physical Review B*, vol. 49, pp. 8522–8525, 1994. [Online]. Available: http://link.aps.org/doi/10.1103/PhysRevB.49.8522

[83] Z. Zhang and M. G. Lagally, "Atomistic processes in the early stages of

thin-film growth," *Science*, vol. 276, no. 5311, pp. 377–383, 1997. [Online]. Available: http://www.sciencemag.org/content/276/5311/377.abstract

[84] C. Ratsch and J. A. Venables, "Nucleation theory and the early stages of thin film growth," *Journal of Vacuum Science & Technology A: Vacuum, Surfaces, and Films*, vol. 21, no. 5, pp. S96–S109, 2003. [Online]. Available: http://link.aip.org/link/?JVA/21/S96/1

[85] C. Tringides and N. A. T. O. S. A. Division, *Surface Diffusion: Atomistic and Collective Processes*, ser. NATO ASI series / B: NATO ASI series. Springer, 1997. [Online]. Available: http://books.google.com/books?id=iL0yrWK22-kC

[86] E. Loginova, N. C. Bartelt, P. J. Feibelman, and K. F. McCarty, "Evidence for graphene growth by C cluster attachment," *New Journal of Physics*, vol. 10, no. 9, p. 093026, 2008. [Online]. Available: http://stacks.iop.org/1367-2630/10/i=9/a=093026?key=crossref.50b4e4bdfb203c8a047d3ce8c03e8d15

[87] A. Zangwill and D. D. Vvedensky, "Novel growth mechanism of epitaxial graphene on metals," *Nano Letters*, vol. 11, no. 5, pp. 2092–2095, 2011. [Online]. Available: http://pubs.acs.org/doi/abs/10.1021/nl2006005

[88] V. Ramachandran, M. Brady, A. Smith, R. Feenstra, and D. Greve, "Preparation of atomically flat surfaces on silicon carbide using hydrogen etching," *Journal of Electronic Materials*, vol. 27, pp. 308–312, 1998, 10.1007/s11664-998-0406-7. [Online]. Available: http://dx.doi.org/10.1007/s11664-998-0406-7

[89] T. Doi, I. D. Marinescu, and S. Kurokawa, *Advances in CMP Polishing Technologies*. Oxford, UK: Elsevier, Inc., 2011.

[90] Z. Pei, G. R. Fisher, and J. Liu, "Grinding of silicon wafers: A review from historical perspectives," *International Journal of Machine Tools and*

Manufacture, vol. 48, no. 1213, pp. 1297 – 1307, 2008. [Online]. Available: http://www.sciencedirect.com/science/article/pii/S0890695508001089

[91] Z. Pei, S. Billingsley, and S. Miura, "Grinding induced subsurface cracks in silicon wafers," *International Journal of Machine Tools and Manufacture*, vol. 39, no. 7, pp. 1103–1116, 1999. [Online]. Available: http://www.sciencedirect.com/science/article/pii/S0890695598000790

[92] T. G. Bifano, T. A. Dow, and R. O. Scattergood, "Ductile-regime grinding: A new technology for machining brittle materials," *Journal of Manufacturing Science and Engineering*, vol. 113, no. 2, pp. 184–189, 1991. [Online]. Available: http://dx.doi.org/10.1115/1.2899676

[93] F. Ericson and J.-A. Schweitz, "Micromechanical fracture strength of silicon," *Journal of Applied Physics*, vol. 68, no. 11, pp. 5840–5844, 1990. [Online]. Available: http://link.aip.org/link/?JAP/68/5840/1

[94] J. Duan and D. Liu, "On the lapping mechanism of optical fiber end-surfaces using fixed diamond abrasive films," *Journal of manufacturing science and engineering*, vol. 133, no. 2, 2011.

[95] T. Bifano, Y. Yi, and K. Kahl, "Fixed abrasive grinding of CVD SiC mirrors," *Precision Engineering*, vol. 16, no. 2, pp. 109–116, 1994. [Online]. Available: http://www.sciencedirect.com/science/article/pii/0141635994901953

[96] M. R. Oliver, *Chemical-Mechanical Planarization of Semiconductor Materials*, 1st ed. Berlin: Springer, 2004.

[97] M. Forsberg, "Effect of process parameters on material removal rate in chemical mechanical polishing of $si(001)$," *Microelectronic Engineering*, vol. 77, no. 3 - 4, pp. 319 – 326, 2005. [Online]. Available: http://www.sciencedirect.com/science/article/pii/S0167931704005283

[98] H. Aida, T. Doi, H. Takeda, H. Katakura, S.-W. Kim, K. Koyama, T. Yamazaki, and M. Uneda, "Ultraprecision cmp for sapphire, gan, and SiC for advanced optoelectronics materials," *Current Applied Physics*, vol. 12, Supplement 2, pp. S41 – S46, 2012, proceedings of the Second International Symposium on Hybrid Materials and Processing Busan, Korea, 27-29 October 2011. [Online]. Available: http://www.sciencedirect.com/science/article/pii/S1567173912000454

[99] S. Jianxiu, D. Jiaxi, M. Lijie, Z. Zhuqing, and K. Renke, "Material removal rate of 6H-SiC crystal substrate CMP using an alumina (Al2O3) abrasive," *Journal of Semiconductors*, vol. 33, no. 10, p. 106003, 2012. [Online]. Available: http://iopscience.iop.org/1674-4926/33/10/106003

[100] H. Nitta, A. Isobe, t. J. Hong, and T. Hirao, "Research on reaction method of high removal rate chemical mechanical polishing slurry for 4H-SiC substrate," *Japanese Journal of Applied Physics*, vol. 50, no. 4, p. 046501, 2011. [Online]. Available: http://jjap.jsap.jp/link?JJAP/50/046501/

[101] P. Kuo and I. Currier, "Augmented CMP techniques for silicon carbide," *Materials Science Forum*, vol. 527-529, pp. 1099–1102, 2006. [Online]. Available: http://www.scientific.net/MSF.527-529.1099

[102] V. Borovikov and A. Zangwill, "Step bunching of vicinal $6\mathrm{H}-\mathrm{SiC}(0001)$ surfaces," *Physical Review B*, vol. 79, no. 24, p. 245413, 2009. [Online]. Available: http://link.aps.org/doi/10.1103/PhysRevB.79.245413

[103] J. Drowart, G. De Maria, and M. G. Inghram, "Thermodynamic study of SiC utilizing a mass spectrometer," *The Journal of Chemical Physics*, vol. 29, no. 5, pp. 1015–1021, 1958.

[104] S. G. Davis, D. F. Anthrop, and A. W. Searcy, "Vapor pressure of silicon and

the dissocation pressure of silicon carbide," *The Journal of Chemical Physics*, vol. 34, no. 2, pp. 659–664, 1961.

[105] S. Lilov, "Thermodynamic analysis of phase transformations at the dissociative evaporation of silicon carbide polytypes," *Diamond and Related Materials*, vol. 4, no. 12, pp. 1331–1334, 1995. [Online]. Available: http://linkinghub.elsevier.com/retrieve/pii/0925963595003126

[106] E. Williams and N. Bartelt, "Thermodynamics of surface morphology," *Science*, vol. 251, no. 4992, pp. 393–400, 1991. [Online]. Available: http://lib.semi.ac.cn:8080/tsh/dzzy/wsqk/science/vol251/251-393.pdf

[107] J. Lin, D. Y. Petrovykh, J. Viernow, F. K. Men, D. J. Seo, and F. J. Himpsel, "Formation of regular step arrays on Si(111) 7x7," *Journal of Applied Physics*, vol. 84, no. 1, pp. 255 – 260, 1998.

[108] F. Owman, C. Hallin, P. Mårtensson, and E. Janzén, "Removal of polishing-induced damage from 6H-SiC(0001) substrates by hydrogen etching," *Journal of Crystal Growth*, vol. 167, no. 1–2, pp. 391–395, 1996. [Online]. Available: http://www.sciencedirect.com/science/article/pii/0022024896002965

[109] J. B. Hannon and R. M. Tromp, "Pit formation during graphene synthesis on SiC(0001): In situ electron microscopy," *Physical Review B*, vol. 77, no. 24, pp. 1–4, 2008. [Online]. Available: http://link.aps.org/doi/10.1103/PhysRevB.77.241404

[110] T. Ohta, N. C. Bartelt, S. Nie, K. Thürmer, and G. L. Kellogg, "Role of carbon surface diffusion on the growth of epitaxial graphene on SiC," *Physical Review B*, vol. 81, no. 12, p. 121411, 2010. [Online]. Available: http://link.aps.org/doi/10.1103/PhysRevB.81.121411

[111] F. Varchon, P. Mallet, L. Magaud, and J.-Y. Veuillen, "Rotational disorder in few-layer graphene films on $6H-SiC(000\bar{1})$: A scanning tunneling microscopy study," *Physical Review B*, vol. 77, no. 16, p. 165415, 2008. [Online]. Available: http://link.aps.org/abstract/PRB/v77/e165415

[112] T. L. Chu and R. B. Campbell, "Chemical etching of silicon carbide with hydrogen," *Journal of The Electrochemical Society*, vol. 112, no. 9, pp. 955–956, 1965. [Online]. Available: http://jes.ecsdl.org/content/112/9/955.abstract

[113] C. L. Frewin, C. Coletti, C. Riedl, U. Starke, and S. E. Saddow, "A Comprehensive Study of Hydrogen Etching on the Major SiC Polytypes and Crystal Orientations," *Materials Science Forum*, vol. 615-617, pp. 589–592, 2009. [Online]. Available: http://www.scientific.net/MSF.615-617.589

[114] Z. Y. Xie, J. H. Edgar, B. K. Burkland, J. T. George, and J. Chaudhuri, "Dpbs-free and polytype controlled growth of SiC via surface etching on on-axis $6H-SiC(0001)$," *Journal of Crystal Growth*, vol. 224, no. 3-4, pp. 235–243, 2001. [Online]. Available: http://linkinghub.elsevier.com/retrieve/pii/S0022024801010247

[115] A. A. Burk and L. B. Rowland, "The role of excess silicon and in situ etching on $4H-SiC$ and $6H-SiC$ epitaxial layer morphology," *Journal of Crystal Growth*, vol. 167, pp. 586–595, 1996.

[116] Y. Ishida, T. Takahashi, H. Okumura, K. Arai, and S. Yoshida, "Origin of giant step bunching on $4H-SiC(0001)$ surfaces," *Materials Science Forum*, vol. 600-603, pp. 473–476, 2009. [Online]. Available: http://www.scientific.net/MSF.600-603.473

[117] J. M. Harris, H. C. Gatos, and A. F. Witt, "Etching characteristics of silicon

carbide in hydrogen," *Journal of The Electrochemical Society*, vol. 116, no. 3, pp. 380–383, 1969. [Online]. Available: http://jes.ecsdl.org/content/116/3/380

[118] S. Soubatch, S. E. Saddow, S. P. Rao, W. Lee, M. Konuma, and U. Starke, "Structure and morphology of 4H-SiC wafer surfaces after H_2-etching," in *Materials Science Forum*, vol. 483. Trans Tech Publications, 2005, pp. 761–764.

[119] M. Sprinkle, M. Ruan, Y. Hu, J. Hankinson, M. Rubio-Roy, B. Zhang, X. Wu, C. Berger, and W. A. d. Heer, "Scalable templated growth of graphene nanoribbons on SiC," *Nature Nanotechnology*, vol. 5, no. 10, pp. 727–731, 2010. [Online]. Available: http://www.nature.com/nnano/journal/v5/n10/full/nnano.2010.192.html

[120] X. Li, "Epitaxial graphene films on SiC: growth, characterization, and devices," Dissertation, Georgia Institute of Technology, 2008. [Online]. Available: http://hdl.handle.net/1853/24670

[121] J. R. Stephens and R. G. Garlick, "Compatibility of tantalum, columbium, and their alloys with hydrogen in presence of temperature gradient," NASA, Lewis Research Center, Cleveland, OH, Technical note ADA400423, 1966. [Online]. Available: http://www.dtic.mil/cgi-bin/GetTRDoc?Location=U2&doc=GetTRDoc.pdf&AD=ADA400423

[122] W. Wulfhekel, D. Sander, S. Nitsche, F. Dulot, A. Leycuras, and M. Hanbücken, "Regular step formation on concave-shaped surfaces on $6H-SiC(0001)$," *Surface Science*, vol. 550, no. 1 - 3, pp. 8 – 14, 2004. [Online]. Available: http://www.sciencedirect.com/science/article/pii/S0039602803015942

[123] W. Wulfhekel, D. Sander, S. Nitsche, F. Dulot, A. Leycuras, and M. Hanbücken, "Structural reorganisation of vicinal surfaces on 6H-SiC(0001) induced by hot hydrogen etching," *Applied Surface Science*, vol. 234, no.

14, pp. 251 – 255, 2004, ¡ce:title¿The Ninth International Conference on the Formation of Semiconductor Interfaces,¡/ce:title¿. [Online]. Available: http://www.sciencedirect.com/science/article/pii/S0169433204006609

[124] G. M. Rutter, "Private discussion," 2010.

[125] D. R. Lide, *CRC Handbook of Chemistry and Physics, 88th Edition (CRC Handbook of Chemistry & Physics)*, 88th ed. CRC Press, 2007. [Online]. Available: http://www.worldcat.org/isbn/0849304881

[126] A. B. Gokhale and G. J. Abbaschian, "The mo-si (molybdenum-silicon) system," *Journal of Phase Equilibria*, vol. 12, no. 4, pp. 493–498, 1991. [Online]. Available: http://link.springer.com/article/10.1007/BF02645979

[127] E. E. G. Hughes, B. R. Williams, and J. M. Thomas, "Etching of graphite surfaces with oxygen," *Transactions of the Faraday Society*, vol. 58, no. 0, pp. 2011–2016, 1962. [Online]. Available: http://pubs.rsc.org/en/content/articlelanding/1962/tf/tf9625802011

[128] V. Gorovenko, V. Knyazik, and A. Shteinberg, "High-temperature interaction between silicon and carbon," *Ceramics International*, vol. 19, no. 2, pp. 129 – 132, 1993. [Online]. Available: http://www.sciencedirect.com/science/article/pii/0272884293900867

[129] J. Zhang, L. Storasta, J. P. Bergman, N. T. Son, and E. Janzen, "Electrically active defects in n-type 4H silicon carbide grown in a vertical hot-wall reactor," *Journal of Applied Physics*, vol. 93, no. 8, pp. 4708–4714, 2003.

[130] J. W. Fergus and W. L. Worrell, "Silicon-carbide/boron-containing coatings for the oxidation protection of graphite," *Carbon*, vol. 33, no. 4, pp. 537–543, 1995. [Online]. Available: http://www.sciencedirect.com/science/article/pii/0008622394001783

[131] T. Li, "Characteristics of graphite films on silicon- and carbon-terminated faces of silicon carbide," Dissertation, Georgia Institute of Technology, 2006. [Online]. Available: http://hdl.handle.net/1853/14024

[132] G. M. Rutter, "Atomic scale properties of epitaxial graphene grown on SiC(0001)," Dissertation, Georgia Institute of Technology, 2008. [Online]. Available: http://hdl.handle.net/1853/26570

[133] J. R. Hass, J. Millán-Otoya, P. N. First, and E. H. Conrad, "Interface structure of epitaxial graphene grown on $4\mathrm{H}-\mathrm{SiC}(000\bar{1})$," *Physical Review B*, vol. 78, no. 20, pp. 1–10, 2008. [Online]. Available: http://link.aps.org/doi/10.1103/PhysRevB.78.205424

[134] N. Sharma, "Microscopic and spectroscopic studies of growth and electronic structure of epitaxial graphene," Dissertation, Georgia Institute of Technology, 2009.

[135] B. G. Liptak, *Instrument Engineers' Handbook, Fourth Edition, Volume One: Process Measurement and Analysis.* CRC Press, 2003.

[136] N. Miloevi, G. S. Vukovi, D. Z. Pavii, and K. D. Magli, "Thermal properties of tantalum between 300 and 2300 k," *International Journal of Thermophysics*, vol. 20, no. 4, pp. 1129–1136, 1999. [Online]. Available: http://link.springer.com/article/10.1023/A%3A1022659005050

[137] D. L. Miller, K. D. Kubista, G. M. Rutter, M. Ruan, W. A. de Heer, P. N. First, and J. A. Stroscio, "Structural analysis of multilayer graphene via atomic moiré interferometry," *Physical Review B*, vol. 81, p. 125427, 2010. [Online]. Available: http://link.aps.org/doi/10.1103/PhysRevB.81.125427

[138] M. Sprinkle, "Epitaxial graphene on silicon carbide: low-vacuum growth, characterization, and device fabrication," Dissertation, Georgia Institute of Technology, 2010.

[139] L. E. Davis, N. C. MacDonald, P. W. Palmberg, and G. Riach, *Handbook of Auger Electron Spectroscopy*, 2nd ed. Chanhassen, MN: Physical Electronics Industries, Inc., 1978.

[140] D. Woodruff and T. Delchar, *Modern Techniques of Surface Science*, ser. Cambridge Solid State Science Series. Cambridge University Press, 1994. [Online]. Available: http://books.google.com/books?id=oSirgCsfQ6AC

[141] A. Einstein, "Über einen die erzeugung und verwandlung des lichtes betreffenden heuristischen gesichtspunkt," *Annalen der Physik*, vol. 322, no. 6, pp. 132–148, 1905. [Online]. Available: http://dx.doi.org/10.1002/andp.19053220607

[142] D. Briggs and P. Seah, *Practical Surface Analysis: Auger and X-ray photoelectron spectroscopy*, ser. Practical Surface Analysis. Wiley, 1990. [Online]. Available: http://books.google.com/books?id=D9pTAAAAMAAJ

[143] J. Goldstein, *Scanning Electron Microscopy and X-Ray Microanalysis*. Springer London, Limited, 2003. [Online]. Available: http://books.google.com/books?id=ruF9DQxCDLQC

[144] G. P. Thomson and A. Reid, "Diffraction of cathode rays by a thin film," *Nature*, vol. 119, p. 890, 1927.

[145] C. Davisson and L. H. Germer, "Diffraction of electrons by a crystal of nickel," *Physical Review*, vol. 30, no. 6, p. 705, 1927.

[146] I. Estermann and O. Stern, "Beugung von molekularstrahlen," *Zeitschrift für Physik*, vol. 61, no. 1-2, pp. 95–125, 1930. [Online]. Available: http://link.springer.com/article/10.1007/BF01340293

[147] W. Friedrich, P. Knipping, and M. von Laue, "Interferenz-erscheinungen bei röntgenstrahlen," *Sitzungsberichte der Mathematisch-Physikalischen Classe der Königlich-Bayerischen Akademie der Wissenschaften zu Mnchen*, p. 303, 1912.

[148] J. R. Levine, J. B. Cohen, Y. W. Chung, and P. Georgopoulos, "Grazing-incidence small-angle x-ray scattering: new tool for studying thin film growth," *Journal of Applied Crystallography*, vol. 22, no. 6, pp. 528–532, 1989. [Online]. Available: http://dx.doi.org/10.1107/S002188988900717X

[149] C. G. Shull, "Early development of neutron scattering," *Reviews of Modern Physics*, vol. 67, pp. 753–757, 1995. [Online]. Available: http://link.aps.org/doi/10.1103/RevModPhys.67.753

[150] M. F. Tompsett and C. W. B. Grigson, "Reflection scanning electron diffraction with energy filtering," *Journal of Scientific Instruments*, vol. 43, no. 7, p. 430, 1966. [Online]. Available: http://stacks.iop.org/0950-7671/43/i=7/a=303

[151] P. Auger, "Sur l'effet photoélectrique composé," *Journal de Physique et le Radium*, vol. 6, no. 6, pp. 205–208, 1925. [Online]. Available: http://dx.doi.org/10.1051/jphysrad:0192500606020500

[152] W. C. Michels and N. L. Curtis, "A pentode lock-in amplifier of high frequency selectivity," *Review of Scientific Instruments*, vol. 12, no. 9, pp. 444–447, 1941. [Online]. Available: http://rsi.aip.org/resource/1/rsinak/v12/i9/p444_s1

[153] D. H. Narumand and K. D. Childs, "Auger spectrometers: A tutorial review," *Applied Spectroscopy Reviews*, vol. 34, no. 3, pp. 139–158, 2004. [Online]. Available: http://www.tandfonline.com/doi/abs/10.1081/ASR-100100842

[154] J. C. Weber, J. B. Schlager, N. A. Sanford, A. Imtiaz, T. M. Wallis, L. M. Mansfield, K. J. Coakley, K. A. Bertness, P. Kabos, and V. M. Bright, "A near-field scanning microwave microscope for characterization of inhomogeneous photovoltaics," *Review of Scientific Instruments*, vol. 83, no. 8, p. 083702, 2012. [Online]. Available: http://link.aip.org/link/?RSI/83/083702/1

[155] G. Binnig, H. Rohrer, C. Gerber, and E. Weibel, "Surface studies by scanning tunneling microscopy," *Physical Review Letters*, vol. 49, no. 1, pp. 57–61, 1982. [Online]. Available: http://link.aps.org/doi/10.1103/PhysRevLett.49.57

[156] G. Binnig and H. Rohrer, "Scanning tunneling microscopy," *Surface Science*, vol. 126, no. 13, pp. 236–244, 1983. [Online]. Available: http://www.sciencedirect.com/science/article/pii/0039602883907161

[157] G. Binnig, H. Rohrer, C. Gerber, and E. Weibel, "7×7 reconstruction on Si(111) resolved in real," *Physical Review Letters*, vol. 50, no. 2, pp. 120–123, 1983. [Online]. Available: http://link.aps.org/doi/10.1103/PhysRevLett.50.120

[158] G. Binnig, H. Rohrer, C. Gerber, and E. Weibel, "Tunneling through a controllable vacuum gap," *Applied Physics Letters*, vol. 40, no. 2, pp. 178–180, 1982. [Online]. Available: http://apl.aip.org/resource/1/applab/v40/i2/p178_s1?isAuthorized=no

[159] G. Binnig and H. Rohrer, "Scanning tunneling microscopy - from birth to adolescence," *Reviews of Modern Physics*, vol. 59, no. 3, pp. 615–625, 1987. [Online]. Available: http://link.aps.org/doi/10.1103/RevModPhys.59.615

[160] C. C. M. Mody, *Discovering The Nanoscale.* Amsterdam, The Netherlands: IOS Press, Inc., 2004, ch. How Probe Microscopists Became Nanotechnologists, pp. 119 – 134. [Online]. Available: http://books.google.com/books?id=O-LM6eWUbmIC

[161] G. Binnig, C. F. Quate, and C. Gerber, "Atomic force microscope," *Physical Review Letters*, vol. 56, pp. 930–933, 1986. [Online]. Available: http://link.aps.org/doi/10.1103/PhysRevLett.56.930

[162] H.-J. Butt, B. Cappella, and M. Kappl, "Force measurements with the atomic force microscope: Technique, interpretation and applications," *Surface Science Reports*, vol. 59, no. 1, pp. 1–152, 2005.

[163] P. M. Vilarinho, Y. Rosenwaks, and A. I. Kingon, *Scanning Probe Microscopy: Characterization, Nanofabrication and Device Application of Functional Materials*. Springer, 2005.

[164] M. J. Higgins, T. Fukuma, and S. P. Jarvis, "AFM in liquid," *Imaging & Microscopy*, vol. 8, no. 3, p. 4749, 2006. [Online]. Available: http://onlinelibrary.wiley.com.prx.library.gatech.edu/doi/10.1002/imic.200790097/abstract

[165] J. R. Matey and J. Blanc, "Scanning capacitance microscopy," *Journal of Applied Physics*, vol. 57, no. 5, pp. 1437–1444, 1985. [Online]. Available: http://jap.aip.org/resource/1/japiau/v57/i5/p1437_s1?isAuthorized=no

[166] D. Pohl, *Near-Field Optics and Surface Plasmon Polaritons*. Würzburg, Germany: Springer, 2001, ch. Introduction, pp. 1 – 13.

[167] G. Gamow, "Zur quantentheorie des atomkernes," *Zeitschrift fr Physik*, vol. 51, pp. 204 – 212, 1928.

[168] O. Nairz, M. Arndt, and A. Zeilinger, "Quantum interference experiments with large molecules," *American Journal of Physics*, vol. 71, no. 4, p. 319, 2003. [Online]. Available: http://link.aip.org/link/AJPIAS/v71/i4/p319/s1&Agg=doi

[169] A. D. O'Connell, M. Hofheinz, M. Ansmann, R. C. Bialczak, M. Lenander, E. Lucero, M. Neeley, D. Sank, H. Wang, M. Weides, J. Wenner, J. M. Martinis, and A. N. Cleland, "Quantum ground state and single-phonon control of a mechanical resonator," *Nature*, vol. 464, no. 7289, pp. 697–703, 2010. [Online]. Available: http://www.nature.com/nature/journal/v464/n7289/full/nature08967.html

[170] E. Fermi, "Versuch einer theorie der -strahlen. i," *Zeitschrift für Physik*, vol. 88, pp. 161–177, 1934. [Online]. Available: http://dx.doi.org/10.1007/BF01351864

[171] F. L. Wilson, "Fermi's theory of beta decay," *American Journal of Physics*, vol. 36, no. 12, p. 1150, 1968. [Online]. Available: http://link.aip.org/link/?AJP/36/1150/1&Agg=doi

[172] R. J. McMahon, "Chemical reactions involving quantum tunneling," *Science*, vol. 299, no. 5608, pp. 833–834, 2003. [Online]. Available: http://www.sciencemag.org/content/299/5608/833

[173] E. Hückel, "Quantentheoretische beitrge zum benzolproblem," *Zeitschrift für Physik*, vol. 70, pp. 204–286, 1931. [Online]. Available: http://dx.doi.org/10.1007/BF01339530

[174] R. H. Fowler and L. Nordheim, "Electron emission in intense electric fields," *Proceedings of the Royal Society of London. Series A*, vol. 119, no. 781, pp. 173–181, 1928. [Online]. Available: http://rspa.royalsocietypublishing.org/content/119/781/173

[175] P. J. Price, "Electron tunneling in solids," *Physics Today*, vol. 15, no. 4, pp. 19–24, 1962. [Online]. Available: http://link.aip.org/link/?PTO/15/19/1

[176] L. Esaki, "New phenomenon in narrow germanium p-n junctions,"

Physical Review, vol. 109, no. 2, pp. 603–604, 1958. [Online]. Available: http://link.aps.org/doi/10.1103/PhysRev.109.603

[177] J. G. Simmons, "Electric tunnel effect between dissimilar electrodes separated by a thin insulating film," *Journal of Applied Physics*, vol. 34, no. 9, pp. 2581–2590, 1963. [Online]. Available: http://link.aip.org/link/?JAP/34/2581/1

[178] J. G. Simmons, "Generalized formula for the electric tunnel effect between similar electrodes separated by a thin insulating film," *Journal of Applied Physics*, vol. 34, no. 6, pp. 1793–1803, 1963. [Online]. Available: http://link.aip.org/link/?JAP/34/1793/1

[179] T. E. Hartman, "Tunneling through asymmetric barriers," *Journal of Applied Physics*, vol. 35, no. 11, pp. 3283–3294, 1964. [Online]. Available: http://link.aip.org/link/?JAP/35/3283/1

[180] T. E. Hartman and J. S. Chivian, "Electron tunneling through thin aluminum oxide films," *Physical Review*, vol. 134, pp. A1094–A1101, 1964. [Online]. Available: http://link.aps.org/doi/10.1103/PhysRev.134.A1094

[181] J. Stroscio and W. Kaiser, *Scanning Tunneling Microscopy*, ser. Methods of Experimental Physics. Elsevier Science, 1993. [Online]. Available: http://books.google.com/books?id=MtHq0mgF5WgC

[182] J. Tersoff and D. R. Hamann, "Theory and application for the scanning tunneling microscope," *Physical Review Letters*, vol. 50, pp. 1998–2001, 1983. [Online]. Available: http://link.aps.org/doi/10.1103/PhysRevLett.50.1998

[183] J. Bardeen, "Tunnelling from a many-particle point of view," *Physical Review Letters*, vol. 6, pp. 57–59, 1961. [Online]. Available: http://link.aps.org/doi/10.1103/PhysRevLett.6.57

[184] J. Tersoff, "Role of tip electronic structure in scanning tunneling microscope images," *Physical Review B*, vol. 41, no. 2, pp. 1235–1238, 1990. [Online]. Available: http://link.aps.org/doi/10.1103/PhysRevB.41.1235

[185] C. J. Chen, "Theory of scanning tunneling spectroscopy," *Journal of Vacuum Science & Technology A: Vacuum, Surfaces, and Films*, vol. 6, no. 2, pp. 319–322, 1988. [Online]. Available: http://link.aip.org/link/?JVA/6/319/1

[186] L. Gross, N. Moll, F. Mohn, A. Curioni, G. Meyer, F. Hanke, and M. Persson, "High-resolution molecular orbital imaging using a *p*-wave stm tip," *Physical Review Letters*, vol. 107, p. 086101, 2011. [Online]. Available: http://link.aps.org/doi/10.1103/PhysRevLett.107.086101

[187] A. Cricenti and R. Generosi, "Air operating atomic force-scanning tunneling microscope suitable to study semiconductors, metals, and biological samples," *Review of Scientific Instruments*, vol. 66, no. 4, pp. 2843–2847, 1995. [Online]. Available: http://rsi.aip.org.prx.library.gatech.edu/resource/1/rsinak/v66/i4/p2843_s1?isAuthorized=no

[188] S. Morita, I. Otsuka, and N. Mikoshiba, "Scanning tunneling microscopy in air and liquid," *Physica Scripta*, vol. 38, no. 2, p. 277, 1988. [Online]. Available: http://iopscience.iop.org/1402-4896/38/2/033

[189] L. A. Nagahara, T. Thundat, and S. M. Lindsay, "Preparation and characterization of STM tips for electrochemical studies," *Review of Scientific Instruments*, vol. 60, no. 10, pp. 3128–3130, 1989. [Online]. Available: http://rsi.aip.org.prx.library.gatech.edu/resource/1/rsinak/v60/i10/p3128_s1?isAuthorized=no

[190] R. Heinz, A. Stabel, F. C. De Schryver, and J. P. Rabe, "Ostwald ripening of two-dimensional crystals at the solid-liquid interface," *The Journal of*

Physical Chemistry, vol. 99, no. 2, pp. 505–507, 1995. [Online]. Available: http://dx.doi.org/10.1021/j100002a009

[191] A. J. Melmed, "The art and science and other aspects of making sharp tips," *Journal of Vacuum Science & Technology B: Microelectronics and Nanometer Structures*, vol. 9, no. 2, p. 601, 1991. [Online]. Available: http://avspublications.org.www.library.gatech.edu:2048/jvstb/resource/1/jvtbd9/v9/i2/p601_s1

[192] A. J. Nam, "Benign making of sharp tips for STM and FIM: pt, ir, au, pd, and rh," *Journal of Vacuum Science & Technology B: Microelectronics and Nanometer Structures*, vol. 13, no. 4, p. 1556, 1995. [Online]. Available: http://avspublications.org.www.library.gatech.edu:2048/jvstb/resource/1/jvtbd9/v13/i4/p1556_s1

[193] A. A. Vives and A. Arnau, *Piezoelectric Transducers and Applications*. Springer, 2008.

[194] G. Binnig and D. P. E. Smith, "Single-tube three-dimensional scanner for scanning tunneling microscopy," *Review of Scientific Instruments*, vol. 57, no. 8, pp. 1688–1689, 1986. [Online]. Available: http://rsi.aip.org/resource/1/rsinak/v57/i8/p1688_s1?isAuthorized=no

[195] K. Uchino, *Piezoelectric Actuators and Ultrasonic Motors*. Norwell, MA, USA: Springer, 1997.

[196] M. E. Taylor, "Dynamics of piezoelectric tube scanners for scanning probe microscopy," *Review of Scientific Instruments*, vol. 64, no. 1, pp. 154–158, 1993. [Online]. Available: http://rsi.aip.org.prx.library.gatech.edu/resource/1/rsinak/v64/i1/p154_s1?isAuthorized=no

[197] R. A. Bizzigotti, "Electromechanical translation apparatus," U.S. Patent 3 902 085, 1975, U.S. Classification: 310/328; 310/25; 310/26; 310/369; 318/135. [Online]. Available: http://www.google.com/patents?id=SDw8AAAAEBAJ

[198] W. G. May, "Piezoelectric electromechanical translation apparatus," U.S. Patent 3 902 084, 1975, U.S. Classification: 310/328; 310/26; 310/315; 310/317; 318/116; 318/118; 318/135. [Online]. Available: http://www.google.com/patents?id=Rzw8AAAAEBAJ

[199] A. W. Hartman, "Piezoelectric inchworm operation in a vacuum," *Optical Engineering*, vol. 17, no. 6, pp. 176 645–176 645, 1978. [Online]. Available: http://dx.doi.org/10.1117/12.7972297

[200] K. Besocke, "An easily operable scanning tunneling microscope," *Surface Science*, vol. 181, no. 12, pp. 145–153, 1987. [Online]. Available: http://www.sciencedirect.com/science/article/pii/0039602887901518

[201] J. Frohn, J. F. Wolf, K. Besocke, and M. Teske, "Coarse tip distance adjustment and positioner for a scanning tunneling microscope," *Review of Scientific Instruments*, vol. 60, no. 6, pp. 1200–1201, 1989. [Online]. Available: http://rsi.aip.org.prx.library.gatech.edu/resource/1/rsinak/v60/i6/p1200_s1?isAuthorized=no

[202] B. Drevniok, W. M. P. Paul, K. R. Hairsine, and A. B. McLean, "Methods and instrumentation for piezoelectric motors," *Review of Scientific Instruments*, vol. 83, no. 3, pp. 033 706–033 706–6, 2012. [Online]. Available: http://rsi.aip.org.prx.library.gatech.edu/resource/1/rsinak/v83/i3/p033706_s1?isAuthorized=no

[203] Y. J. Song, A. F. Otte, V. Shvarts, Z. Zhao, Y. Kuk, S. R. Blankenship, A. Band, F. M. Hess, and J. A. Stroscio, "Invited review article: A 10 mK

scanning probe microscopy facility," *Review of Scientific Instruments*, vol. 81, no. 12, pp. 121 101–121 133, 2010. [Online]. Available: http://rsi.aip.org.prx.library.gatech.edu/resource/1/rsinak/v81/i12/p121101_s1?isAuthorized=no

[204] P. e. Quesenberry, "Scanning tunneling microscopy studies fo a reactive interface, ni/gaas," Dissertation, Georgia Institute of Technology, 1996.

[205] A. J. V. Bommel, J. Crombeen, and A. V. Tooren, "Leed and auger electron observations of the SiC(0001) surface," *Surface Science*, vol. 48, no. 2, pp. 463 – 472, 1975. [Online]. Available: http://www.sciencedirect.com/science/article/pii/0039602875904197

[206] F. Owman and P. Mårtensson, "Stm study of the sic(0001) $\sqrt(3) \times \sqrt(3)$ surface," *Surface Science*, vol. 330, no. 1, pp. L639–L645, 1995. [Online]. Available: http://www.sciencedirect.com/science/article/pii/0039602895004270

[207] F. Owman and P. Mårtensson, "Scanning tunneling microscopy study of SiC(0001) surface reconstructions," *Journal of Vacuum Science & Technology B*, vol. 14, pp. 933–937, 1996. [Online]. Available: http://link.aip.org/link/?JVB/14/933/1

[208] I. Forbeaux, J.-M. Themlin, and J.-M. Debever, "Heteroepitaxial graphite on $6\mathrm{H}-\mathrm{SiC}(0001)$: Interface formation through conduction-band electronic structure," *Physical Review B*, vol. 58, pp. 16 396–16 406, 1998. [Online]. Available: http://link.aps.org/doi/10.1103/PhysRevB.58.16396

[209] I. Forbeaux, J.-M. Themlin, A. Charrier, F. Thibaudau, and J.-M. Debever, "Solid-state graphitization mechanisms of silicon carbide $6H - SiC$ polar faces," *Applied Surface Science*, vol. 162163, pp. 406–412,

2000. [Online]. Available: http://www.sciencedirect.com/science/article/pii/S0169433200002245

[210] A. Charrier, A. Coati, T. Argunova, F. Thibaudau, Y. Garreau, R. Pinchaux, I. Forbeaux, J. Debever, M. Sauvage-Simkin, and J. Themlin, "Solid-state decomposition of silicon carbide for growing ultra-thin heteroepitaxial graphite films," *Journal of Applied Physics*, vol. 92, no. 5, pp. 2479–2484, 2002.

[211] G. Dhanaraj, K. Byrappa, V. Prasad, and M. Dudley, *Springer Handbook of Crystal Growth*, ser. Springer Handbooks. Würzburg, Germany: Springer Science+Business Media, Incorporated, 2010. [Online]. Available: http://books.google.com/books?id=izaSIlOahJkC

[212] J. Tersoff, M. D. Johnson, and B. G. Orr, "Adatom densities on gaas: Evidence for near-equilibrium growth," *Physical Review Letters*, vol. 78, pp. 282–285, 1997. [Online]. Available: http://link.aps.org/doi/10.1103/PhysRevLett.78.282

[213] S. Oida, F. R. McFeely, J. B. Hannon, R. M. Tromp, M. Copel, Z. Chen, Y. Sun, D. B. Farmer, and J. Yurkas, "Decoupling graphene from SiC(0001) via oxidation," *Physical Review B*, vol. 82, no. 4, p. 041411, 2010.

[214] C. Chatillon, P. Rocabois, and C. Bernard, "High-temperature analysis of the thermal degradation of silicon-based materials. i: Binary si - o, si - c, and si -n compounds." *High Temperatures - High Pressures*, vol. 31, pp. 413–432, 1999.

[215] M. P. Seah, "Quantitative auger electron spectroscopy and electron ranges," *Surface Science*, vol. 32, no. 3, pp. 703–728, 1972. [Online]. Available: http://linkinghub.elsevier.com/retrieve/pii/0039602872901963

[216] P. J. Cumpson and M. P. Seah, "Elastic scattering corrections in aes and xps. ii. estimating attenuation lengths and conditions required

for their valid use in overlayer/substrate experiments," *Surface and Interface Analysis*, vol. 25, no. 6, pp. 430–446, 1997. [Online]. Available: http://doi.wiley.com/10.1002/\%28SICI\%291096-9918\%28199706\%2925\%3A6\%3C430\%3A\%3AAID-SIA254\%3E3.0.CO\%3B2-7

[217] C. C. Chang, "General formalism for quantitative auger analysis," *Surface Science*, vol. 48, no. 1, pp. 9–21, 1975.

[218] R. Payling, "Modified elemental sensitivity factors for auger electron spectroscopy," *Journal of Electron Spectroscopy and Related Phenomena*, vol. 36, pp. 99–104, 1985.

[219] P. W. Palmberg, "Quantitative auger electron spectroscopy using elemental sensitivity factors," *Journal of Vacuum Science and Technology*, vol. 13, no. 1, pp. 214–218, 1976. [Online]. Available: http://link.aip.org/link/?JVS/13/214/1

[220] Luxmi, N. Srivastava, R. M. Feenstra, and P. J. Fisher, "Formation of epitaxial graphene on SiC(0001) using vacuum or argon environments," *Journal of Vacuum Science & Technology B: Microelectronics and Nanometer Structures*, vol. 28, no. 4, p. C5C1, 2010. [Online]. Available: http://avspublications.org/jvstb/resource/1/jvtbd9/v28/i4/pC5C1_s1?isAuthorized=no

[221] S. Mroczkowski and D. Lichtman, "Calculated auger sensitivity factors compared to experimental handbook values," *Surface Science*, vol. 131, pp. 159–166, 1983.

[222] R. Payling, "Semi-empirical elemental sensitivities for quantitative auger electron spectroscopic analysis," *Journal of Electron Spectroscopy and Related Phenomena*, vol. 37, pp. 225–239, 1985.

[223] G. Leveque, "Quantitative correction of backscattering in auger electron spectroscopy of thin films," *Applied Surface Science*, vol. 89, no. 2, pp.

211–219, 1995. [Online]. Available: http://linkinghub.elsevier.com/retrieve/pii/0169433295000372

[224] S. Tanuma, C. J. Powell, and D. R. Penn, "Calculations of electron inelastic mean free paths. IX. data for 41 elemental solids over the 50 eV to 30 keV range," *Surface and Interface Analysis*, vol. 43, no. 3, p. 689713, 2011. [Online]. Available: http://onlinelibrary.wiley.com/doi/10.1002/sia.3522/abstract

[225] A. Jablonski, "Relationships between electron inelastic mean free paths, effective attenuation lengths, and mean escape depths," *Journal of Electron Spectroscopy and Related Phenomena*, vol. 100, no. 1-3, pp. 137–160, 1999. [Online]. Available: http://linkinghub.elsevier.com/retrieve/pii/S0368204899000444

[226] A. Jablonski and C. J. Powell, "The electron attenuation length revisited," *Surface Science Reports*, vol. 47, pp. 33–91, 2002.

[227] C. J. Powell, "Inelastic mean free paths and attenuation lengths of low-energy electrons in solids," *Scanning Electron Microscopy*, vol. 4, pp. 1649 – 1664, 1984.

[228] A. Jablonski and H. Ebel, "Comparison of electron attenuation lengths and escape depths with inelastic mean free paths," *Surface and Interface Analysis*, vol. 11, no. 12, p. 627632, 1988. [Online]. Available: http://onlinelibrary.wiley.com/doi/10.1002/sia.740111208/abstract

[229] C. J. Powell, A. Jablonski, and F. Salvat, "NIST databases with electron elastic-scattering cross sections, inelastic mean free paths, and effective attenuation lengths," *Surface and Interface Analysis*, vol. 37, no. 11, pp. 1068 – 1071, 2005. [Online]. Available: http://onlinelibrary.wiley.com/doi/10.1002/sia.2098/abstract

[230] C. J. Powell and A. Jablonski, *NIST Electron Effective-Attenuation-Length Database, Version 1.3, SRD82*. Gaithersburg, MD: National Institute of Standards and Technology, 2011, vol. Version 1.3.

[231] I. Tilinin, A. Jablonski, J. Zemek, and S. Hucek, "Escape probability of signal photoelectrons from non-crystalline solids: influence of anisotropy of photoemission," *Journal of Electron Spectroscopy and Related Phenomena*, vol. 87, no. 2, pp. 127–140, 1997. [Online]. Available: http://www.sciencedirect.com/science/article/pii/S0368204897000868

[232] S. Tanuma, C. J. Powell, and D. R. Penn, "Calculations of electron inelastic mean free paths III. data for 1 inorganic compounds over the 50-2000 ev range," *Surface and Interface Analysis*, vol. 17, pp. 927–939, 1991.

[233] S. Tanuma, T. Shiratori, T. Kimura, K. Goto, S. Ichimura, and C. J. Powell, "Experimental determination of electron inelastic mean free paths in 13 elemental solids in the 50 to 5000 ev energy range by elastic-peak electron spectroscopy," *Surface and Interface Analysis*, vol. 37, no. 11, pp. 833–845, 2005. [Online]. Available: http://doi.wiley.com/10.1002/sia.2102

[234] M. Xu, D. Fujita, J. Gao, and N. Hanagata, "Auger electron spectroscopy: A rational method for determining thickness of graphene films." *ACS Nano*, vol. 25, no. 5, pp. 2937–2945, 2010. [Online]. Available: http://www.ncbi.nlm.nih.gov/pubmed/20373812

[235] S. Tanuma, C. J. Powell, and D. R. Penn, "Calculations of electron inelastic mean free paths II. data for 27 elements over the 50-2000 ev range," *Surface and Interface Analysis*, vol. 17, pp. 911–926, 1991.

[236] M. Krawczyk, L. Zommer, A. Kosinski, J. W. Sobczak, and A. Jablonski, "Measured electron IMFPs for SiC," *Surface and Interface Analysis*, vol. 38, pp. 644–647, 2006.

[237] M. Krawczyk, "Quantification of surface excitation effects on the epes-determined imfps for gan and sic," *Surface and Interface Analysis*, vol. 40, pp. 725–727, 2008.

[238] S. Tanuma, C. J. Powell, and D. R. Penn, "Calculations of electron inelastic mean free paths. V. data for 14 organic compounds over the 50-2000 ev range," *Surface and Interface Analysis*, vol. 21, no. 3, pp. 165–176, 1994. [Online]. Available: http://dx.doi.org/10.1002/sia.740210302

[239] G. M. Rutter, N. P. Guisinger, J. N. Crain, E. A. A. Jarvis, M. D. Stiles, T. Li, P. N. First, and J. A. Stroscio, "Imaging the interface of epitaxial graphene with silicon carbide via scanning tunneling microscopy," *Physical Review B*, vol. 76, p. 235416, 2007.

[240] F. Speck, M. Ostler, J. Röhrl, J. Jobst, D. Waldmann, M. Hundhausen, L. Ley, H. B. Weber, and T. Seyller, "Quasi-freestanding graphene on SiC(0001)," in *Materials Science Forum*, ser. Silicon Carbide and Related Materials 2009, vol. 645–648, 2009, pp. 629–632.

[241] J. Hass, R. Feng, J. E. Millàn-Otoya, X. Li, M. Sprinkle, P. N. First, W. A. de Heer, E. H. Conrad, and C. Berger, "Structural properties of the multilayer graphene/ $4H-SiC(000\bar{1})$ system as determined by surface x-ray diffraction," *Physical Review B*, vol. 75, no. 21, p. 214109, 2007. [Online]. Available: http://link.aps.org/doi/10.1103/PhysRevB.75.214109

[242] R. M. Tromp and J. B. Hannon, "Thermodynamics and kinetics of graphene

growth on SiC(0001)," *Physical Review Letters*, vol. 102, no. 10, p. 106104, 2009. [Online]. Available: http://dx.doi.org/10.1103/PhysRevLett.102.106104

[243] N. Srivastava, G. He, Luxmi, P. C. Mende, R. M. Feenstra, and Y. Sun, "Graphene formed on SiC under various environments: comparison of si-face and c-face," *Journal of Physics D: Applied Physics*, vol. 45, no. 15, p. 154001, 2012. [Online]. Available: http://iopscience.iop.org/0022-3727/45/15/154001

[244] J. Bernhardt, M. Nerding, U. Starke, and K. Heinz, "Stable surface reconstructions on $6\mathrm{H}-\mathrm{SiC}(000\bar{1})$," *Materials Science and Engineering B*, vol. B61-62, pp. 207–211, 1999.

[245] K. L. Wallis, J. K. Patyk, and T. W. Zerda, "Reaction kinetics of nanostructured siliconcarbide," *Journal of Physics: Condensed Matter*, vol. 20, no. 32, p. 325216, 2008. [Online]. Available: http://stacks.iop.org/0953-8984/20/i=32/a=325216

[246] G. Muller-Vogt and W. Wendl, "Reaction kinetics in the determination of silicon by graphite furnace atomic absorption spectrometry," *Analytical Chemistry*, vol. 53, no. 4, pp. 651–653, 1981. [Online]. Available: http://pubs.acs.org/doi/abs/10.1021/ac00227a019

[247] W. A. de Heer, "Private discussion." 2013.

[248] M. Knudsen, "Die maximale verdampfungsgeschwindigkeit des quecksilbers," *Annalen der Physik*, vol. 352, no. 13, pp. 697–708, 1915. [Online]. Available: http://dx.doi.org/10.1002/andp.19153521306

[249] S. Chapman and T. G. Cowling, *The mathematical theory of non-uniform gases*, 3rd ed. Cambridge: Cambridge University Press, 1990. [Online]. Available: http://www.worldcat.org/oclc/55600801

[250] P. J. A. M. Kerkhof, "New light on some old problems: Revisiting the stefan tube, grahams law, and the bosanquet equation," *Industrial & Engineering Chemistry Research*, vol. 36, no. 3, pp. 915–922, 1997. [Online]. Available: http://pubs.acs.org/doi/abs/10.1021/ie960542i

[251] R. Krishna and J. M. van Baten, "Investigating the validity of the bosanquet formula for estimation of diffusivities in mesopores," *Chemical Engineering Science*, vol. 69, no. 1, pp. 684–688, 2012. [Online]. Available: http://www.sciencedirect.com/science/article/pii/S0009250911008256

[252] W. Steckelmacher, "The effect of cross-sectional shape on the molecular flow in long tubes," *Vacuum*, vol. 28, no. 6-7, pp. 269–275, 1978. [Online]. Available: http://linkinghub.elsevier.com/retrieve/pii/0042207X78900167

[253] D. Turner, "A mathematical analysis of a thermal transpiration vacuum pump," *Vacuum*, vol. 16, no. 8, pp. 413–419, 1966. [Online]. Available: http://linkinghub.elsevier.com/retrieve/pii/0042207X66914291

[254] P. J. Fisher, Luxmi, N. Srivastava, S. Nie, and R. M. Feenstra, "Thickness monitoring of graphene on SiC using low-energy electron diffraction," *Journal of Vacuum Science & Technology A: Vacuum, Surfaces, and Films*, vol. 28, no. 4, p. 958, 2010. [Online]. Available: http://avspublications.org/jvsta/resource/1/jvtad6/v28/i4/p958_s1?isAuthorized=no

[255] J. Hass, F. Varchon, J. Millán-Otoya, M. Sprinkle, N. Sharma, W. de Heer, C. Berger, P. First, L. Magaud, and E. Conrad, "Why multilayer graphene on $4H-SiC(000\bar{1})$ behaves like a single sheet of graphene," *Physical Review Letters*, vol. 100, no. 12, pp. 3–6, 2008. [Online]. Available: http://link.aps.org/doi/10.1103/PhysRevLett.100.125504

[256] J. R. Hass, W. A. de Heer, and E. H. Conrad, "The growth

and morphology of epitaxial multilayer graphene," *Journal of Physics: Condensed Matter*, vol. 20, no. 32, p. 323202, 2008. [Online]. Available: http://stacks.iop.org/0953-8984/20/323202

[257] M. Sprinkle, J. Hicks, A. Tejeda, A. Taleb-Ibrahimi, P. L. Fèvre, F. Bertran, H. Tinkey, M. C. Clark, P. Soukiassian, D. Martinotti, J. Hass, and E. H. Conrad, "Multilayer epitaxial graphene grown on the (SiC(000$\bar{1}$) surface; structure and electronic properties," *Journal of Physics D: Applied Physics*, vol. 43, no. 37, p. 374006, 2010. [Online]. Available: http://iopscience.iop.org/0022-3727/43/37/374006

[258] P. J. Luxmi, Fisher, N. Srivastava, R. M. Feenstra, Y. Sun, J. Kedzierski, P. Healey, and G. Gu, "Morphology of graphene on SiC(000$\bar{1}$) surfaces," *Applied Physics Letters*, vol. 95, no. 7, p. 073101, 2009. [Online]. Available: http://link.aip.org/link/APPLAB/v95/i7/p073101/s1\&Agg=doi

[259] V. Borovikov and A. Zangwill, "Step-edge instability during epitaxial growth of graphene from SiC(0001)," *Physical Review B*, vol. 80, p. 121406(R), 2009. [Online]. Available: http://prb.aps.org/abstract/PRB/v80/i12/e121406

[260] K. V. Emtsev, A. Bostwick, K. Horn, J. Jobst, G. L. Kellogg, L. Ley, J. L. McChesney, T. Ohta, S. A. Reshanov, J. Rohrl, E. Rotenberg, A. K. Schmid, D. Waldmann, H. B. Weber, and T. Seyller, "Towards wafer-size graphene layers by atmospheric pressure graphitization of silicon carbide," *Nature Materials*, vol. 8, no. 3, pp. 203–207, 2009. [Online]. Available: http://www.nature.com/nmat/journal/v8/n3/abs/nmat2382.html

[261] C. Virojanadara, M. Syvajarvi, R. Yakimova, L. I. Johansson, A. A. Zakharov, and T. Balasubramanian, "Homogeneous large-area graphene layer growth on

6H − SiC(0001),” *Physical Review B*, vol. 78, no. 24, p. 245403, 2008. [Online]. Available: http://link.aps.org/abstract/PRB/v78/e245403

[262] J. L. Tedesco, G. G. Jernigan, J. C. Culbertson, J. K. Hite, Y. Yang, K. M. Daniels, R. L. Myers-Ward, C. R. Eddy, J. A. Robinson, K. A. Trumbull, M. T. Wetherington, P. M. Campbell, and D. K. Gaskill, “Morphology characterization of argon-mediated epitaxial graphene on c-face SiC,” *Applied Physics Letters*, vol. 96, no. 22, p. 222103, 2010.

[263] L. Biedermann, M. Bolen, M. Capano, D. Zemlyanov, and R. Reifenberger, “Insights into few-layer epitaxial graphene growth on $4H - SiC(000\bar{1})$ substrates from stm studies,” *Physical Review B*, vol. 79, no. 12, 2009. [Online]. Available: http://link.aps.org/doi/10.1103/PhysRevB.79.125411

[264] Luxmi, N. Srivastava, G. He, R. M. Feenstra, and P. J. Fisher, “Comparison of graphene formation on c-face and si-face $SiC0001$ surfaces,” *Physical Review B*, vol. 82, no. 23, p. 235406, 2010. [Online]. Available: http://link.aps.org/doi/10.1103/PhysRevB.82.235406

[265] K. S. Novoselov, A. K. Geim, S. V. Morozov, D. Jiang, Y. Zhang, S. V. Dubonos, I. V. Grigorieva, and A. A. Firsov, “Electric field effect in atomically thin carbon films,” *Science*, vol. 306, no. 5696, pp. 666–669, 2004. [Online]. Available: http://www.sciencemag.org/cgi/content/abstract/306/5696/666

[266] S. Adam, E. H. Hwang, V. M. Galitski, and S. Das Sarma, “A self-consistent theory for graphene transport,” *Proceedings of the National Academy of Sciences*, vol. 104, no. 47, pp. 18 392–18 397, 2007. [Online]. Available: http://www.pnas.org/content/104/47/18392.abstract

[267] J.-H. Chen, C. Jang, S. Adam, M. S. Fuhrer, E. D. Williams, and M. Ishigami,

“Charged-impurity scattering in graphene,” *Nature Physics*, vol. 4, no. 5, pp. 377–381, 2008. [Online]. Available: http://dx.doi.org/10.1038/nphys935

[268] J. Martin, N. Akerman, G. Ulbricht, T. Lohmann, J. H. Smet, K. von Klitzing, and A. Yacoby, “Observation of electron-hole puddles in graphene using a scanning single-electron transistor,” *Nature Physics*, vol. 4, no. 2, pp. 144–148, 2008. [Online]. Available: http://dx.doi.org/10.1038/nphys781

[269] X. Wu, M. Sprinkle, X. Li, F. Ming, C. Berger, and W. A. de Heer, “Epitaxial-graphene/graphene-oxide junction: An essential step towards epitaxial graphene electronics,” *Physical Review Letters*, vol. 101, p. 026801, 2008. [Online]. Available: http://link.aps.org/doi/10.1103/PhysRevLett.101.026801

[270] D. R. Dreyer, S. Park, C. W. Bielawski, and R. S. Ruoff, “The chemistry of graphene oxide,” *Chemical Society Reviews*, vol. 39, pp. 228–240, 2010. [Online]. Available: http://dx.doi.org/10.1039/B917103G

[271] E. Bekyarova, M. E. Itkis, P. Ramesh, C. Berger, M. Sprinkle, W. A. de Heer, and R. C. Haddon, “Chemical modification of epitaxial graphene: Spontaneous grafting of aryl groups,” *Journal of the American Chemical Society*, vol. 131, no. 4, pp. 1336–1337, 2009. [Online]. Available: http://pubs.acs.org/doi/abs/10.1021/ja8057327

[272] M. Z. Hossain, M. A. Walsh, and M. C. Hersam, “Scanning tunneling microscopy, spectroscopy, and nanolithography of epitaxial graphene chemically modified with aryl moieties,” *Journal of the American Chemical Society*, vol. 132, no. 43, pp. 15 399–15 403, 2010. [Online]. Available: http://pubs.acs.org/doi/abs/10.1021/ja107085n

[273] S. Sarkar, E. Bekyarova, S. Niyogi, and R. C. Haddon, “Diels-alder chemistry of graphite and graphene: Graphene as diene and dienophile,” *Journal of the*

American Chemical Society, vol. 133, no. 10, pp. 3324–3327, 2011. [Online]. Available: http://pubs.acs.org/doi/abs/10.1021/ja200118b

[274] J. O. Sofo, A. S. Chaudhari, and G. D. Barber, "Graphane: A two-dimensional hydrocarbon," *Physical Review B*, vol. 75, p. 153401, 2007. [Online]. Available: http://link.aps.org/doi/10.1103/PhysRevB.75.153401

[275] D. C. Elias, R. R. Nair, T. M. G. Mohiuddin, S. V. Morozov, P. Blake, M. P. Halsall, A. C. Ferrari, D. W. Boukhvalov, M. I. Katsnelson, A. K. Geim, and K. S. Novoselov, "Control of graphene's properties by reversible hydrogenation: Evidence for graphane," *Science*, vol. 323, no. 5914, pp. 610–613, 2009. [Online]. Available: http://www.sciencemag.org/content/323/5914/610.abstract

[276] R. Balog, B. Jorgensen, L. Nilsson, M. Andersen, E. Rienks, M. Bianchi, M. Fanetti, E. Laegsgaard, A. Baraldi, S. Lizzit, Z. Sljivancanin, F. Besenbacher, B. Hammer, T. G. Pedersen, P. Hofmann, and L. Hornekaer, "Bandgap opening in graphene induced by patterned hydrogen adsorption," *Nature Materials*, vol. 9, no. 4, pp. 315–319, 2010. [Online]. Available: http://dx.doi.org/10.1038/nmat2710

[277] S.-H. Cheng, K. Zou, F. Okino, H. R. Gutierrez, A. Gupta, N. Shen, P. C. Eklund, J. O. Sofo, and J. Zhu, "Reversible fluorination of graphene: Evidence of a two-dimensional wide bandgap semiconductor," *Physical Review B*, vol. 81, p. 205435, 2010. [Online]. Available: http://link.aps.org/doi/10.1103/PhysRevB.81.205435

[278] M. Z. Hossain, J. E. Johns, K. H. Bevan, H. J. Karmel, Y. T. Liang, S. Yoshimoto, K. Mukai, T. Koitaya, J. Yoshinobu, M. Kawai, A. M. Lear, L. L. Kesmodel, S. L. Tait, and M. C. Hersam, "Chemically homogeneous and thermally reversible oxidation of epitaxial graphene,"

Nature Chemistry, vol. 4, no. 4, pp. 305–309, 2012. [Online]. Available: http://dx.doi.org/10.1038/nchem.1269

[279] S. Niyogi, E. Bekyarova, J. Hong, S. Khizroev, C. Berger, W. de Heer, and R. C. Haddon, "Covalent chemistry for graphene electronics," *The Journal of Physical Chemistry Letters*, vol. 2, no. 19, pp. 2487–2498, 2011. [Online]. Available: http://pubs.acs.org/doi/abs/10.1021/jz200426d

[280] K. Nakada, M. Fujita, G. Dresselhaus, and M. S. Dresselhaus, "Edge state in graphene ribbons: Nanometer size effect and edge shape dependence," *Physical Review B*, vol. 54, no. 24, pp. 17 954–17 961, 1996. [Online]. Available: http://link.aps.org/doi/10.1103/PhysRevB.54.17954

[281] M. Fujita, K. Wakabayashi, K. Nakada, and K. Kusakabe, "Peculiar localized state at zigzag graphite edge," *Journal of the Physical Society of Japan*, vol. 65, no. 7, pp. 1920–1923, 1996. [Online]. Available: http://jpsj.ipap.jp/link?JPSJ/65/1920/

[282] O. V. Yazyev, R. B. Capaz, and S. G. Louie, "Theory of magnetic edge states in chiral graphene nanoribbons," *Physical Review B*, vol. 84, no. 11, p. 115406, 2011. [Online]. Available: http://link.aps.org/doi/10.1103/PhysRevB.84.115406

[283] A. R. Akhmerov, J. H. Bardarson, A. Rycerz, and C. W. J. Beenakker, "Theory of the valley-valve effect in graphene nanoribbons," *Physical Review B*, vol. 77, no. 20, p. 205416, 2008. [Online]. Available: http://link.aps.org/doi/10.1103/PhysRevB.77.205416

[284] Y.-W. Son, M. L. Cohen, and S. G. Louie, "Energy gaps in graphene nanoribbons," *Physical Review Letters*, vol. 97, no. 21, p. 216803, 2006. [Online]. Available: http://link.aps.org/doi/10.1103/PhysRevLett.97.216803

[285] M. Y. Han, B. Özyilmaz, Y. Zhang, and P. Kim, "Energy band-gap engineering of graphene nanoribbons," *Physical Review Letters*, vol. 98, p. 206805, 2007. [Online]. Available: http://link.aps.org/doi/10.1103/PhysRevLett.98.206805

[286] M. Y. Han, J. C. Brant, and P. Kim, "Electron transport in disordered graphene nanoribbons," *Physical Review Letters*, vol. 104, p. 056801, 2010. [Online]. Available: http://link.aps.org/doi/10.1103/PhysRevLett.104.056801

[287] E. R. Mucciolo, A. H. Castro Neto, and C. H. Lewenkopf, "Conductance quantization and transport gaps in disordered graphene nanoribbons," *Physical Review B*, vol. 79, p. 075407, 2009. [Online]. Available: http://link.aps.org/doi/10.1103/PhysRevB.79.075407

[288] M. Evaldsson, I. V. Zozoulenko, H. Xu, and T. Heinzel, "Edge-disorder-induced anderson localization and conduction gap in graphene nanoribbons," *Physical Review B*, vol. 78, p. 161407, 2008. [Online]. Available: http://link.aps.org/doi/10.1103/PhysRevB.78.161407

[289] C. Stampfer, J. Güttinger, S. Hellmüller, F. Molitor, K. Ensslin, and T. Ihn, "Energy gaps in etched graphene nanoribbons," *Physical Review Letters*, vol. 102, p. 056403, 2009. [Online]. Available: http://link.aps.org/doi/10.1103/PhysRevLett.102.056403

[290] F. Sols, F. Guinea, and A. H. C. Neto, "Coulomb blockade in graphene nanoribbons," *Physical Review Letters*, vol. 99, p. 166803, 2007. [Online]. Available: http://link.aps.org/doi/10.1103/PhysRevLett.99.166803

[291] X. Li, X. Wang, L. Zhang, S. Lee, and H. Dai, "Chemically derived, ultrasmooth graphene nanoribbon semiconductors," *Science*, vol. 319, no. 5867, pp. 1229–1232, 2008. [Online]. Available: http://www.sciencemag.org/content/319/5867/1229.abstract

[292] X. Wang, Y. Ouyang, X. Li, H. Wang, J. Guo, and H. Dai, "Room-temperature all-semiconducting sub-10-nm graphene nanoribbon field-effect transistors," *Physical Review Letters*, vol. 100, p. 206803, 2008. [Online]. Available: http://link.aps.org/doi/10.1103/PhysRevLett.100.206803

[293] L. Jiao, L. Zhang, X. Wang, G. Diankov, and H. Dai, "Narrow graphene nanoribbons from carbon nanotubes," *Nature*, vol. 458, no. 7240, pp. 877–880, 2009. [Online]. Available: http://dx.doi.org/10.1038/nature07919

[294] L. Jiao, X. Wang, G. Diankov, H. Wang, and H. Dai, "Facile synthesis of high-quality graphene nanoribbons," *Nature Nanotechnology*, vol. 5, no. 5, pp. 321–325, 2010. [Online]. Available: http://dx.doi.org/10.1038/nnano.2010.54

[295] X. Wang, Y. Ouyang, L. Jiao, H. Wang, L. Xie, J. Wu, J. Guo, and H. Dai, "Graphene nanoribbons with smooth edges behave as quantum wires," *Nature Nanotechnology*, vol. 6, no. 9, pp. 563–567, 2011. [Online]. Available: http://dx.doi.org/10.1038/nnano.2011.138

[296] K. Wakabayashi, Y. Takane, and M. Sigrist, "Perfectly conducting channel and universality crossover in disordered graphene nanoribbons," *Physical Review Letters*, vol. 99, no. 3, p. 036601, 2007. [Online]. Available: http://link.aps.org/doi/10.1103/PhysRevLett.99.036601

[297] C. Tao, L. Jiao, O. V. Yazyev, Y.-C. Chen, J. Feng, X. Zhang, R. B. Capaz, J. M. Tour, A. Zettl, S. G. Louie, H. Dai, and M. F. Crommie, "Spatially resolving edge states of chiral graphene nanoribbons," *Nature Physics*, vol. 7, no. 8, pp. 616–620, 2011. [Online]. Available: http://www.nature.com/nphys/journal/v7/n8/full/nphys1991.html

[298] M. Syväjärvi, R. Yakimova, and E. Janzén, "Step-bunching in SiC epitaxy: anisotropy and influence of growth temperature," *Journal of*

Crystal Growth, vol. 236, no. 13, pp. 297–304, 2002. [Online]. Available: http://www.sciencedirect.com/science/article/pii/S0022024801023314

[299] H. Nakagawa, S. Tanaka, and I. Suemune, "Self-ordering of nanofacets on vicinal SiC surfaces," *Physical Review Letters*, vol. 91, p. 226107, 2003. [Online]. Available: http://link.aps.org/doi/10.1103/PhysRevLett.91.226107

[300] A. Nakajima, H. Yokoya, Y. Furukawa, and H. Yonezu, "Step control of vicinal 6H–SiC(0001) surface by h[sub 2] etching," *Journal of Applied Physics*, vol. 97, no. 10, p. 104919, 2005. [Online]. Available: http://link.aip.org/link/?JAP/97/104919/1

[301] J. Robinson, X. Weng, K. Trumbull, R. Cavalero, M. Wetherington, E. Frantz, M. LaBella, Z. Hughes, M. Fanton, and D. Snyder, "Nucleation of epitaxial graphene on SiC(0001)," *ACS Nano*, vol. 4, no. 1, pp. 153–158, 2010, pMID: 20000439. [Online]. Available: http://pubs.acs.org/doi/abs/10.1021/nn901248j

[302] W. Norimatsu and M. Kusunoki, "Formation process of graphene on SiC(0001)," *Physica E: Low-dimensional Systems and Nanostructures*, vol. 42, no. 4, pp. 691–694, 2010. [Online]. Available: http://www.sciencedirect.com/science/article/pii/S1386947709006432

[303] S. Nie, C. Lee, R. Feenstra, Y. Ke, R. Devaty, W. Choyke, C. Inoki, T. Kuan, and G. Gu, "Step formation on hydrogen-etched 6H-SiC{0001} surfaces," *Surface Science*, vol. 602, no. 17, pp. 2936–2942, 2008. [Online]. Available: http://www.sciencedirect.com/science/article/pii/S0039602808005049

[304] S. Tanaka, K. Morita, and H. Hibino, "Anisotropic layer-by-layer growth of graphene on vicinal SiC(0001) surfaces," *Physical Review B*, vol. 81, p. 041406, 2010. [Online]. Available: http://link.aps.org/doi/10.1103/PhysRevB.81.041406

[305] J. Baringhaus, C. Tegenkamp, F. Edler, M. Ruan, E. Conrad, C. Berger, and W. A. de Heer, "Exceptional ballistic transport in epitaxial graphene nanoribbons," *arXiv:1301.5354*, 2013. [Online]. Available: http://arxiv.org/abs/1301.5354

[306] Y.-J. Yu, Y. Zhao, S. Ryu, L. E. Brus, K. S. Kim, and P. Kim, "Tuning the graphene work function by electric field effect," *Nano Letters*, vol. 9, no. 10, pp. 3430–3434, 2009, pMID: 19719145. [Online]. Available: http://pubs.acs.org/doi/abs/10.1021/nl901572a

[307] Collaboration: Authors and Editors of the LB Volumes III/17A-22A-41A1b, "Silicon carbide (SiC), work function," in *Group IV Elements, IV-IV and III-V Compounds. Part b - Electronic, Transport, Optical and Other Properties*, O. Madelung, U. Rössler, and M. Schulz, Eds. Berlin/Heidelberg: Springer, Inc., 2013, vol. B, pp. 1–2. [Online]. Available: http://www.springermaterials.com/index/chapterdoi/10.1007/10832182_607

[308] F. Ming and A. Zangwill, "Model for the epitaxial growth of graphene on $6\mathrm{H}-\mathrm{SiC}(0001)$," *Physical Review B*, vol. 84, p. 115459, 2011. [Online]. Available: http://link.aps.org/doi/10.1103/PhysRevB.84.115459

[309] P. N. First, W. A. de Heer, T. Seyller, C. Berger, J. A. Stroscio, and J.-S. Moon, "Epitaxial graphenes on silicon carbide," *MRS Bulletin*, vol. 35, pp. 296–305, 2010.

[310] G. F. Sun, J. F. Jia, Q. K. Xue, and L. Li, "Atomic-scale imaging and manipulation of ridges on epitaxial graphene on 6H-SiC(0001)," *Nanotechnology*, vol. 20, no. 35, p. 355701, 2009. [Online]. Available: http://stacks.iop.org/0957-4484/20/i=35/a=355701

[311] J. Hicks, A. Tejeda, A. Taleb-Ibrahimi, M. S. Nevius, F. Wang, K. Shepperd,

J. Palmer, F. Bertran, P. Le Fvre, J. Kunc, W. A. de Heer, C. Berger, and E. H. Conrad, "A wide-bandgap metal-semiconductor-metal nanostructure made entirely from graphene," *Nature Physics*, vol. 9, no. 1, pp. 49–54, 2013. [Online]. Available: http://www.nature.com/nphys/journal/v9/n1/full/nphys2487.html#/supplementary-information

[312] F. Guinea, M. I. Katsnelson, and A. K. Geim, "Energy gaps and a zero-field quantum hall effect in graphene by strain engineering," *Nature Physics*, vol. 6, no. 1, pp. 30–33, 2010. [Online]. Available: http://dx.doi.org/10.1038/nphys1420

[313] N. Levy, S. A. Burke, K. L. Meaker, M. Panlasigui, A. Zettl, F. Guinea, A. H. C. Neto, and M. F. Crommie, "Strain-induced PseudoMagnetic fields greater than 300 tesla in graphene nanobubbles," *Science*, vol. 329, no. 5991, pp. 544 –547, 2010. [Online]. Available: http://www.sciencemag.org/content/329/5991/544.abstract

[314] N.-C. Yeh, M.-L. Teague, S. Yeom, B. Standley, R.-P. Wu, D. Boyd, and M. Bockrath, "Strain-induced pseudo-magnetic fields and charging effects on cvd-grown graphene," *Surface Science*, vol. 605, no. 17–18, pp. 1649–1656, 2011. [Online]. Available: http://www.sciencedirect.com/science/article/pii/S0039602811002275

[315] H. Yan, Y. Sun, L. He, J.-C. Nie, and M. H. W. Chan, "Observation of landau-level-like quantization at 77 k along a strained-induced graphene ridge," *Physical Review B*, vol. 85, p. 035422, 2012. [Online]. Available: http://link.aps.org/doi/10.1103/PhysRevB.85.035422

[316] K. V. Emtsev, F. Speck, T. Seyller, L. Ley, and J. D. Riley, "Interaction, growth, and ordering of epitaxial graphene on sic0001 surfaces: A comparative

photoelectron spectroscopy study," *Physical Review B*, vol. 77, p. 155303, 2008. [Online]. Available: http://link.aps.org/doi/10.1103/PhysRevB.77.155303

[317] A. Y. Ogbazghi, "Conductance through nanometer-scale metal-to-graphite contacts," Dissertation, Georgia Institute of Technology, 2005.

[318] N. P. Guisinger, G. M. Rutter, J. N. Crain, P. N. First, and J. A. Stroscio, "Exposure of epitaxial graphene on SiC(0001) to atomic hydrogen," *Nano Letters*, vol. 9, no. 4, pp. 1462–1466, 2009. [Online]. Available: http://pubs.acs.org/doi/abs/10.1021/nl803331q

VITA

David Britt Torrance was born in Atlanta, GA on December 26, 1984 to parents Ralph and Deborah Torrance. He spent the majority of his adolescence in Jacksonville, FL. He graduated from the University of Central Florida with a Bachelor of Science in Physics in 2007. Directly following graduation he entered the PhD program in the School of Physics at the Georgia Institute of Technology. He still does not know what he wants to be when he grows up, and probably never will.